Far Field and Near Field Terahertz Spectroscopy on Parabolic Quantum Wells

Dissertation an der Fakultät für Physik
der Ludwig–Maximilians–Universität München
vorgelegt von Guillermo Acuña aus Buenos Aires,
Argentinien

München, im Februar 2010

Betreuer: Prof. Dr. Roland Kersting
Zweitgutachter: Prof. Dr. Achim Hartschuh
Mündliche Prüfung am 03.05.2010

Content

List of Publications during this Dissertation

i. F. Buersgens, G. Acuna, C. H. Lang, S. Manus and R. Kersting, "Shear force control for a terahertz near filed microscope",
Rev. Sci. Instr. **78**, 113701 (2007).

ii. F. Buersgens, G. Acuna and R. Kersting, "Millimeter wave probing of the acoustic phase for concealed object detection",
Opt. Express **15**, 8838 (2007).

iii. F. Buersgens, G. Acuna and R. Kersting, "Acoustic phase imaging with terahertz radiation",
Opt. Express **15**, 4427 (2007).

iv. F. Buersgens, G. Acuna and R. Kersting, "Terahertz imaging of concealed objects by acoustic phase detection",
Terahertz Mil. Sec. Appl. IV, **6949**, 94905 (2008).

v. R. Kersting, F. Buersgens and G. Acuna, "Mapping the acoustic phase with terahertz and millimeter wave techniques",
TM-Technisches Messen **75**, 51 (2008).

vi. G. Acuna, F. Buersgens, C. H. Lang and R. Kersting, "Impact of High-Field Charge Transport on Terahertz Emission From Semiconductor Devices",
IEEE J. Sel. Top. Quant. Electr. **14**, 1 (2008).

vii. R. Kersting, F. Buersgens, G. Acuna and G. C. Cho, "Terahertz Near-Field Microscopy",
Advances in Solid State Physics, Bd. 47.
Springer Berlin / Heidelberg (2008).

viii. G. Acuna, F. Buersgens, C. H. Lang, M. Handloser, A. Guggenmos and R. Kersting, "Interdigitated terahertz emitters",
Electr. Lett. **44**, 3 (2008).

ix. G. Acuna, S. Heucke, F. Kuchler, H-T. Chen, A. Taylor and R. Kersting, "Surface plasmons in terahertz metamaterials",
Opt. Express **16**, 18745 (2008).

x. S. Funk, G. Acuna, M. Handloser and R. Kersting, ”Probing the momentum relaxation time of charge carriers in ultrathin layers with terahertz radiation”,
Opt. Express **17**, 17450 (2009).

Previous Publications

i. A. Medus, G. Acuña and C. Dorso, ”Detection of community structures in networks via global optimization”,
Physica A **358**, 593 (2005).

ii. G. Acuña and J. Miraglia, ”Time-dependent induced potentials in convoy electron emission”,
Surface Science **600**, 4961 (2006).

Contributions to Conferences

i. G. Acuna, and R. Kersting, ”Interdigitated terahertz emitters”, International Conference on Infrared and Millimeter Waves 2007, Cardiff, Wales.

ii. F. Buersgens, G. Acuna, and R. Kersting, ”Concealed object detection by far infrared sensing of the acoustic phase”, International Conference on Infrared and Millimeter Waves 2007, Cardiff, Wales.

iii. G. Acuna, F. Buersgens, C.H. Lang, and R. Kersting, ”Terahertz Emission from Charge Transport in Inhomogeneous Fields”, CLEO QELS 2008, San José, California, USA.

iv. G. Acuna, F. Kuchler, R. Kersting, H-T Chen, A. Taylor, and A Gossard, ”Time-resolved Terahertz Microscopy of Nanostructures”, CLEO QELS 2008, San José, California, USA.

v. F. Buersgens, G. Acuna, and R. Kersting, ”Terahertz imaging of concealed objects by acoustic phase detection”, SPIE Defense & Security Symposium 2008, Orlando, Florida, USA.

vi. G. Acuna, S.F. Heucke, M. Handloser, and R. Kersting, ”Terahertz near-field microscopy with extreme subwavelength resolution”, II International Symposium ”Topical Problems of Biophotonics” 2009, Samara, Russia.

Kurzfassung

Die Dynamik und das Streuverhalten von Elektronen in zweidimensionalen Elektronengasen (2DEG) hat wissenschaftlich und technologisch große Bedeutung. Einerseits bestimmt die Dynamik grundlegende Phänomene wie den Quanten-Hall-Effekt und anderseits ist sie maßgeblich für das Verhalten von Halbleiterbauelementen und deren langfristig erreichbare Schaltgeschwindigkeit. Hierbei ist vor allem die Frage nach den Ursachen und Beiträgen der verschiedenen Streuprozesse bislang nicht eindeutig geklärt.

Im Mittelpunkt der vorliegenden Arbeit steht die Untersuchung und Quantifizierung der Streuung in 2DEGs in AlGaAs-GaAs-Halbleiter-Heterostrukturen mit Hilfe von Terahertz (THz) Fern- und Nahfeldspektroskopie. Im gewählten Modellsystem werden die unterschiedlichen Bandlücken beider Materialien so eingesetzt, dass der resultierende parabolische Potentialverlauf im Leitungsband einen Quantentopf bildet, in dem die elektronischen Zustände entlang der Wachstumsrichtung quantisiert sind. Der parabolische Quantentopf ist hierbei so bemessen, dass die äquidistanten Subbänder Übergangsfrequenzen im Terahertz-Bereich haben. Hingegen können sich die Elektronen in der Ebene senkrecht zur Wachstumsrichtung des Quantentopfs frei bewegen und daher mit Hilfe des Drude-Modells beschrieben werden.

In dieser Arbeit wird erstmals die Streu- bzw. Dephasierungszeit der Elektronen in ihrer freien und quantisierten Bewegung mit extremer Subwellenlängen-Auflösung mittels apperturlose THz-Nahfeldmikroskopie bestimmt. Der Vergleich der Ergebnisse der kontaktlosen Messungen im Nah- und Fernfeld zeigt zudem, dass vor allem inhomogene Linienverbreiterung die Kohärenz der Intersubbandübergänge im parabolischen Quantentopf begrenzt. Diese inhomogene Verbreiterung wird vor allem durch die lokal variierende Größe des Quantentopfs hervorgerufen. So ergeben Messungen bei kryogenischen Temperaturen auf einer Fläche von etwa 1 mm^2 (d.h im Fernfeld) eine Dephasierungszeit von τ_d^{ff} =0.49±0.08 ps, während Nahfeldmessungen, die über eine Fläche des Quantentopfs von nur etwa 1 μm^2 mitteln, eine Dephasierungszeit von τ_d^{nf} =2.3 ± 0.3 ps zeigen. Davon abweichend ergeben die Drude-Streuzeiten im Nah- und Fernfeld einen nahezu übereinstimmenden Wert (τ_m^{nf} =500±200 fs bzw. τ_m^{ff} =350±150 fs). Für diese Messungen wird eine Elektromodulationstechnik angewendet, die es erlaubt, den THz-Signalbeitrag der Ladungsträger zu isolieren, indem die Ladungsträger periodisch durch ein elektrostatisches Potential aus dem Detektionsvolumen verdrängt werden. In Fernfeldmessungen wird hierzu eine Modulationsspannung zwischen dem 2DEG und dem mikrostrukturierten metallischen Gitter auf der Oberfläche der Heterostruktur angelegt, das zur Kopplung des THz-Feldes in den Quantentopf benötigt wird. In Nahfeldmessungen hingegen werden das 2DEG und die Nahfeldsonde auf unterschiedliche Potentiale gelegt, so dass sich lediglich eine lokale Modulation der Ladungsträgerdichte unterhalb der Nahfeldsonde ergibt.

Diese Ergebnisse werden durch substantielle Verbesserungen der experimentellen Methodik während dieser Arbeit ermöglicht. Unter anderem ist das weltweit erste kryogenische THz-Nahfeldmikroskop entwickelt worden, das die Antenneneigenschaften der Nahfeldsonde nutzt, um extreme Subwellenlängen-Auflösungen zu erzielen. Durch die Implementierung einer Scherkraft-Abstandsregelung werden zudem topografische Artefakte im Bildkontrast vermieden. Mit den eigens entwickelten THz-Emittern werden darüber hinaus ausreichend hohe Singal-Rauschabstände zur Detektion des Signalbeitrags der Ladungsträger realisiert.

1 Introduction

Over the last decades, the trend in semiconductor technology has consisted of a steady reduction of structure size together with an increase of the number of transistors per unit area, in a manner approximately following Moore's law [1]. Recently electronic circuits have approached dimensions smaller than 100 nm, where quantum effects start playing a significant role [2]. In order to obtain a quantitative understanding of the electronic excitations in such structures, it is necessary to develop new spectroscopic approaches that do not perturb the quantum properties of the devices being tested and on the same footing yield a resolution on the nanometer regime.

Since scattering rates as well as plasma frequencies in current semiconductor devices lie in the terahertz (THz) range of the optical spectrum, its use for mapping charge carriers is becoming increasingly popular. The so called THz band (from about 0.1 to 10 THz) was considered to be a gap until the late 1980's when different THz emission and detection schemes were developed. Terahertz spectroscopy for semiconductors was first introduced in the 1990's for macroscopic Si samples [3, 4]. However, the use in industry for characterizing heterostructures is still not common since all these measurements were diffraction limited and only macroscopic structures were addressed. In the present work, a cryogenic microscope for THz near field spectroscopy with subwavelength spatial resolution is developed. Using this microscope, the response of electrons in a parabolic quantum well with intersubband transitions in the THz range are investigated.

Two main parameters can be used to characterize the electron response in quantized structures: The momentum relaxation time τ_m and the dephasing time τ_d. The first parameter, defines charge transport in solids for a Drude electron gas and is also crucial for the optimization of the switching speed in electronic devices. The second one describes the coherence of electrons performing intersubband transitions and has also been previously studied using far field techniques [5–7]. Understanding the mechanisms that affect this coherence is vital for the development and optimization of devices such as quantum cascade lasers [8, 9] operating at THz frequencies.

In the following, the forthcoming chapters are going to be briefly introduced.

The chapter, "Background", is devoted to the fundamentals of semiconductor structures. Basic properties of doped semiconductors are reviewed. The carrier drift and the momentum relaxation time within the Drude model are addressed. Later, the fabrication of quantum well structures is discussed together with an analysis of the intersubband transitions in quantum wells. This chapter ends with a review of the different ways of contacting electron gases in semiconductors, employed in this work

In the third chapter "Terahertz Spectroscopy and Microscopy", the basics of terahertz radiation and terahertz techniques are included. The main approaches for the generation and detection of THz pulsed radiation are discussed. Finally the main limitations of conventional far field spectroscopy are addressed and a method to overcome this shortcomings, aperture-less near field microscopy, is included. It is important to understand the imaging mechanism of this technique. For this purpose, two models are presented: The dipole model and the antenna model.

The fourth chapter "Development of a Terahertz Near Field Microscope" deals with the design and implementation of a setup for the measurements performed in this work. In particular the fabrication of a novel THz emitter and its impact on the signal to noise ratio is studied. In addition, a method for reducing artifacts arising from the sample's topography is included. This technique is based on shear force control and enables THz near field microscopy with extreme subwavelength resolution.

In the fifth chapter "Preparation and Characterization of the Parabolic Quantum Well Structure" the quantum well structure to be studied is presented. The layer sequence that forms the sample is discussed in detail. The different connections to the quantum well are included. Techniques to efficiently excite intersubband transitions with THz radiation in the far field and in the near field are addressed. An electronic characterization of the structure is performed and the electron density in the well is deduced. A complementary method for studying the quantum well based on numerical simulation ends this chapter. With this technique a relevant parameter is estimated, the intersubband transition frequency.

In the sixth chapter "Far Field and Near Field Terahertz Spectroscopy Measurements" the main results of this dissertation are presented. By a novel technique, based on electro-modulation, the contribution to the overall signal of the electrons in the quantum well can be isolated. Terahertz interaction with a Drude electron gas as well as with the excitation of intersubband transition was observed and temporally and spectrally resolved. These measurements were carried out in the far field and in the near field. A theoretical model, based on the thin film equations, was developed for the interpretation of the results obtained. The momentum relaxation time τ_m and the dephasing time τ_d are deduced for the far field and near field experiments. This allows for the determination of the dephasing mechanisms that affect the coherence of the intersubband transitions.

2 Background

In the first section of this chapter, the basic concepts of semiconductors, which includes definition, dispersion relation, differences between direct and indirect semiconductors and doping are revisited. In addition, the carriers' velocity in the drift regime and the Drude model are addressed. Most of the following discussion is based on standard solid state and semiconductor books like [10] and [11].
In the following section interfaces between semiconductors are studied with an emphasis on $Al_xGa_{1-x}As$*-GaAs heterointerfaces, which will be employed throughout this work. Moreover, the origin of a quantum well and a two dimensional electron gas is discussed together with techniques for introducing high mobility carriers in the wells. This section ends with a discussion of the techniques, which are applied to shape the quantum wells.*
A further section is devoted to the physics of intersubband transitions. Most of the concepts in that section are adapted from [12, 13]. Following an introduction, interaction with light is discussed together with fundamental properties of parabolic quantum wells ending with an overview of the mechanisms that lead to dephasing of a macroscopic intersubband polarization.
Depending on the desired application, like for example feeding an electrical current or controlling the carrier density, semiconductors need to be contacted with metals. Therefore in the last section of this chapter, the main two ways of doing so, the so called Schottky contact and the Ohmic contact are introduced.

2.1 Semiconductors

Electrons of single and isolated atoms occupy discrete energy levels known as atomic orbitals. If a large number of atoms (for example more than 10^{15}) are brought together to form a solid, the energy levels can be more properly described in terms of nearly continuous energy bands. These energy bands determine the relationship between the electron's energy and momentum. In terms of the band structure, solids can be classified into metals, insulators and semiconductors (Fig. 2.1). In metals there is at least one band which is partially filled at a temperature of 0 K and therefore, by applying an external electric field, electrons can be directly excited into higher energy states and a current can be detected. In an insulator, however, the uppermost populated band is full at 0 K. There is a large bandgap E_g, between this band (valence band) and the next empty band (conduction band). As a result, when an external electric field is applied, these materials conduct almost no current. If the temperature is raised, there is a probability that some electrons will be excited across the gap into the conduction band leaving holes in the valence

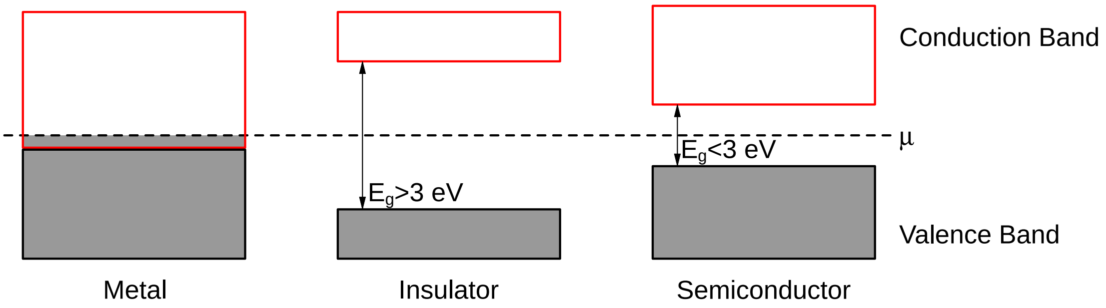

Figure 2.1: Conduction and valence band for metals, insulators and semiconductors. Bands are filled with electrons up to the chemical potential μ

band. Both electrons and holes, are capable of conducting. The probability of finding electrons (or holes) in a determined band with a certain energy E is given by the Fermi-Dirac distribution:

$$F(E) = \frac{1}{1 + e^{(E-E_F)/k_B T}} \approx e^{-\frac{E-E_F}{k_B T}}, \tag{2.1.1}$$

where E_F is the fermi energy which in this context should be regarded as the chemical potential μ [10]. The Fermi energy lies within the bang gap so, whether a thermal excitation leads to noticeable conductivity strongly depends on the band gap. Although it is not a sharp distinction, solids with a band gap smaller than 3 eV are historically denominated semiconductors.

2.1.1 Dispersion Relation

Free electrons show a dispersion relationship given by:

$$E = \frac{\mathbf{p}^2}{2m_o} = \frac{\hbar^2 \mathbf{k}^2}{2m_o}, \tag{2.1.2}$$

with $\mathbf{p}$ the momentum, m_o the free electron mass and $\mathbf{k}$ the wave vector. In a semiconductor with a periodic crystal structure electrons have a dispersion relation given by Bloch's theorem [14]. However close to the band edge, at the bottom of the conduction band, the dispersion relationship can be approximated by a quadratic expression

$$E = \frac{\hbar^2 \mathbf{k}^2}{2m_{eff}}, \tag{2.1.3}$$

where m_{eff} is the associated effective mass. Therefore electrons in the conduction band close to the band edge will behave as nearly free electrons with an effective mass determined by:

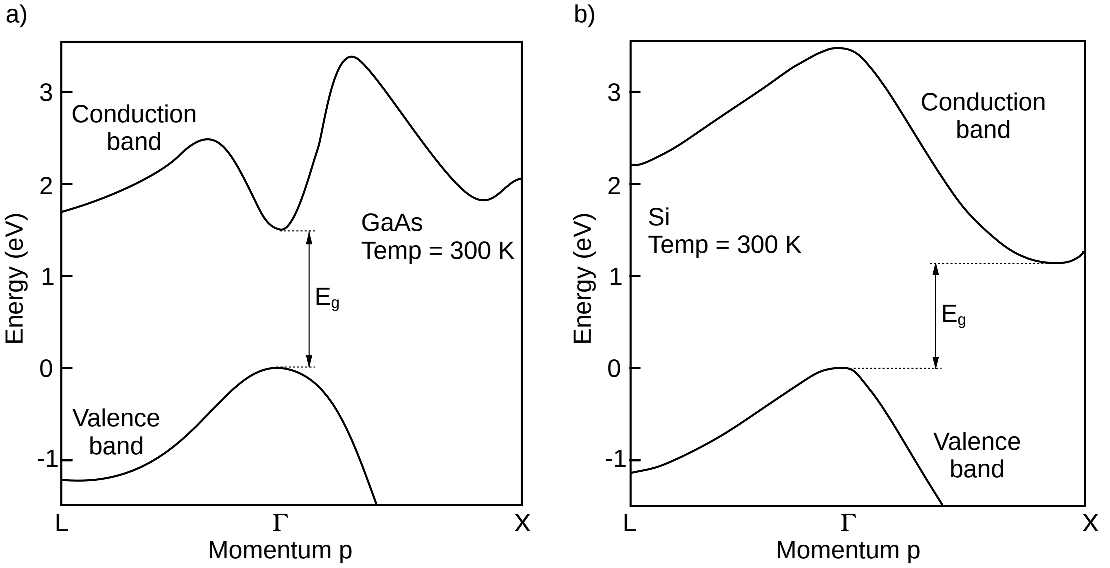

Figure 2.2: a) Example of a direct semiconductor, GaAs and b) of an indirect semiconductor, Si.

$$m_{eff} = \frac{\hbar}{\frac{\partial^2 E}{\partial \mathbf{k}^2}}. \tag{2.1.4}$$

For the last equation it has been assumed that the energy only depends on the modulus of the wave vector **k**. If this is not the case, the effective mass is not a scalar but rather a tensor [15].

2.1.2 Direct and Indirect Semiconductors

Depending on the relative position of the edges of the conduction and valence bands in k-space, semiconductors can be classified into direct and indirect. In the first case, the maximum of the valence band and the minimum of the conduction band occur at the same momentum, an example of a direct semiconductor is GaAs ($k = 0$), (Fig. 2.2 a)). Thus, for an electron to make a transition from the valence band to the conduction band just a change of energy and not of momentum is needed. In indirect semiconductors, the band edges occur at different momenta values, like for instance in Si, (Fig. 2.2 b)). Therefore, electrons that make a transition from the valence band to the conduction band, need not only a change of energy but also of momentum (or much more energy than the one given by the bang gap, E_g).

2.1.3 Doping of Semiconductors

As discussed before, homogeneous (intrinsic) semiconductors will have a number of electrons (and holes) in the conduction (valence) band which strongly depends on the temperature. In

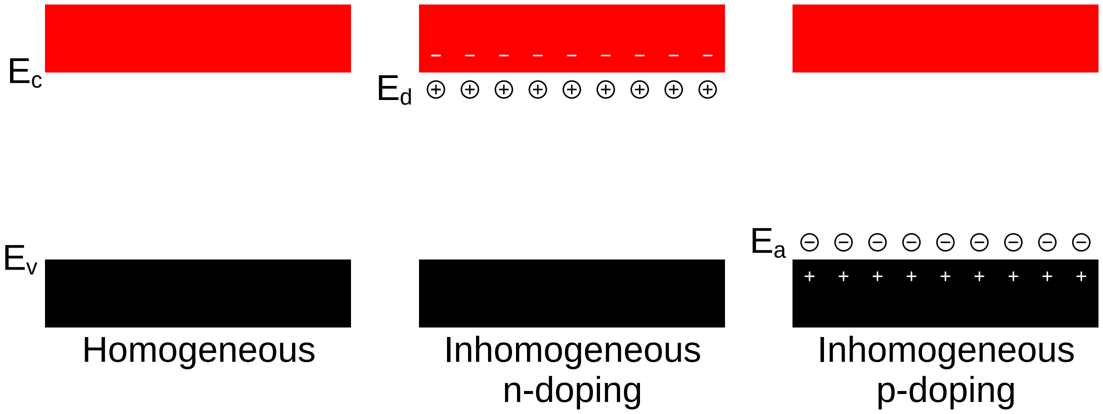

Figure 2.3: Homogeneous and inhomogeneous semiconductors with n-doping and p-doping.

many cases it is desirable to have a larger amount of carriers at a given temperature and also a carrier density which is independent of the temperature at least within a certain range. One way of achieving this in inhomogeneous semiconductors consists in adding suitable impurities to the crystal. This method is called doping. There are two types of dopants: Donors, which donate an electron to the conduction band (n-doping) and acceptors which accept an electron from the valence band (p-doping) and thus create a hole in the valence band, Fig. 2.3. The donors are chosen in a way that they have one (or more) extra electron in their outer shell compared to the host atom they replace. The extra electron now sees a positively charged extra ion to which it is attracted. This model resembles a Coulomb potential suppressed by the dielectric constant of the semiconductor host material. The calculations for the lowest energy level of these extra electrons, the donor energy level E_d, will follow that of hydrogen-like energy levels but affected by the dielectric function of the host semiconductor and the effective mass of the electron. For most semiconductors the donor energy level will lie just a few meV under the conduction band. Therefore it can be easily thermally excited. In an analogous way acceptors are selected so that the acceptor energy level, E_a, is also just a few meV above the valence band and can be easily thermally excited.

2.1.4 Carrier Drift

Upon applying an electric field $\mathcal{E}$, carriers in a semiconductor will initially accelerate increasing their velocity with a rate proportional to $\mathcal{E}$. This is the so called ballistic regime. After a characteristic time called mean free time τ_m (also known as momentum relaxation time), carriers will enter the drift regime. In this regime they undergo scattering events caused for instance by other carriers, the lattice or impurities. This will decrease the velocity of a single carrier leading to an average velocity named drift velocity v_d that is proportional to the applied electric field,

$$|v_d| = \mathcal{E}\mu_{e,h}, \tag{2.1.5}$$

where $\mu_{e,h}$ is the factor of proportionality called mobility which depends on the type of carrier, (e:electrons and h:holes). The mobility is related to the mean free time through

$$\mu_{e,h} = \frac{|q|\,\tau_m}{m_{eff}}, \tag{2.1.6}$$

with q being the carrier's charge.

2.1.5 Optical Properties of Doped Semiconductors: The Drude Model

Electrons in the conduction band of a doped semiconductor can be described using the Drude model. The central assumption of this model is that after the mean free time τ_m introduced in the previous section, electrons will experience on average a collision. An electron with a certain momentum $p(t)$ at time t will have a collision within $t + dt$ with a probability dt/τ_m, and therefore it will survive a time $t + dt$ without suffering a collision with probability $1 - dt/\tau_m$. When there are no collisions involved the change in momentum will be given by the electric field, $\mathcal{E}(t)$, and thus the electron acquires an additional momentum given by $q\,\mathcal{E}(t)dt$. Neglecting second order contributions, the following expression for the momentum can then be derived [10]

$$p(t + dt) = \left(1 - \frac{dt}{\tau_m}\right)(p(t) + q\,\mathcal{E}(t)dt), \tag{2.1.7}$$

which leads to a differential equation of the form

$$\frac{dp(t)}{dt} = -\frac{p(t)}{\tau_m} - q\,\mathcal{E}(t). \tag{2.1.8}$$

For an electron driven by an electric field given by $\mathcal{E}(t) = \Re\mathrm{e}(\mathcal{E}(\omega)e^{i\omega t})$, equation 2.1.8 has the following solution

$$p(t) = \Re\mathrm{e}(p(\omega)e^{i\omega t}), \tag{2.1.9}$$

with $p(\omega)$ given by the complex expression

$$p(\omega) = -\frac{q\mathcal{E}(\omega)}{(1/\tau_m + i\omega)}. \tag{2.1.10}$$

The current density j relates to p through

$$j(\omega) = \frac{qn_e p(\omega)}{m_{eff}}, \tag{2.1.11}$$

with n_e being the electron density. Following Ohm's law, the conductivity of the electrons in the conduction band $\sigma(\omega)$ is

$$\sigma(\omega) = \frac{j(\omega)}{\mathcal{E}(\omega)} = \frac{\sigma_o}{1 + i\omega\tau_m}, \quad \text{with} \quad \sigma_o = \frac{n_e q^2 \tau_m}{m_{eff}}. \tag{2.1.12}$$

2.2 Al$_x$Ga$_{1-x}$As-GaAs Semiconductor Heterointerfaces

2.2.1 Background

Semiconductor heterointerfaces are interfaces between two different types of semiconductors. Depending on the band alignment of the semiconductor the interfaces are classified in different types [14]. Type I comprises interfaces in which the smaller band gap lies completely inside the larger band gap, whereas type II includes all other possible combinations in which both bands of the first semiconductor lie above the corresponding bands of the second semiconductor [14]. An example of a type I heterointerface is Al$_x$Ga$_{1-x}$As-GaAs, in which the bandgap of GaAs lies inside the band gap of Al$_x$Ga$_{1-x}$As, like in Fig. 2.4a). In the following we will focus only on this type of structures since they are relevant for the present work. Al$_x$Ga$_{1-x}$As-GaAs structures have the advantage that both semiconductors have the same crystal structure and very small lattice mismatch (0.4 % for $x = 0.3$) which leads to a reduced strain in the heterojunction. Up to a maximum content of $x \approx 0.45$, Al$_x$Ga$_{1-x}$As behaves like a direct semiconductor [16]. The bands' mismatches, ΔE_c and ΔE_v depend linearly (up to $x \approx 0.45$) on the Al content, Fig. 2.4b).
High quality Al$_x$Ga$_{1-x}$As-GaAs structures are grown in ultra high vacuum ($< 5 \cdot 10^{-11}$ bar) using molecular-beam epitaxy (MBE). Typically the Al content is set to $x = 0.3$ and therefore $\Delta E_c \approx 300$ meV. By stacking several Al$_x$Ga$_{1-x}$As-GaAs interfaces different quantum wells can be realized, like for example triangular, square or parabolic ones.

2.2.2 Modulation Doping

The most direct way of introducing carriers is to dope the region in which electrons or holes are desired. One could think for instance of doping directly on the well, on the GaAs side, at a lower

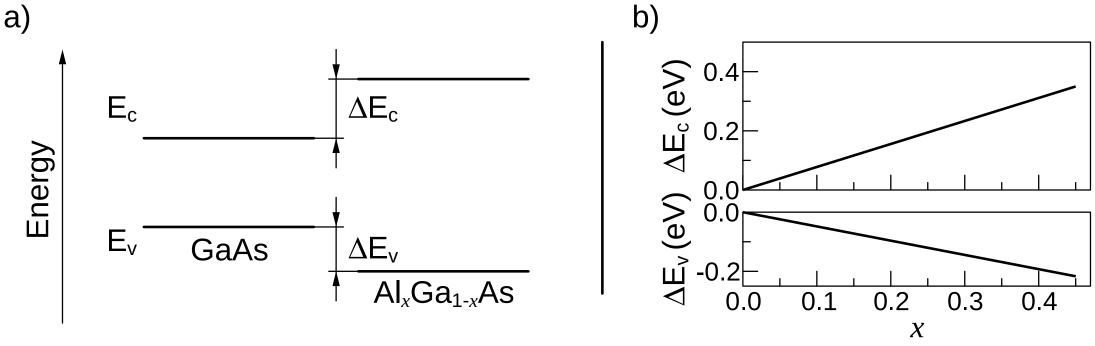

Figure 2.4: a) Energy band diagram of a Al_xGa_{1-x}As-GaAs semiconductor heterointerface. b) Dependence of the bands mismatch, $\varDelta E_c$ and $\varDelta E_v$ between GaAs and AlGaAs on the Al content x.

potential than the $Al_xGa_{1-x}As$ (Fig. 2.4a)). One major disadvantage of this technique is that charged donors and acceptors are left behind when electrons and holes are thermally excited and may scatter with the carriers through Coulomb interaction (ionized-impurity scattering). This leads to a reduced carrier mobility [1]. One technique for tackling this problem is the so called modulation doping, in which doping is performed in a certain region adjacent to where charges are desired. Carriers diffuse from this initial region into the desired one, so that carriers and ionized donors and acceptors are separated [17].

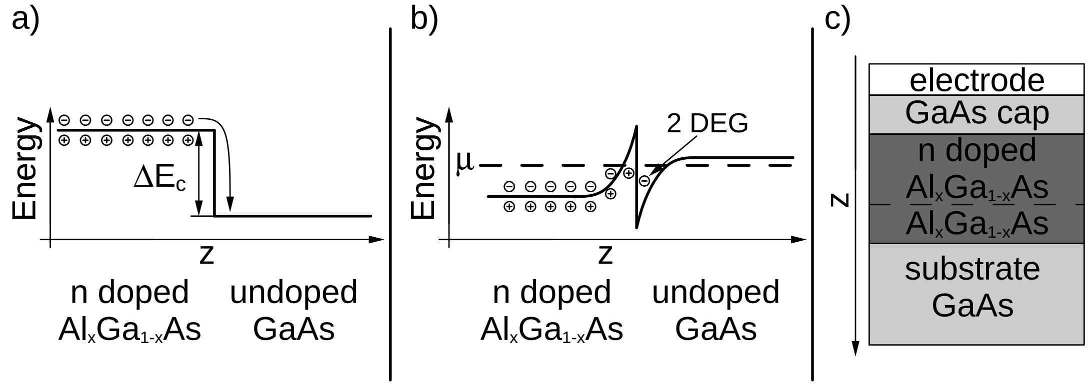

Figure 2.5: a) Conduction band diagram of a n-doped Al_xGa_{1-x}As-GaAs semiconductor heterointerface. Some of the electrons can cross into the GaAs until thermal equilibrium is reached and a two dimensional electron gas (2 DEG) is formed, b). Different layers of a Al_xGa_{1-x}As-GaAs heterostructure, c).

Figure 2.5a) illustrates an example of an heterointerface between n-doped $Al_xGa_{1-x}As$ and undoped GaAs. Some of the excited electrons in the $Al_xGa_{1-x}As$ conduction band will lower their

---

[1] This is particularly relevant at low temperatures, since the mobility from ionized impurities has a dependence with temperature given by $\propto T^{3/2}$ [15].

energy by crossing into the GaAs until thermal equilibrium is reached. In consequence, the chemical potential μ will be aligned. This will result in the band bending sketched in Fig. 2.5b). Electrons in the GaAs are confined in a quasi-triangular well since they can not go back through the ΔE_c barrier. Furthermore an electrostatic potential builds up between the ionized donors and the electrons on the GaAs that keeps the electrons close to the interface. This well is typically 10 nm wide at the energy of the electrons, with quantized energy levels in the heterostructure growth direction (z) but no confinement in the perpendicular direction, ($x - y$). This is the so called two dimensional electron gas (2 DEG).

Finally with the modulation doping technique electrons in the 2 DEG are separated from donors which drastically reduces the ionized-impurity scattering. A further improvement of the electrons mobility can be performed by introducing an undoped $Al_xGa_{1-x}As$ thin layer 2.5c). This increases the separation between electrons and donors enhancing the electrons mobility at the expense of having less electrons in the well. For experiments in which ultra high mobilities are required, this technique is applied [18, 19]. Devices are generally completed with a GaAs cap layer that prevents oxidation of the $Al_xGa_{1-x}As$.

2.2.3 Digital Alloy Technique

As mentioned before, the mismatch in the conduction band energy in $Al_xGa_{1-x}As$-GaAs heterointerfaces is a function of the Al content x. Therefore in principle, any desired well can be built by changing the Al content in the growth direction. However, in reality, this scheme is not followed since it involves a very precise control of the temperature of the Al furnace in the MBE. Instead another approach, called digital alloy technique is taken. First the MBE is calibrated to a certain Al content, generally x=0.3. Then the wide well is divided into very thin layers of around 2 nm, so that the Al content in each layer is either x=0 or x=0.3. In this way the average content of Al can be adjusted and several wells can be built [20–24]. In Fig 2.6 the growth of a parabolic quantum well using the digital alloy technique is sketched, the black lines show the local Al content while the gray line shows the average one.

2.3 Intersubband Transitions in Quantum Wells

2.3.1 Definition

In the previous section it was discussed how electrons in a (thin) quantum well form a 2 DEG. Since they are confined in the growth direction (z), the allowed energy levels in the conduction band will be quantized (the same is valid for holes in the valence band). These energy levels E_n can be tuned by changing the width, depth and shape of the quantum wells. Electrons in a 2 DEG are free to move in the perpendicular plane (x-y). This will result in an additional contribution to the overall energy of the electrons, which can be written as:

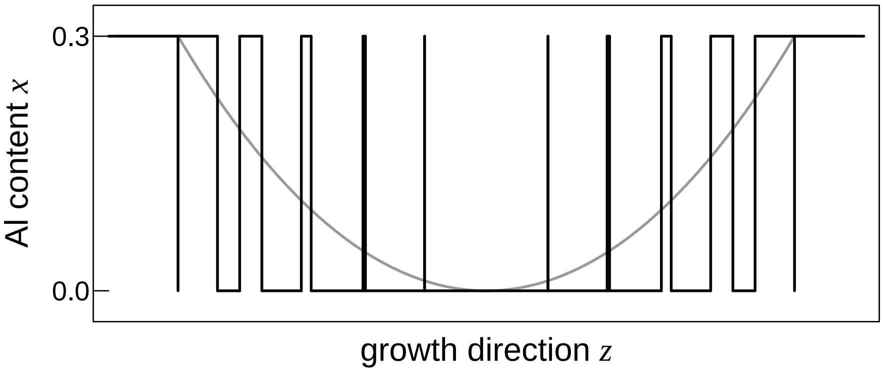

Figure 2.6: Sketch of a parabolic quantum well built using the digital alloy technique. The black lines show the Al content which can only take two values while the gray line shows the average Al content, averaged over a larger distance scale.

$$E = E_n + \frac{\hbar^2 k_\perp^2}{2m_{eff}}, \tag{2.3.1}$$

where E_n is the n-th quantized energy level, n is the principal quantum number (n=1,2,3,...) and $k_\perp$ the modulus of the wave vector in the plane perpendicular to the growth direction of the well. The term intersubband transition refers to transitions between these quantized levels within a given band. In the following we will focus only on intersubband transitions of electrons in the conduction band.

2.3.2 Optical Excitation of Intersubband Transitions

Since electrons in the conduction band of a quantum well are free to move in the perpendicular ($x - y$) plane, the wave function $f_{n,\mathbf{k}_\perp}$ describing the electrons can be written as a product of two functions. The first one describing free motion (plane wave) in the ($x - y$) plane, whereas the second one reflects the confinement in z direction, additionally this function has to be normalized:

$$f_{n,\mathbf{k}_\perp} = \frac{e^{i\mathbf{k}_\perp \cdot \mathbf{r}_{x-y}} \varphi_n(z)}{\sqrt{A}}, \tag{2.3.2}$$

where A is the area of the 2 DEG, $\mathbf{r}_{x-y}$ lies in $x - y$ plane and $\varphi_n(z)$ depends on the quantum well potential. The interaction of electrons with light can be calculated in the semiclassical picture by modifying the unperturbed Hamiltonian $H_o = \frac{\mathbf{p}^2}{2m} + V(\mathbf{r})$ in the Coulomb gauge through:

$$\mathbf{p} \rightarrow \mathbf{p} - e\mathbf{A}, \tag{2.3.3}$$

with $\mathbf{A}$ being the vector potential and $-e$ being the electron's charge. Since $\nabla\mathbf{A} = 0$, the interaction Hamiltonian H' yields:

$$H' = \frac{e}{m_{eff}}\mathbf{A}\cdot\mathbf{p}, \tag{2.3.4}$$

where the effective mass has been introduced and to first approximation the term with $\mathbf{A}^2$ has been neglected [25]. A linearly polarized electromagnetic wave can be described as:

$$-\frac{\partial\mathbf{A}}{\partial t} = \mathcal{E} = E_o\mathbf{e}\cos(\mathbf{k}\cdot\mathbf{r} - \omega t), \tag{2.3.5}$$

with $\mathcal{E}$ the electric field, $\mathbf{e}$ the polarization vector and $\mathbf{k}$ the propagation vector. Depending on the photon energy $\hbar\omega$, light can induce a transition rate from an electron state i to a state f, W_{if} given by Fermi's golden rule:

$$W_{if} = \frac{2\pi}{\hbar} \mid\langle f_i \mid H' \mid f_f\rangle\mid^2 \delta(E_f - E_i - \hbar\omega). \tag{2.3.6}$$

If the wavelength of the radiation is longer than the width of the quantum well (a condition which is fullfilled throughout the present work) the dipole approximation can be employed so that $\mathbf{k}\cdot\mathbf{r} << 1$ [25]. Therefore in order to obtain the transition rate the following matrix element has to be calculated $\langle f_i \mid \mathbf{e}\cdot\mathbf{p} \mid f_f\rangle$, but since:

$$[\mathbf{r},H_o] = \frac{i\hbar\mathbf{p}}{m_{eff}}, \tag{2.3.7}$$

calculation of Eq. 2.3.6 can be reduced to obtain the dipole moment, $\langle f_i \mid \mathbf{e}\cdot\mathbf{r} \mid f_f\rangle$.
If $n,\mathbf{k}_\perp$ and $n',\mathbf{k}'_\perp$ label the initial and final states respectively,

$$\langle f_{n,\mathbf{k}_\perp} \mid \mathbf{e}\cdot\mathbf{r} \mid f_{n',\mathbf{k}'_\perp}\rangle = \frac{1}{A}\int d^3r e^{-i\mathbf{k}_\perp\cdot\mathbf{r}_{x-y}}\varphi_n^*(z)[e_x x + e_y y + e_z z]e^{i\mathbf{k}'_\perp\cdot\mathbf{r}_{x-y}}\varphi_{n'}(z). \tag{2.3.8}$$

Thus only the term proportional to e_z yields an intersubband transition contribution, as the terms proportional to e_x and e_y vanish unless the initial and final states are identical, $n = n'$ and $k_\perp = k'_\perp$. Finally the intersubband absorption of a photon by an electron in a quantum well is determined by:

$$\langle\varphi_n(z) \mid z \mid \varphi_{n'}(z)\rangle = \int dz\varphi_n^*(z)z\varphi_{n'}(z) \tag{2.3.9}$$

so that in order to induce an intersubband transition, the electric field needs to have a component in the growth direction z. This is the polarization selection rule. Different techniques to realize this experimentally will be introduced in the following chapters.

2.3.3 Parabolic Quantum Wells

In the following, parabolic quantum wells (PQW) will be discussed since they are the main topic of the present work. In section 2.2 an example of how a PQW can be realized using a digital alloy technique was introduced. In an harmonic potential the quantization of the allowed energy leads to equally spaced energy levels given by [16]:

$$E_n = \hbar\omega_o(n - 1/2), \tag{2.3.10}$$

where ω_o is the oscillator frequency. There are different ways to estimate ω_o, elaborated techniques including simulations will be analyzed later, however a first approach is to relate ω_o to the width W and the energetic depth Δ of the well, Fig. 2.7 a) through [12]:

$$\omega_o = \sqrt{\frac{8\Delta}{m_{eff}W^2}}. \tag{2.3.11}$$

In the case of PQWs made of $Al_xGa_{1-x}As$-GaAs the effective mass of GaAs can be employed.

So far bare PQW (without electrons) have been analyzed, but in order to detect transitions, electrons have to be introduced, for example through modulation doping, section 2.2. As a consequence electrons give rise to an additional potential given by the electron-electron interaction. This potential is also parabolic and compensates the original parabolic potential close to the minimum, depending on the electron density, Fig. 2.7 b). However one advantage of PQWs is that regardless on the number of electrons in the well and how they modify the potential, the resonant absorption always occurs at the bare frequency ω_o. This is a consequence of the generalized Kohn's theorem which states that in a parabolical potential, excitations are independent of electron-electron interactions since they couple to the centre of mass motion [26, 27]. Thus, effects like the depolarization shift can be neglected [28].

2.3.4 Dephasing

The main focus of the present work is to study the dephasing mechanisms of intersubband transitions. Therefore, in this section an introduction to dephasing phenomena is presented. After interaction with light, the state of an electron in a PQW can be described as a linear superposition of eigenstates of the unperturbed Hamiltonian, H_o [29]:

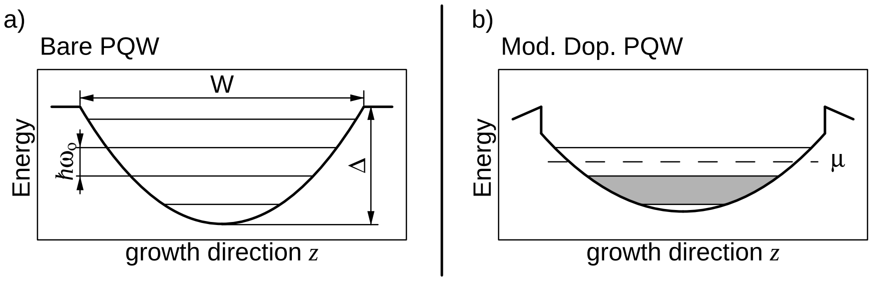

Figure 2.7: a) Diagram of a bare PQW, the width W and depth Δ of the well are indicated as well as the energy levels. b) Shows the well after being filled with electrons through modulation doping, the energy levels and the chemical potential μ are indicated.

$$\Psi(z,t) = a_1(t)e^{i\frac{E_1 t}{\hbar}}\varphi_1(z) + a_2(t)e^{i\frac{E_2 t}{\hbar}}\varphi_2(z), \tag{2.3.12}$$

where just the first two levels are considered which is a good approximation for the energies involved in the present work and also because in parabolic quantum wells transitions are just allowed between adjacent eigenstates, Δn=±1 (further details are included in Appendix B). We focus on the z dependence as discussed before and recall

$$\mid a_1(t) \mid^2 + \mid a_2(t) \mid^2 = 1, \tag{2.3.13}$$

with $\mid a_1(t) \mid^2$ and $\mid a_2(t) \mid^2$ being the probabilities of finding the electron in the first or second level respectively. Electrons in such a state have a dipole moment $\mu_d(t)$

$$\begin{aligned}\mu_d(t) = \langle \Psi(z,t) \mid -ez \mid \Psi(z,t) \rangle \quad &= \quad a_1^*(t)a_1(t)\mu_{11} + a_2^*(t)a_2(t)\mu_{22} \\ &\quad +a_1^*(t)a_2(t)e^{-i\omega_o t}\mu_{12} + a_2^*(t)a_1(t)e^{i\omega_o t}\mu_{21},\end{aligned} \tag{2.3.14}$$

with $\mu_{ij} = \langle \varphi_i(z) \mid -ez \mid \varphi_j(z) \rangle$ the matrix element and $E_2 - E_1 = \hbar\omega_o$. For a parabolic potential, $\varphi_i(z)$ can be obtained analytically yielding functions with fixed symmetry and therefore, $\mu_{11} = \mu_{22} = 0$ and $\mu_{12} = \mu_{21}$. The dipole moment is given by the last two terms of Eq. 2.3.14:

$$\mu_d(t) = a_1^*(t)a_2(t)e^{-i\omega_o t}\mu_{12} + a_2^*(t)a_1(t)e^{i\omega_o t}\mu_{12}, \tag{2.3.15}$$

oscillating at the transition frequency ω_o. An ensemble of n_e electrons will then build up a macroscopic intersubband polarization $P_m(t)$

$$P_m(t) = n_e \mu_d(t), \tag{2.3.16}$$

only if the dipoles can oscillate coherently in phase. In reality, coherence will be lost after a dephasing time τ_d, and the macroscopic polarization will vanish. There are several mechanisms, with characteristic times τ_i, that will damp the coherence of the macroscopic polarization. They can be related to the dephasing time using the Matthiessen's rule [30]

$$\frac{1}{\tau_d} = \gamma = \sum_i \frac{1}{\tau_i}, \tag{2.3.17}$$

where γ is the damping rate of the macroscopic polarization. This damping can also be regarded as broadening of the linewidth of the transition given by Eq. 2.3.6. The different damping mechanisms can be divided in:

(i) Phase breaking scattering processes: each scattering event which changes the relative phase between the electron dipoles will lead to a damping of the coherent macroscopic instersubband polarization [5]. The relevant processes (among others) are:

Electron-phonon scattering: Scattering of electrons with the lattice will lead to the creation of optical as well as acoustic phonons. The phonon scattering rate depends strongly on the temperature, so this effect can be reduced by working at low temperatures [31]. The mobility arising from lattice scattering has a dependence with temperature given by $\propto T^{-3/2}$ [32].

Ionized impurity scattering: Electrons can also scatter with donors introduced in the doping process. This effect is currently reduced with modulation doping techniques, Sec. 2.2, in which ionized donors and electrons are separated [5, 18]. Scattering with ionized impurities is particularly relevant at low temperatures since the mobility arising from this effect has a $\propto T^{3/2}$ dependence [32].

In Fig. 2.8 the overall mobility arising from both lattice scattering and ionized impurities is sketched as a function of the temperature. The resulting mobility is obtained adding both contributions using the Matthiessen's rule. For low temperatures, the reduction in the mobility is due to ionized impurity scattering whereas for high temperatures lattice scattering dominates.

Alloy-disorder scattering: Alloy scattering in ternary compounds $A_xB_{1-x}C$ is induced by the fluctuation of the uniform distribution of atoms A and B over the lattice sites. However, in modulation-doped $Al_xGa_{1-x}As$–GaAs heterointerfaces scattering is limited by the small pene-

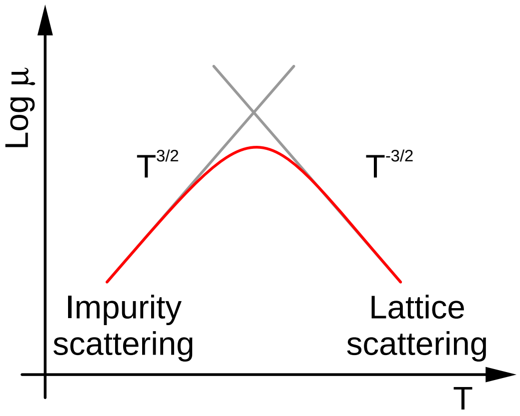

Figure 2.8: Sketch of the temperature dependence of the mobility due to lattice and ionized impurity scattering.

tration of the electron wavefunction into the $Al_xGa_{1-x}As$ [33].

Interface roughness scattering: This effect is particularly relevant in $Al_xGa_{1-x}As{-}GaAs$ thin quantum wells, since small roughness of heterointerfaces can cause a large fluctuation in the quantization energy of confined electrons in the 2 DEG, which would lead to a strong momentum scattering [34, 35].

Electron-electron scattering: Scattering between electrons will affect the macroscopic coherence especially in the case of non-parallel subbands [36].

All these scattering mechanisms contribute to what is denominated homogeneous broadening [13].

(ii) Inhomogeneous broadening: A distribution of transition energies in the optically coupled range, leads to a fast decay of the macroscopic polarization caused by destructive interference between the individual components. The most important contribution to inhomogeneous broadening stems from disorder effects like fluctuations of the quantum well width, see Fig. 2.9 or the alloy composition.

In any case both homogeneous and inhomogeneous processes take place at the same time. To date a detailed quantitative understanding of the different broadening processes and of their relative contribution to the overall damping has not been reached. The damping rate γ can be introduced in a phenomenological way through a semiclassical approach for an oscillating dipole [37]. The differential equation of the amplitude z of an oscillator with a frequency ω_o and damping constant γ driven by an external force F, is given phenomenologically following

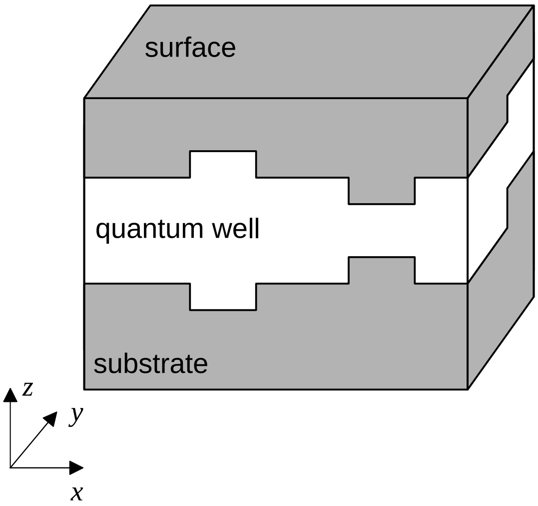

Figure 2.9: Sketch of quantum well in which fluctuations in the width lead to inhomogeneous broadening.

a classical approach by:

$$\frac{d^2z}{dt^2} + \gamma\frac{dz}{dt} + \omega_o^2 z = \frac{F}{m_{eff}}, \tag{2.3.18}$$

where m_{eff} is the mass of the oscillator. In the case the driving force is electromagnetic radiation of the form $\mathcal{E}(\omega)e^{i\omega t}$ the previous equation becomes:

$$\frac{d^2z}{dt^2} + \gamma\frac{dz}{dt} + \omega_o^2 z = -\frac{e}{m_{eff}}\mathcal{E}(\omega)e^{i\omega t}, \tag{2.3.19}$$

with $-e$ being the electron's charge. The steady-state solution can be written in the form

$$z = z(\omega)e^{i\omega t}, \tag{2.3.20}$$

with the frequency dependent amplitude

$$z(\omega) = \frac{e}{m_{eff}}\frac{\mathcal{E}(\omega)}{\omega^2 - i\gamma\omega - \omega_o^2}. \tag{2.3.21}$$

The macroscopic polarization of the medium $P_m(\omega)$ is proportional to $z(\omega)$ and it is also related to the complex susceptibility $\chi(\omega)$ through:

$$P_m(\omega) = \epsilon_o \chi(\omega) \mathcal{E}(\omega), \tag{2.3.22}$$

yielding the following expression for the susceptibility [38]

$$\chi(\omega) = \frac{n_e e^2}{\epsilon_o m_{eff}} \frac{1}{\omega^2 - i\gamma\omega - \omega_o^2}. \tag{2.3.23}$$

Since the complex index of refraction n can be written as:

$$n = \sqrt{1 + \chi(\omega)}. \tag{2.3.24}$$

By studying the reflection or transmission of light for frequencies around ω_o, the damping rate γ can be estimated experimentally.

2.4 Metal Semiconductor Contacts and Control of the Charge Carrier Density

2.4.1 The Schottky Contact

As explained previously, metals and semiconductors have different band structures, Fig. 2.10 a). Furthermore they generally also differ in the work function $q\phi$: The energy between the chemical potentials μ and the vacuum level E_{vac}. As both materials are brought together, carrier transfer between them is allowed. In the case of n-doped semiconductors for example, donor electrons are transferred into the metal until both chemical potentials are aligned in thermal equilibrium, Fig. 2.10 b). In addition their vacuum levels must be continuous. Fullfiling these two requirements determines the band structure of a Schottky contact [39].

As a result, electrons in the conduction band are confined to the semiconductor by the so called built-in potential given by $V_{bi} = \phi_m - \phi_{sc}$. This barrier can be modified by applying a voltage between the metal and the n-doped semiconductor. When a forward bias V_f is applied, with the metal at a higher potential than the semiconductor, the barrier is reduced and electrons see a confinement potential of $V_{bi} - V_f$. Therefore, a forward bias enables the electron flow from the semiconductor to the metal. The opposite occurs when a reverse bias V_r is applied (negative voltage applied to the metal). This further increases the confinement potential to $V_{bi} + V_r$ restricting the electron flow from the semiconductor to the metal and pushing the electrons away from the interface deeper into the semiconductor. Thus, a region called depletion zone in which electrons are pushed away is created.

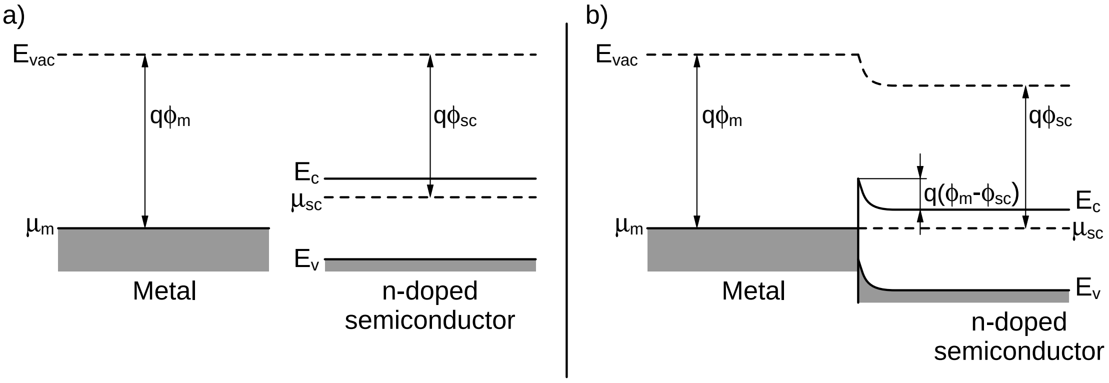

Figure 2.10: a) Energy band diagram of a metal and a n-doped semiconductor. b) Energy band diagram of a contact in thermal equilibrium between a metal and a n-doped semiconductor.

2.4.2 The Ohmic Contact

In the previous case of a metal-semiconductor Schottky contact, a significant current can only flow into the metal. However, operating a semiconductor also requires a current flow into it. This can be achieved with Ohmic contacts, i.e. a metal-semicondutor contact in which the current flow is proportional to the applied voltage, with very low resistance independent of the direction of the current flow. One way of realizing an Ohmic contact is by choosing an appropriate metal with a sufficiently low work function so that it yields a low barrier, Fig. 2.11 a). For example $Au_{0.88}Ge_{0.12}$ is generally employed for contacting n-doped GaAs. The other way is to use heavily doped semiconductors, in this way the barrier is so thin that electrons can tunnel across it, Fig. 2.11 b). If possible both approaches are taken at the same time to increase the quality of the Ohmic contact [15].

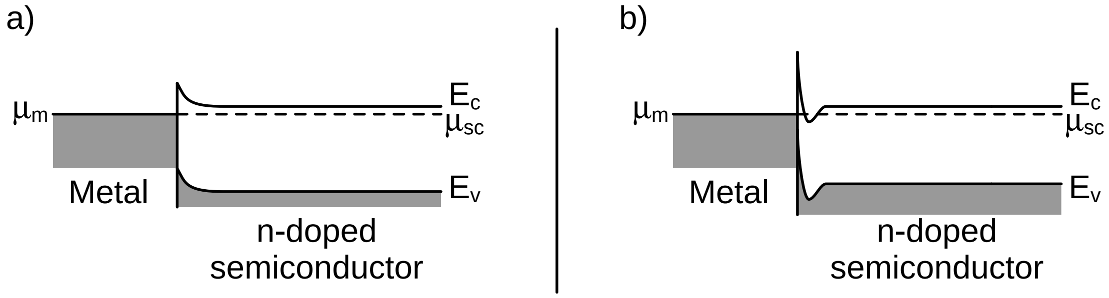

Figure 2.11: a) Energy band diagram of an Ohmic contact formed between a n-doped semiconductor and an appropriate metal. The barrier height is low enough so that thermally excited electrons in the conduction band can overcome it. b) Energy band diagram of an Ohmic contact between a metal and a n-doped semiconductor. The semiconductor is so highly doped that the barrier is thin enough and electrons can tunnel across it.

3 Terahertz Spectroscopy and Terahertz Microscopy

Since this work deals with intersubband transitions in the terahertz (THz) range, this chapter is devoted to THz technology. After an introduction in which the main characteristics and advantages of working in the THz range are highlighted, different methods for generating and detecting THz radiation are analyzed. Particular details are given for the techniques used throughout this work: Photoconductive switches in the case of generation and electro-optic sampling for detection. Finally different techniques for overcoming the diffraction limit through near field techniques are discussed. Two main approaches for the interpretation of results are presented, the dipole and the antenna model.

3.1 Introduction

Although not a rigid definition, the terahertz (THz) electromagnetic radiation comprises the range from about 0.1 to 10 THz ($\lambda_{THz} = 0.03 - 3$ mm), Fig 3.1. For several years this band was referred to as the "Terahertz Gap ". From the microwave side of the spectrum approaching the THz gap, it is difficult to fabricate electronic devices which operate at frequencies above 100 GHz. From the optical side, although interband laser diodes have long been designed, the same principle can not be extended to the THz range as there are no suitable semiconductors (or the bangap is comparable to the thermal excitation at room temperature, $E_g \sim kT$). Even when some techniques for continuous wave (cw) THz generation were already available, like for example backward wave oscillators (BWO) [40] or frequency mixing [41], it was the invention of the mode-locked Ti:sapphire laser [42, 43] which boosted the generation of THz pulsed radiation.

The main difference between electromagnetic radiation in the visible and in the THz range is that in the later case, through time domain techniques, the amplitude and phase of the electric field of a THz pulse can be simultaneously measured [1]. In Fig. 3.2a) the electric field of a typical time resolved few cycle THz pulse is included together with its corresponding amplitude spectrum in frequency domain, Fig. 3.2b). Measuring the amplitude and phase of an electromagnetic pulse has several advantages, like for instance the ability to determine the complex dielectric function of a sample [3, 4, 45, 46]. In addition, the coherent detection of THz pulses is performed

---

[1] Recently complex techniques that allow for time-resolving the electric field of a pulse in the visible range have been developed [44].

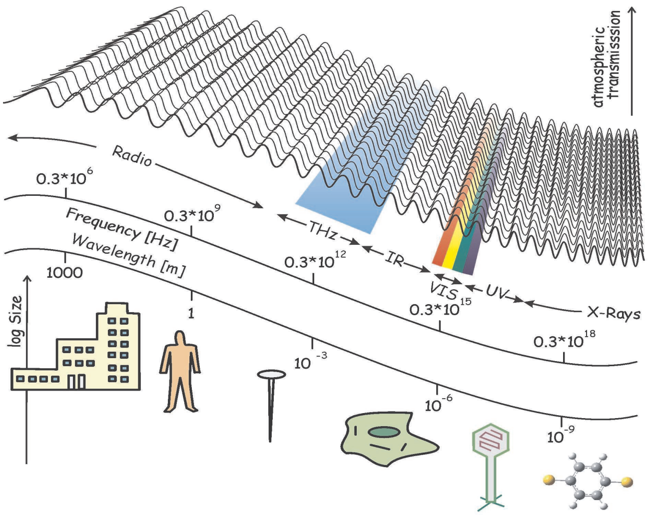

Figure 3.1: A part of the electromagnetic spectrum. (Courtesy of Prof. Dr. R. Kersting, Rensselaer Polytechnic Institute)

using time gated techniques. This constitutes a major difference to commonly employed far infrared (F.I.R.) spectroscopy techniques, in which a bolometer is used constantly for detection. Coherent gated detection has the advantage that it is immune to ambient black body radiation [47, 48] and therefore a much higher signal to noise ratio can be achieved with time domain THz spectroscopy.

3.2 Terahertz Generation

A typical source of pulsed THz radiation consists of a short-pulse laser (<100 fs) in the visible or near infrared range ($\approx$ 800 nm) which is typically a Ti:sapphire laser and a method to convert the visible pulses into pulses in the THz range. Two main approaches will be discussed in this section, optical rectification and the current surge effect.

3.2.1 Optical Rectification

Optical rectification is a difference frequency mixing process that occurs in media with large second order susceptibility χ^2. For high enough electric field intensities, the polarization P_m in a material contains not only a term proportional to the electric field $\mathcal{E}(t)$ but also a second order term that reads:

$$P_m^{(2)}(t) = \chi^2 \mathcal{E}^2(t), \tag{3.2.1}$$

where $P_m^{(2)}(t)$ is the second order polarization and higher order terms were neglected. If two

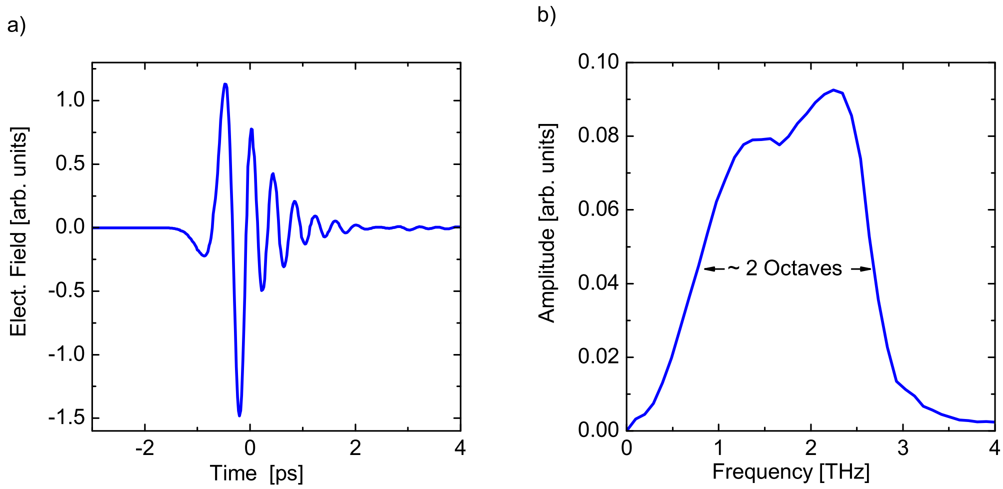

Figure 3.2: a) Electric field of a time resolved few-cycle THz pulse and b) corresponding amplitude spectrum in frequency domain.

optical beams with the same amplitude E_o but different frequency, ω_1 and ω_2 respectively meet collinearly in a non linear medium, the second order polarization yields:

$$\begin{aligned} P_m^{(2)}(t) &= \chi^2 \left\{E_o \sin(\omega_1 t) + E_o \sin(\omega_2 t)\right\}^2 \\ &= \chi^2 E_o^2 \Big\{1 - \frac{1}{2}\cos(2\omega_1 t) - \frac{1}{2}\cos(2\omega_2 t) \\ &\quad + \cos((\omega_1 - \omega_2)t) - \cos((\omega_1 + \omega_2)t)\Big\}. \end{aligned} \tag{3.2.2}$$

Thus the induced polarization has a constant term, two terms at twice the original frequencies, one term at the sum of the frequencies and one at the difference. Considering Maxwell's equations, the time dependent terms will radiate at different frequencies as compared to the incoming beams. For THz generation the term that includes the difference frequency $\omega_1 - \omega_2$, can be exploited. If two cw laser beams in the visible range, that differ in frequency in the THz range, are employed cw THz radiation can be generated.

The same concept can be extended to the generation of pulsed THz radiation if instead of two cw laser beams, a short-pulse laser (<100 fs) in the visible is chosen. These short-pulses have a bandwidth of tens of terahertz. Therefore, when traveling in a non linear medium, difference frequency generation takes place between the different frequency components within the pulse bandwidth. Since difference frequency generation occurs between all the frequency components, a pulse in the visible range can generate pulsed-THz radiation. Suitable materials for THz generation typically include ZnTe [49, 50] and GaP [51].

3.2.2 Current Surge Effect

In this case, also known as ultrafast charge transport, pulsed THz radiation is generated from rapidly varying electric currents. A short-pulse laser in the visible range is used for photoexciting electron-hole pairs in a semiconductor. Following photoexcitation, carriers are driven by an electric field. Suitable electric fields can be raised in two ways.

Intrinsic electric fields. The built in electric field which arises due to the Fermi level pinning at the surface of doped semiconductors like n-doped GaAs is employed for driving the photogenerated carriers [52]. Another alternative is to exploit the difference of the electron and hole mobilities. After photoexcitation, electrons will diffuse into the semiconductor faster than holes and therefore an electric field will originate. This is the so called photo Dember effect for which intrinsic InAs is typically used [53].

Externally applied electric fields. Two metallic contacts are deposited onto a semiconductor surface so that a bias voltage can be applied [54, 55]. A sketch of such a THz photoconductive emitter is included in Fig. 3.3. This technique will be explained in further details since it will be used throughout the present work.

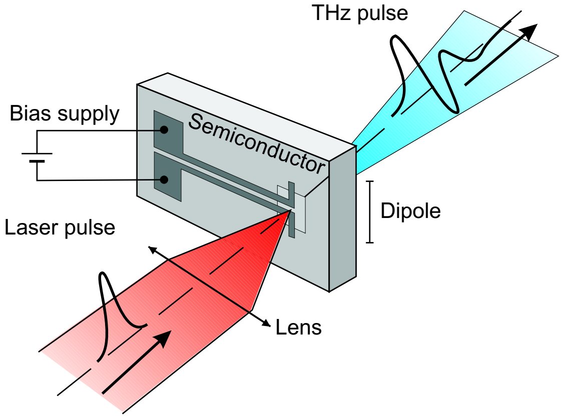

Figure 3.3: Sketch of a photoconductive THz emitter.

The pulsed laser beam is focused onto the semiconductor, in the gap between the metallic contacts. If the incoming photon energy is higher than the semiconductor band gap, electron-hole pairs are created close to the surface (extending just a few μm into the semiconductor bulk). Once carriers are created, a current will be established due to the applied electric field, in a similar manner as in Sec. 2.1.4 using Ohm's law

$$j_l(t) = \sigma_l(t)\mathcal{E}_t(t), \tag{3.2.3}$$

with $j_l(t)$ the line current, $\sigma_l(t)$ the line conductivity and $\mathcal{E}_t(t)$ the total electric field seen by the carriers. According to Maxwell's equation [56], a varying current emits electromagnetic radiation. The electric field of the radiated emission into the far field $\mathcal{E}_{THz}(t)$, is related to the current through

$$\mathcal{E}_{THz}(t) \propto \frac{dj_l(t)}{dt}, \tag{3.2.4}$$

so that the time dependence of the line current $j_l(t)$ has to be studied. The line conductivity can be expressed as function of the electron density n_e and mobility μ_e,

$$\sigma_l(t) = en_e(t)\mu_e, \tag{3.2.5}$$

where the contribution of holes is neglected due to their lower mobility (in commonly employed semiconductors like intrinsic GaAs, $\mu_h \approx 400$ cm^2/Vs while $\mu_e \approx 8000$ cm^2/Vs). The electron density depends on two competing mechanism: The photoexcitation described by the incoming laser intensity $I_i(t)$ and the recombination given by the electron lifetime τ_e

$$\frac{dn_e(t)}{dt} = -\frac{n_e(t)}{\tau_e} + \frac{I_i(t)}{\hbar\omega}, \tag{3.2.6}$$

with $\hbar\omega$ being the photon energy and assuming that every photon generates an electron-hole pair. Thus, an appropriate choice of the semiconductor which comprises parameters like the electron mobility μ_e and lifetime τ_e together with the incoming pulse shape and intensity will tailor the radiated THz emission regarding its spectral composition as well as its intensity [57]. The total electric field $\mathcal{E}_t(t)$, will also affect the THz emission (Eq. 3.2.3 and 3.2.4). The electric field applied through the contacts $\mathcal{E}_{bias}$, can be considered constant in the time scale involved during the photoexcitation. However, different processes like screening by charge carriers will alter the total electric field. In first approximation the total electric field $\mathcal{E}_t(t)$ can be expressed as the product between the applied field $\mathcal{E}_{bias}$ and a function of time, $f(t)$.

$$\mathcal{E}_t(t) = f(t)\mathcal{E}_{bias}. \tag{3.2.7}$$

Thus a higher emission will be achieved by increasing the applied electric field $\mathcal{E}_{bias}$, at the same time care has to be taken that the dark resistance of the semiconductor is low enough to prevent excessive heating. Photoconductive THz emitters have one advantage over THz emission involving other methods: In order to reduce noise Lock-in techniques can be employed for detection. In the case of photoconductive THz emitters the applied bias can be modulated at high frequencies on the order of ≈100 kHz whereas for most alternative methods the incoming laser beam has to be mechanically chopped at lower frequencies on the order of ≈1 kHz, which results in higher noise.

3.3 Terahertz Detection

As introduced in the beginning of this chapter, one advantage of dealing with THz pulsed radiation is that the electric field can be time-resolved. Considering the pulse length of THz radiation, detection schemes need a response time in the sub-picosecond range. Currently, this can not be achieved with electronic devices (like for example an oscilloscope), such that an optical pump-probe approach is followed. The incoming pulsed laser beam is split in two: A small fraction, the probe beam, is used for detection whereas the rest, the pump beam, is used for THz generation as discussed in the previous section. Both the pulsed probe beam and the generated pulsed THz radiation meet on a THz detection element. By changing the optical path length between the pump and the probe beam, the THz pulse can be time resolved. This technique is often referred as time domain THz spectroscopy. Two THz detection methods will be discussed in the following section, photoconductive switches and electro-optic sampling (EOS).

3.3.1 Photoconductive Switches

For this technique a similar device as in Fig. 3.3 is used, only that in this case a voltage is not applied to the contacts but rather a current flowing between the contacts is measured [58, 59]. As the probe beam impinges onto the gap between the contacts, carriers will be photoexcited reducing the resistance between the contacts. If the THz radiation is also focused onto the gap between the contacts, the THz electric field will originate a current. When both the carrier lifetime and the probe pulse are short compared to the THz pulse, this current is proportional to the THz electric field $\mathcal{E}_{THz}$. In practice, the resolution of this technique will be limited by the carriers' lifetime to about 100 fs [60]. Another disadvantage of this technique is that effects, like the frequency dependence of the electron's mobility may distort the THz pulse shape [57], also contacts may act as antennas with a frequency dependent coupling.

3.3.2 Electro-optic Sampling

This wide spread technique circumvents the problems of the previous method and therefore it was the method of choice for the current work. It is based on the linear electro-optic effect (also known as the Pockels effect): An applied electric field induces a linear change in the refractive indices between the ordinary and extraordinary axis (birefringence) of a material, typically an electro-optic (EO) crystal. This crystal can be oriented so that a THz pulse propagating through it, will induce a change of the refractive indices Δn given by [61]

$$\Delta n = n^3 r_{41} \mathcal{E}_{THz}, \tag{3.3.1}$$

where $\mathcal{E}_{THz}$ is the THz electric field, n is the index of refraction of the EO crystal and r_{41} is the electro-optic coefficient of the material. This change in the refractive indices can be sensed by the probe pulse, with electric field components on both axis, propagating collinearly with the THz pulse. After propagating a length d through the crystal, a phase difference Γ arises between the two polarization directions

$$\Gamma = \frac{2\pi}{\lambda_{opt}} d \Delta n, \tag{3.3.2}$$

with λ_{opt} the vacuum wavelength of the probe pulse. Both polarization components of the probe pulse can be then separated with the aid of a quarter-wave plate ($\lambda/4$) and a Wollaston prism and finally the difference in phase can be sensed with two photo-diodes connected in a differential manner, Fig. 3.4. In this way, by changing the delay between pump and probe, the electric field of the THz pulse $\mathcal{E}_{THz}$ can be retrieved. This technique has the advantage that the time resolution is limited only by the probe pulse length (which depending on the laser employed can be <100 fs). The typical choice for an electro optic crystal is ZnTe [62–64] since for frequencies around 1 THz the phase velocity is equal to the group velocity of the generally used Ti:sapphire radiation around 800 nm. This allows for the use of very thick crystals yielding large signals. One drawback of ZnTe is that it can only detect frequencies up to 4 THz due to an optical phonon resonance. For a higher bandwidth GaP can be used with a flat response up to 7 THz [65].

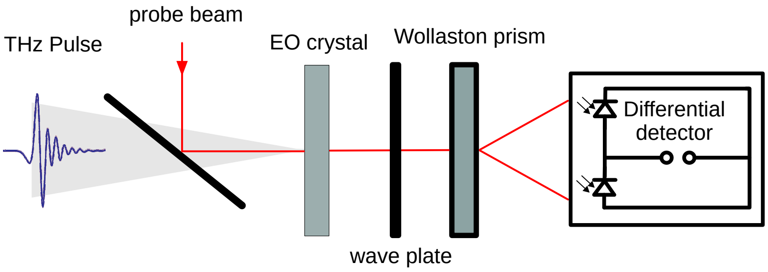

Figure 3.4: Sketch of the setup employed for electro-optic sampling.

3.4 Introduction to Near Field Microscopy

3.4.1 Limitations of Conventional Optical Microscopy

In order to achieve high spatial resolution in conventional optical microscopes, propagating electromagnetic waves are focused with the aid of lenses and mirrors. The smallest spot diameter $\mathit{\Delta} x$ that can be attained is limited by diffraction to roughly

$$\mathit{\Delta} x = \frac{0.61\lambda}{n \sin\alpha}, \tag{3.4.1}$$

where λ is the wavelength of the electromagnetic waves, $n \sin\alpha$ is the numerical aperture of the objective lens or mirror [66]. This quantity $\mathit{\Delta} x$, determines the size of the smallest objects that can be spatially distinguished (Abbe criterion), Fig. 3.5.

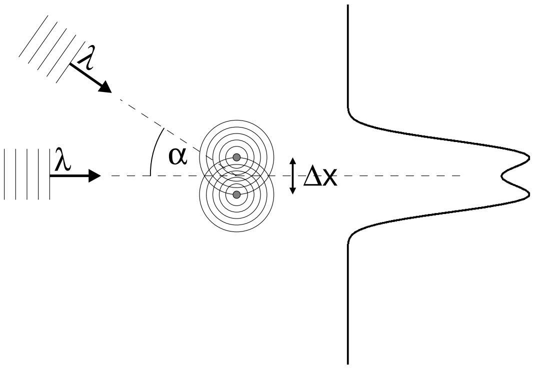

Figure 3.5: Spatial resolution in a conventional microscope given by the Abbe criterion.

The spatial resolution can be improved by increasing the numerical aperture: Using surrounding mediums with higher index of refraction n or larger angles of acceptance α [67]. However, the smallest objects that can be spatially resolved are generally not smaller than the wavelength [68]. For THz microscopy, this corresponds to a spatial resolution of $\mathit{\Delta} x = 0.3$ mm at a frequency of 1 THz which is comparable to the resolution of the human eye. This, together with the fact that THz radiation is transparent to most clothing materials, turned THz radiation into an appropriate choice for object detection [69–71].

3.4.2 Near Field Scanning Optical Microscopy (NSOM)

The diffraction limit introduced in the previous section can be overcome by employing the so called near field techniques. In this case imaging of a sub-wavelength object can be performed if not only the propagating waves but also the evanescent waves are collected. Since evanescent waves do not propagate, they have to be acquired in a region very close to the object. This is typically done by a local probe kept in close proximity to the object to be imaged. Now the resolution Δx no longer depends on the wavelength λ but rather on a characteristic length d_c of the probe. Finally, the probe is raster scanned over the object, and for every defined position an optical response signal is recorded. Thus, a contrast image of an object with sub-wavelength dimensions can be obtained. Two main approaches are followed for the construction of probes, aperture and aperture-less (pointed) probes.

Aperture probes

This technique was first envisioned by Synge in the year 1928 [72] and realized only recently in the THz range by Hunsche and coworkers [73]. A sketch of this method is included in Fig. 3.6a). THz radiation is sent through a conical metal tip with a sub-wavelength aperture. The distance between tip and sample is fixed on a subwavelength scale so that the transmitted radiation interacts with the sample before diffracting. In this case the resolution is mainly given by the aperture diameter so that higher resolutions can be achieved by decreasing the size of the aperture. However, the limit of this technique is given by the amount of radiation which is transmitted through the aperture. Unfortunately, the power transmission of a circular aperture decreases as the sixth power of the aperture's diameter [74]. This limitation is of particular relevance for THz radiation, since most THz sources have a rather low power output. In addition other disadvantages are that the aperture behaves like a cylindrical waveguide with frequency dependent transmission and that with aperture probes topology measurements can not be done simultaneously.

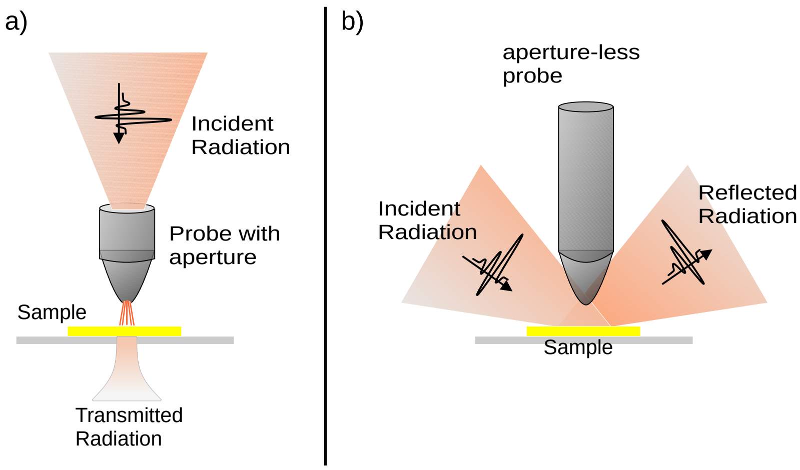

Figure 3.6: a) Sketch of a setup used for aperture near field microscopy and b) for aperture-less near field microscopy.

Aperture-less (pointed) probes

An alternative to aperture probes was first developed in the 1990s [75] and extended to the THz range by van der Valk in 2002 [76] and Chen in 2003 [77]. There are several ways of implementing aperture-less THz near field microscopy [61, 78–80]. In this work, the approach introduced in [81] is going to be followed. The main concept is sketched in Fig. 3.6b), a metallic probe with a sharp tip is held close to the sample to be studied and illuminated with THz radiation. The metallic probe localizes and enhances the electromagnetic field under the tip's apex. The field enhancement arises from a combination of a lightning-rod effect and surface-plasmon excitations [82]. The reflected THz radiation, containing information about the near field interaction between sample and tip is measured in the far field. Aperture-less THz microscopy has the advantage that the spatial resolution is mostly given by the tip apex diameter and that it can be combined with other microscopy techniques to perform simultaneous topology measurements.

3.4.3 Imaging Mechanisms in Aperture-less Near Field Scanning Optical Microscopy (ANSOM)

In the previous section it was explained how aperture-less near field scanning optical microscopy (ANSOM) techniques can be applied for obtaining images of objects with sub-wavelength resolution. Interpretation of these images requires an understanding of the interaction between radiation, probe and sample. Through a proper analysis of ANSOM experiments involving not only continuous wave (cw) but also broadband radiation insight on physical local properties, like the complex dielectric function, can be gained.

A detailed description of the imaging mechanism in ANSOM experiments has not been developed so far and it is therefore beyond the scope of this work. Most of the current approaches involve numerical simulations since objects with particular geometries, like the probe, are very complex to treat theoretically [67]. However, it is desirable to develop approximate models that can be treated analytically and account for the most relevant features of ANSOM experiments. In the following, two different models are going to be described, the dipole model and the antenna model.

The dipole model

This model was originally developed for ANSOM experiments using radiation in the visible and near infrared range [83]. The metallic tip is treated as a sphere of diameter $2r_t$ and complex dielectric function ϵ_t, Fig. 3.7, that is polarized by the incoming electric field.

Assuming an electric field with an amplitude $\mathcal{E}$ perpendicular to the sample and oscillating frequency ω, the induced dipole moment μ_d is

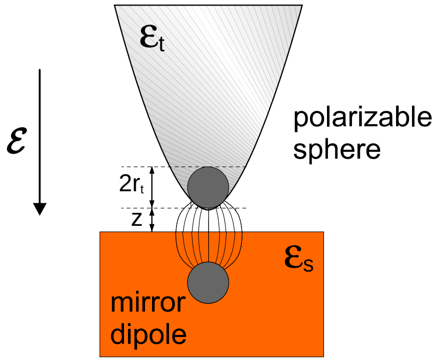

Figure 3.7: The dipole model for ANSOM. The probe tip is approximated by a sphere and the interaction with the sample is introduced through an image dipole.

$$\mu_d(\omega) = \alpha\mathcal{E}(\omega), \tag{3.4.2}$$

where α is the polarizability. For a sphere with the properties given before, it reads [84]

$$\alpha = 4\pi\epsilon_o r_t^3 \frac{\epsilon_t - 1}{\epsilon_t - 2}. \tag{3.4.3}$$

So far only the interaction between the incoming electromagnetic radiation and the metallic tip has been considered. However, the presence of a sample, described by a complex dielectric function ϵ_s, will modify the field distribution and enhancement in the region close to the tip. In order to introduce this effect, the dipole model can be extended to include the interaction with the sample taking into account a mirror dipole. The latter can be calculated using the method of images [56], yielding an induced polarization $p' = \beta p$ with $\beta = (\epsilon_s - 1)/(\epsilon_s + 1)$, located inside the sample at a distance $2(r_t + z)$ from the sphere centre. As a consequence the total electric field at the tip will result in a superposition of the incoming electric field $\mathcal{E}$ and the electric field due to the mirror dipole, so therefore the actual dipole at the tip is modified:

$$\mu_d(\omega) = \alpha\left(\mathcal{E}(\omega) + \frac{p'}{16\pi(r_t + z)^3}\right) = \frac{\alpha}{1 - \frac{\alpha\beta}{16\pi(r_t+z)^3}}\mathcal{E}(\omega). \tag{3.4.4}$$

Finally the total electric field of the tip-sample system includes the contribution of both the tip and the image dipole. For this coupled system an effective polarizability α_{eff}, can be defined [85]:

$$\alpha_{eff} = \frac{\alpha(1+\beta)}{1-\alpha\beta/[16\pi(z+r_t)^3]}. \tag{3.4.5}$$

Once the effective polarizability of the tip-sample system can be estimated, Mie-theory of scattering is introduced to calculate the scattering and absorption cross-sections, C_{sca} and C_{abs} respectively. In the Rayleigh limit, with a tip radius much smaller than the wavelength of the incoming radiation ($r_t << \lambda$) [85],

$$C_{sca} = \frac{8\pi^3}{3\lambda^4}\left|\alpha_{eff}\right|^2 \qquad C_{abs} = \frac{2\pi}{\lambda}\Im\mathrm{m}(\alpha_{eff}). \tag{3.4.6}$$

These last expressions have been successfully employed to study signal contrast in ANSNOM experiments at near infrared frequencies [86]. However, trying to extend the dipole model to THz frequencies, faces several shortcomings. Eq. 3.4.6 shows that both the scattering and absorption cross-sections have an inverse dependence with the wavelength, $1/\lambda^4$ and $1/\lambda$ respectively. For $\lambda = 10\ \mu$m a contrast signal of around 3% has been reported [86]. Following the dipole model, for $\lambda = 300\ \mu$m (1 THz), a contrast signal of 0.1% is to be expected based on the absorption cross section. In THz-ANSOM experiments, under similar conditions as in the near infrared experiments (i.e. tip apex and complex dielectric function together with sample) a contrast signal of 3% has also been achieved [87, 88].
The dipole moment also predicts an increase of both the scattering and absorption cross-sections as the distance z is reduced, for instance when the tip is brought closer to the sample. However experiments performed by Cho *et al* [89] using THz broadband radiation show an increase of the reflected THz signal, see Fig. 3.6b), when z is reduced to less than 1μm.

The antenna model

In order to circumvent the problems the dipole model has in explaining most relevant features of THz-ANSOM experiments, an alternative called the antenna model was developed [78, 90]. Within this model, in the THz range the tip-sample system is treated like an antenna with three macroscopic parameters, capacitance C, inductance L and resistance R, Fig. 3.8.

Following the antenna model, the interaction between the incident THz radiation and the tip-sample system is considered in terms of antenna absorption and subsequent dissipation in terms of reemission and ohmic heating. The ratio between the dissipated and incident power, $\eta(\omega)$ is [81, 90]

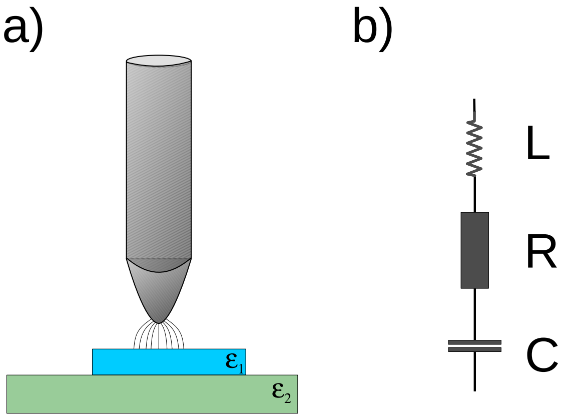

Figure 3.8: The antenna model: a) The tip-sample system can be represented by an antenna, b) equivalent electric circuit characterized by a capacitance, inductance and a resistance.

$$\eta(\omega) = \frac{P_{diss}}{P_{inc}} = \frac{RZ_o}{4\pi(R^2 + (\omega L - \frac{1}{\omega C})^2)}, \tag{3.4.7}$$

with P_{diss} and P_{inc} being the dissipated and incident power respectively, and $Z_o = 377\ \Omega$ being the vacuum impedance. According to [90], parameters like the resistance R and the inductance L depend mostly on the probe characteristics (i.e. length, shape and complex dielectric function) and can be considered constant during a THz-ANSOM experiment. Typical values of R≈1000 Ω and L≈0.3 nH are obtained experimentally. The remaining parameter, the capacitance C is the only one that also depends on the sample's properties. As a first approximation this value can be estimated by taking into account the capacitance formed in the air gap between the probe's tip and the sample in series with a capacitance that considers the sample's dielectric function and penetration depth for THz radiation [81]. Therefore, in THz-ANSOM experiments the signal contrast originates from a change in the effective capacitance that leads to a change in the ratio between dissipated and incident power $\eta(\omega)$, Fig. 3.9.

From Eq. 3.4.7, it can be derived that $\eta(\omega)$ has a resonance at $f_r = \frac{1}{2\pi}\sqrt{\frac{1}{LC}}$. Thus, the main effect of a change in the effective capacitance of the antenna system is a spectral shift of $\eta(\omega)$. In Fig. 3.10, $\eta(\omega)$ is plotted for the aforementioned antenna parameters (R=1000 Ω and L=0.3 nH) and for three typical capacitance values together with a reference spectrum of the incoming THz radiation.

The antenna model can successfully account for the increase in the reflected THz signal measured when the distance between the probe's tip and the sample is reduced [89]. As the air gap decreases, the capacitance of the tip-sample system increases. This leads to a shift of the resonance frequency f_r towards lower frequencies, Fig. 3.10. The THz signal measured in reflection

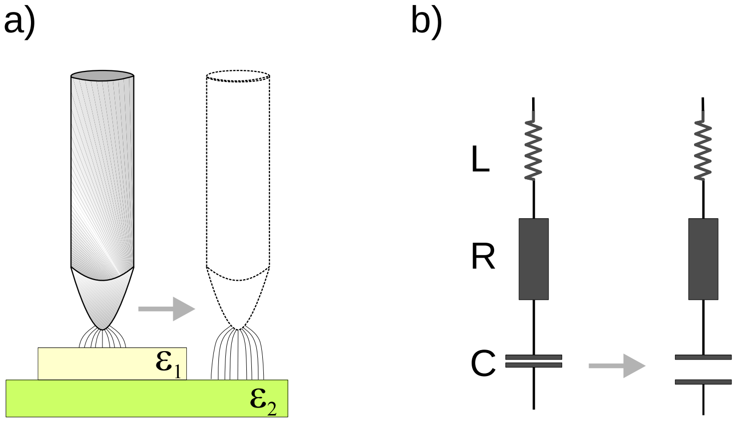

Figure 3.9: Signal contrast in THz-ANSOM experiments: a) As the tip scans samples with different complex dielectric functions ϵ_1 and ϵ_2, the antenna capacitance is modified. b) Change in capacitance shown in the equivalent electric circuit.

geometry is related to the reflected power P_{ref}

$$P_{ref} = P_{inc} - P_{diss}. \tag{3.4.8}$$

For low frequencies (i.e. ≤ 0.5 THz) there is little overlap between the dissipation ratio $\eta(\omega)$ and the incoming (reference) THz radiation, yielding a smaller amount of dissipated power which results in the increase of the THz reflected signal.

In the previous sections, it was pointed out that one of the main advantages of working with THz radiation is the fact that the electric field can be directly time resolved. Thus, a relationship between the electric field and the dissipation ratio $\eta(\omega)$ has to be developed. In this work the aproach introduced by Kersting *et al* [81] (Fig. 3.6b)) is going to be followed and therefore the measured signal is the electric field of the reflected THz radiation, $\mathcal{E}_{ref}$. The dissipation ratio can be written in terms of the electric field of the incident and dissipated radiation, $\mathcal{E}_{inc}$ and $\mathcal{E}_{diss}$

$$\eta(\omega) = \frac{P_{diss}}{P_{inc}} = \left(\frac{\mathcal{E}_{diss}}{\mathcal{E}_{inc}}\right)^2. \tag{3.4.9}$$

Combining the last two equations leads to

$$\eta(\omega) = 1 - \left(\frac{\mathcal{E}_{ref}}{\mathcal{E}_{inc}}\right)^2. \tag{3.4.10}$$

Derivating this last expression for η with respect to $\mathcal{E}_{ref}$

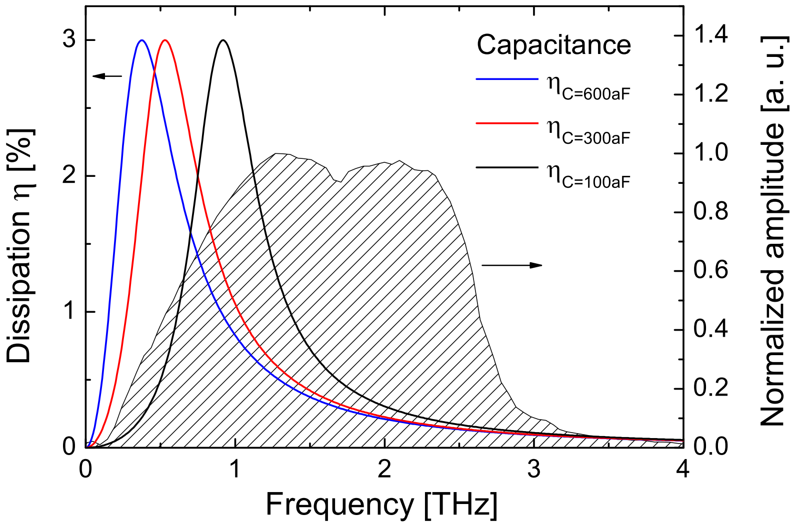

Figure 3.10: Dissipation ratio η for R=1000 Ω, L=0.3 nH and three typical capacitance values. The shaded curve shows a reference spectrum of the incoming THz radiation

$$\frac{\partial\eta(\omega)}{\partial\mathcal{E}_{ref}} = -2\frac{\mathcal{E}_{ref}}{\mathcal{E}_{inc}^2}. \tag{3.4.11}$$

Since in the current experiments $\eta(\omega) << 1$, replacing the differential with Δ, the last expression can be simplified

$$\frac{\Delta\eta(\omega)}{2} \approx -\frac{\Delta\mathcal{E}_{ref}}{\mathcal{E}_{ref}}. \tag{3.4.12}$$

So that finally the antenna model provides a way of relating the signal contrast in this type of THz-ANSOM experiments, namely the difference in the measured reflected THz electric field, to a change in the dissipation factor and therefore to the dielectric properties of the sample.

Coupling between THz radiation and the probe antenna

Antennas are known to have a high directional pattern for emitting and absorbing radiation [91]. Since the probe-sample system can be considered to be an antenna, a deep understanding of the coupling mechanism between THz radiation and the effective antenna is of utmost relevance for the design of more efficient THz near field microscopes. These mechanisms have been studied by Walther *et al* [92]. They found an expression for the electric field emission (and therefore also the absorption according to the reciprocity principle) pattern for a travelling wave antenna

$$\mathcal{E}(\alpha) \approx \frac{\sin\alpha}{1-\cos\alpha}\sin\left(\frac{\pi l}{\lambda}(1-\cos\alpha)\right), \tag{3.4.13}$$

with $\mathcal{E}$ the electric field, α the angle between the emitted (absorbed) THz radiation and the antenna axis, l the illuminated length of the antenna and λ the wavelength of the THz radiation. In Fig. 3.11 the emission pattern is plotted for two different frequencies 1 and 1.5 THz and for a typical illuminated antenna length used in this work, $l = 0.5$ mm. As mentioned before, these results can be considered for the design of the THz near field microscope. For the centre frequency of the THz radiation used in this work, around 1.5 THz, a more efficient coupling can be achieved by choosing angles between $30° - 40°$.

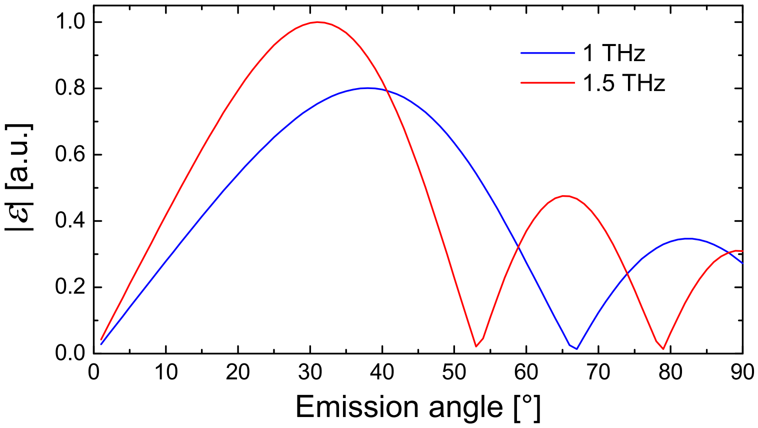

Figure 3.11: Emission pattern for an antenna of illuminated length $l = 0.5mm$ and two different frequencies, 1 and 1.5 THz.

4 Development of a Terahertz Near Field Microscope

This chapter deals with the development and characterization of the different components of a THz near field microscope. In particular a novel THz emitter is presented and its impact on the improvement of the signal to noise ratio is addressed. Later, a method for avoiding artifacts arising from the topography of samples based on shear force control is included.

4.1 Experimental Setup

In the context of this work substantial improvements to the experimental methodology were made. Thus, some experimental aspects will be discussed in detail. The setup employed was specially designed and developed for studying THz intersubband transitions in parabolic quantum wells using ANSOM techniques. Since THz frequencies are related to a temperature smaller than room temperature (for example 100 K at around 2 THz), in order to avoid thermal excitation these experiments need to be performed at cryogenic temperatures. Lowering the working temperature also reduces the electron scattering mechanisms [5]. Although in the last decade different THz-ANSOM techniques were developed [61, 78–81], to date, the microscope introduced in this work is the only one capable of operating inside a cryostat at helium temperatures (4 K). Placing a microscope in a cryostat and developing a position control system for the probe at low temperatures involve several challenges which will be discussed in a forthcoming section.
Another improvement of this setup, as compared to existing THz-ANSOMs, lies on the inclusion of a more powerful novel THz broadband emitter. This allows for reducing significantly the measuring time, a particularly relevant parameter for low temperature experiments in which the measuring time is limited by the amount of helium that can be stored. In addition, these novel THz emitters enable new experiments that were previously hindered by the low signal to noise ratio. The design and construction of the novel THz emitter will be also included on a separate section.
Finally, the work of Walther *et al* [92] introduced in the last section, has been followed so that an angle of 30° between the THz radiation and the probe axis was chosen. This lead to a factor of 5 improvemement of the coupling between the THz radiation and the antenna system as compared to previous experiments (in which an angle of 60° was employed) [93] and therefore also to a reduction of the measuring time.

The developed setup is likewise capable of performing THz far-field spectroscopy measurements in reflection as well as transmission geometry. This enables the comparison between near and far-field results, for example the momentum relaxation time of charge carriers in ultrathin layers was determined as a function of the temperature [94].

Description of the components of the setup

In Fig. 4.1 a sketch of the THz-ANSOM setup built for this work is included, it mainly comprises a THz pump-probe setup (Sec. 3.3) together with a near-field microscope, Fig. 3.6b). A mode-locked Ti:saphire laser (MaiTai, Spectra-Physics) delivers horizontally polarized 65 fs (FWHM) pulses at a centre wavelength of 780 nm and a repetition rate of 80 MHz. The laser's average power is 0.8 W so that the energy per pulse is around 10 nJ. The laser beam is divided with a beam splitter into a probe and a pump beam. The pump beam (710 mW) is used for THz generation while the probe beam (80mW) is used for THz detection.
The pump beam is focused onto the THz emitter so that a spotsize of approximately 500 μm is reached, this results in a photoexcitation density of $n_{exc} \approx 2\,\mathrm{x}\,10^{17}\mathrm{cm}^{-3}$. THz generation occurs in a biased emitter [95, 96] and is collected in reflection geometry by the first parabolic mirror (NA=0.32). Together with the THz radiation, some of the incoming laser radiation will also be reflected-diffracted at the THz emitter and collected by the parabolic mirror. This red beam will follow a similar path as the THz radiation and can therefore be used for alignment purposes or filtered when performing experiments. This is an advantage of working in reflection geometry.

The THz beam is later focused by the second parabolic mirror (NA=0.24), onto the sample in the cryostat Fig. 4.2. The cryostat (CryoVac, Konti Microskop) was custom designed to host the microscope. The spotsize on the sample depends on the wavelength of the radiation and it is found to be 1.5 mm for the centre frequency of the employed THz radiation, 1.5 THz. In the centre of the focus the probe is placed. Proper alignment between probe and focus is reached by means of slip-stick piezo actuators (ANPx51, attocube systems), Px and Py in Fig. 4.2. The same mechanism is used to approach the probe to the sample, Pz (ANPz101, attocube systems). These type of actuators have the advantage of having a long range of 3 mm, even at cryogenic temperatures. The probe is glued to a tuning fork, which is excited by a dither piezo. The distance between the probe and the sample is adjusted in close contact, using the piezo actuator Sz (ANSz50, attocube systems) further details will be included in a following section. All the microscope head (probe and actuators) is fastened to a copper holder connected to the helium cooling circuit. In this way temperature gradients are minimized. In order to perform scans without changing the alignment between probe and THz focus, the sample is placed on two piezo actuators, Sx and Sy (ANSxy100, attocube systems) with a range of 40x40 μm.

Once reflected on the sample, the THz radiation meets the probe pulse on an Indium-Tin-Oxide

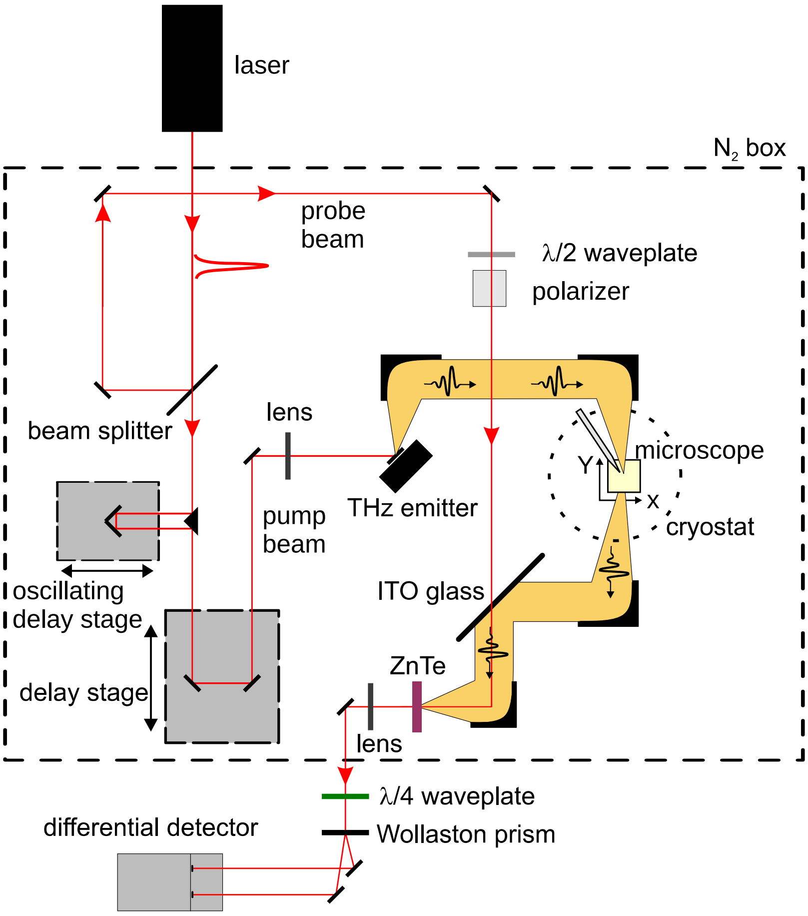

Figure 4.1: Sketch of the developed THz-ANSOM setup.

(ITO) glass. This material is transparent for radiation in the visible range but is able to reflect radiation at THz frequencies [97]. As discussed before, in pump-probe experiments both optical paths need to have the same length. The optical length of the pump beam is adjusted using a delay stage with a range of 2.54 mm and 3 μm resolution. After a time overlap between both beam paths is found, the THz pulse can be scanned by means of an oscillating delay stage (APE) which consists of a set of mirrors that can oscillate at frequencies around 15 Hz and an amplitude of 7.5 mm (corresponding to a delay of 50 ps).

The electric field of the THz radiation is retrieved with electro-optic sampling techniques (Sec. 3.3.2). The last parabolic mirror focuses the near infrared probe pulse together with the THz beam onto a 1 mm thick ZnTe crystal with [110] orientation. As introduced before, the probe beam then goes through a $\lambda/4$ waveplate to balance the polarization. Later the two polarization components are separated using a Wollaston prism and focused onto two photodiodes (Siemens

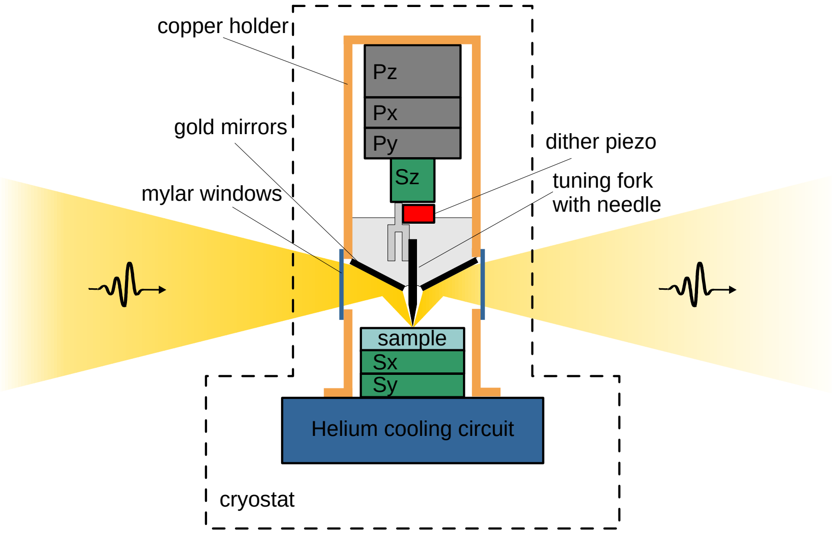

Figure 4.2: Detail of the cryostat containing the microscope.

BPW34) connected in a differential manner. Typical currents on single photodiodes are of the order of 2.5 mA, while the THz incoming beam induces a birefringence in the ZnTe crystal which leads to a difference in the current measured between the photodiodes as high as 20 μA. Finally, in order to avoid THz absorption due to water vapor around 0.8, 1.6 and 2.1 THz [98], the whole setup is placed within a plexiglass box that can be flooded with nitrogen gas.

4.2 Development of a Novel THz Emitter

4.2.1 Introduction

In order to design an experiment, one of the main parameters that determines the measuring time is the signal to noise ratio. This is particularly relevant for THz-ANSOM experiments in which the coupling between THz radiation and the antenna system is of the order of 3%. In the case of low temperature measurements, the acquisition time is further restricted to the amount of helium that can be stored. In current technology, the detection sensitivity for THz radiation is mostly limited by shot noise [99]. Therefore an increment of the signal to noise ratio can only be attained provided the THz output power is improved.

Following Sec. 3.2.2, the THz emission of photoconductive switches can be increased by applying higher electric fields, Eq. 3.2.7. One approach consists in increasing the bias voltage, however one disadvantage is that very high voltages up to 400 V are required [100]. The other option is to use rather low bias voltages (<50 V) but to reduce the gap between the contacts without affecting the active surface. This can be achieved using metal-semiconductor-metal (MSM) photoconductors with interdigitated finger electrodes, Fig. 4.3a). This type of structures can be built with an electrode spacing smaller than 10 μm.

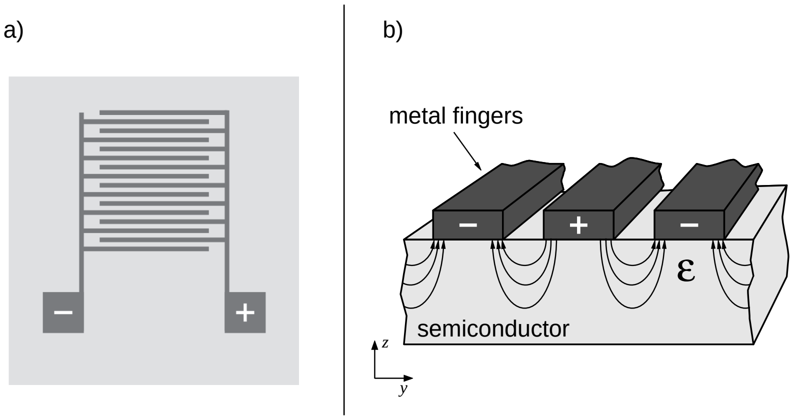

Figure 4.3: a) Sketch of a metal-semiconductor-metal (MSM) photoconductor with interdigitated finger electrodes. b) The alternating applied bias results in an electric field $\mathcal{E}$ in the semiconductor as indicated by the arrows.

The applied bias voltage results in a electric field with alternating direction between the fingers, Fig. 4.3b). Therefore, photogenerated carriers are accelerated into opposite directions. This leads to THz electric fields in counter-phase between consecutive finger spacings and thus to destructive interference and a cancellation of the THz emission in the far-field. Despite the destructive interference, surprisingly THz emission into the far field can be observed. This effect was studied in the present work [101] in order to maximize the emission output of photoconductive emitters. A weak THz emission was observed in this configuration. It was found that this emission is due to the unidirectional acceleration of carriers towards the semiconductor surface. The carrier's velocity in z is given by Eq. 2.1.5, $v_{dz} = \mathcal{E}_z(z,y)\mu_{e,h}$ as a consequence, for example, the electron velocities near an anode or cathode have opposing directions with a magnitude proportional to the local electric field $\mathcal{E}_z(z,y)$. However, the acceleration vector point in the same direction. In the vicinity of the anode, electrons experience an overall acceleration because the external field increases during their motion. The reverse happens near the cathode: The driving force reduces because the electrons move out of the high-field region. Since the electromagnetic emission is proportional to the carrier acceleration, the individual emission processes have the same polarity, which leads to a constructive superposition and thus, to a nonzero THz far-field emission.

One way of avoiding the destructive interference in the far-field due to counter-phase THz generation is to passivate every second finger spacing, Fig. 4.4a). The applied electric field in y direction is more intense on those finger spacings that were not passivated 4.4b) and therefore photogenerated carriers are predominantly accelerated into one direction leading to constructive interference of the generated THz radiation in the far field.

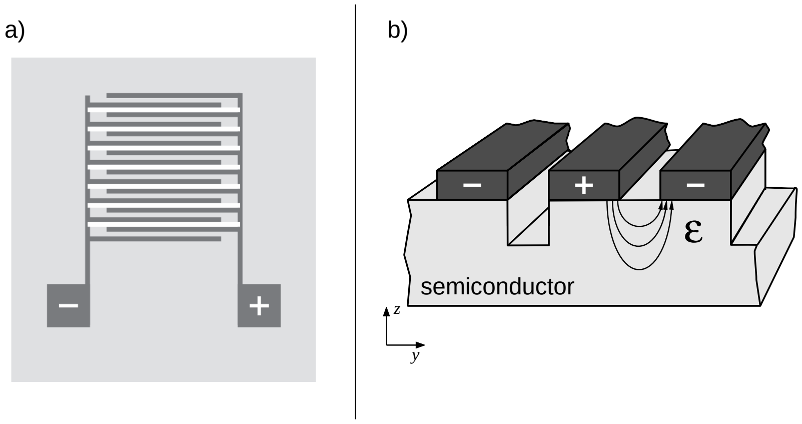

Figure 4.4: a) Sketch of a metal-semiconductor-metal (MSM) photoconductor in which every second finger spacing has been passivated. b) The applied electric field in y direction, $\mathcal{E}_y$ is more intense on those finger spacings that were not passivated.

4.2.2 Fabrication

The passivation of every second finger spacing (double periodicity) was previously performed using shadow masks integrated to the THz emitter device [95, 102]. Following this approach, every second finger spacing is covered with an opaque insulating material so that carriers can not be photogenerated in that region. Unfortunately, this technique is very challenging since it requires advanced hybrid technology. An alternative, which consists in etching away every second finger spacing (Fig. 4.4) instead of blocking it, was developed in the present work. This can be done with conventional chemical etching procedures.

As discussed in Sec. 3.2.2 the interdigitated metal-semiconductor-metal structures were fabricated on semi-insulating GaAs (Freiberger). The overall photo-active area is 2x2 mm. The metallic fingers have a width and spacing of 6 μm and were evaporated in a layer sequence of 20 nm Ti, 60 nm Au and 20 nm Ti. The fingers form a Schottky contact with the GaAs. The THz emitter is completed by etching every second spacing $\approx$5 μm deep using Piranha solution (H_2SO_4+H_2O_2+H_2O) so that therefore only conventional photolithography as well as wet chemical etching techniques were employed. In Fig. 4.5a) an image of the THz emitter taken with a scanning electron microscope (SEM) is included. In order to estimate the electric field distribution between the fingers, numerical simulations were carried out. The result is depicted in Fig. 4.5b) and shows that the electric field under the trenches where the etching took place, is almost negligible and thus, following photoexcitation carriers are accelerated predominantly into one direction.

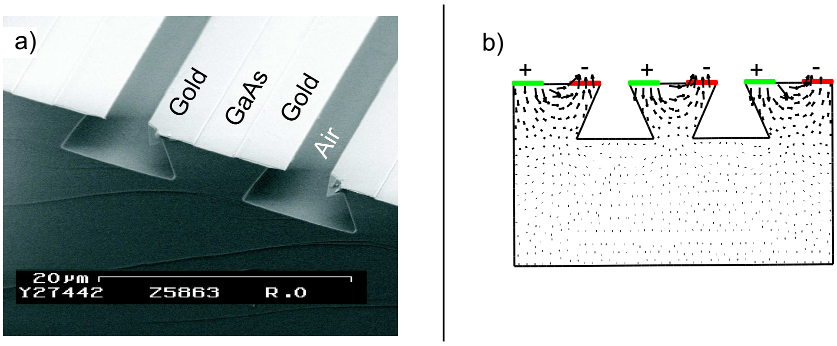

Figure 4.5: a) Scanning electron microscopy image of the THz emitter. b) Numerical simulation of the applied electric field.

4.2.3 Results on the Performance of the THz Emitter

A typical few cycle THz pulse generated with these devices is included in Fig. 4.6a). The corresponding amplitude spectrum, Fig. 4.6b) shows a centre frequency of 1.7 THz and an emission bandwidth of more than 2 octaves.

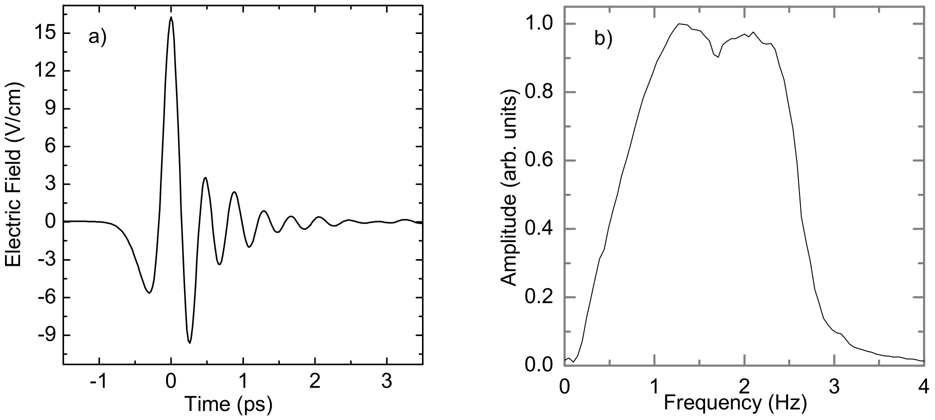

Figure 4.6: a) A typical THz pulse obtained with the developed emitter and b) corresponding amplitude spectrum.

With the aid of Eq. 3.3.1 the field strength of the THz pulses was deduced. In Fig. 4.7, the peak amplitude of the THz emission together with the photocurrent through the emitter device in dependence on the applied electric field is plotted.

The peak amplitude nearly follows a linear behavior while the current through the emitter exhibits a faster increase. This nonlinear behavior restricts the maximum DC field that can be

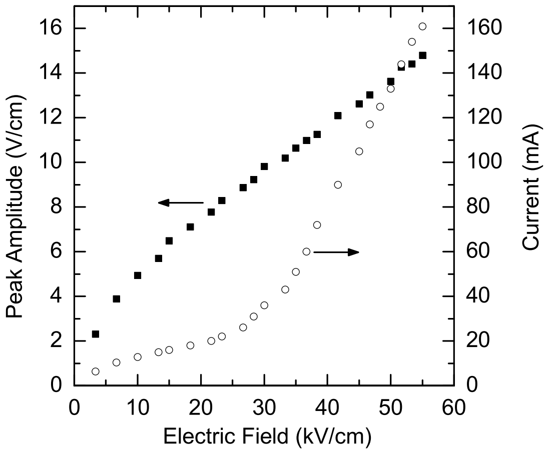

Figure 4.7: Peak amplitude of the THz emission and photocurrent through the emitter device in dependence on the applied electric field.

applied to about 50 kV/cm. Under this bias, the THz field strength is 15 V/cm, which leads to a power intensity at the THz focus I_{THz} given by

$$I_{THz} = \frac{1}{2}\epsilon_o c \mathcal{E}_{THz}^2 \approx 3\frac{kW}{m^2}. \tag{4.2.1}$$

This last expression can be integrated for the THz pulse in Fig. 4.6a) in time domain, so that an energy density $E_d \approx 1$ nJ/m^2 per pulse is estimated. For a THz focus with a radius $r = 1$ mm and considering the repetition rate of the pulse laser $v_l = 80$ MHz, the average THz power P_{THz}

$$P_{THz} = E_d \cdot v_l \cdot \pi r^2 \approx 0.25\mu W. \tag{4.2.2}$$

The performance of the developed THz emitter was compared to previously introduced THz emitters using shadow masks. Under identical excitation conditions both emitters show a similar field strength [95, 102, 103]. In addition, the field strength obtained with this device is five times bigger than the one obtained with InAs wafers which is one of the most popular THz emitters.

4.3 Analysis and Improvement to the Signal to Noise Ratio

The signal to noise ratio (SNR) is defined as

$$SNR = \frac{Signal}{sd(Signal) \cdot \sqrt{\tau_{int}}}, \tag{4.3.1}$$

where *sd*(*Signal*) is the standard deviation of the signal, which is a good estimate of the noise level, and τ_{int} is the integration time. This last equation is of utmost relevance since it allows to determine which experiments are feasible in a determined amount of time. For the present work in which THz-ANSOM experiments are performed, the *Signal* is represented by the measured THz electric field. The signal to noise ratio is a property of the whole setup comprising the THz emitter but also the detection scheme. The *Signal* has been already introduced in the last section and therefore in the following the different sources of noise will be discussed. The main two sources of noise that affect the THz signal are the laser noise and the Shot noise.

Laser noise

The laser noise (fluctuations in the emitted power intensity) affects the THz generation as well as the detection. In the detection, this effect can be reduced by balancing the probe laser beam intensity in each photodiode, Sec. 3.3.2. Since the photodiodes are connected in a differential manner, if both receive the same intensity, fluctuations in the probe laser beam cancel out. For the pump laser, fluctuations of the laser power can be correlated to the noise of the measured THz electric field. The frequency spectrum of the laser noise is included in Fig. 4.8, it shows a peak at around 25 kHz and also high noise components for low frequencies. The influence of the laser fluctuations to the THz generation can be decreased if a low bandwidth detection (e.g. by using a lock-in technique) is applied. This is performed by biasing the THz emitter with an alternating voltage at a frequency with a low noise level.

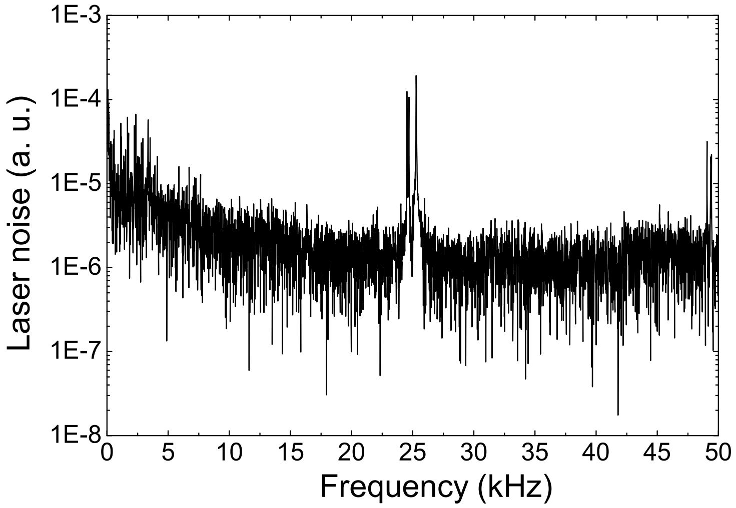

Figure 4.8: Frequency spectrum of the laser intensity fluctuations.

Shot noise

The Shot noise arises from the fact that light or electrical current are quantized in a discrete amount of photons or carriers respectively. In the photodiodes, the probe laser beam generates photocarriers. The number of measured photocarriers will fluctuate around the average value N following a Poisson distribution:

$$sd(N) = \sqrt{N}, \tag{4.3.2}$$

where $sd(N)$ is the standard deviation of the average number of carriers. The number of carriers are not directly measured but rather the electrical current they generate in a determined integration time τ_{int}. This current is given by $I = e \cdot N/\tau_{int}$, and has therefore an associated Shot noise:

$$sd(I) = \frac{e \cdot \sqrt{N}}{\tau_{int}} = \sqrt{\frac{e \cdot I}{\tau_{int}}}. \tag{4.3.3}$$

This expression sets the minimum amount of noise in THz detection using electro-optic sampling [99].

Fast scan

A further improvement for the acquisition of THz pulses in time domain consists in the introduction of an oscillating scan delay (Fig. 4.1). The previous approach was based on a set of mirrors mounted on a step motor (labelled ”delay stage” in Fig. 4.1), so that for determined time delays the THz electric field was measured and thus the field transient was reconstructed in time domain. Depending on the desired time resolution, typical values for time domain sampling are between 20 and 100 fs. Thus, the stage motor needs to shift around 3 and 15 μm between successive sample points. During this time lag no THz measurements are performed which affects the overall signal to noise ratio. In order to reduce this effect, higher integration times can be chosen so that the time lag between measurements represents only a small percentage of the total integration time. However, as studied in detail in [104], this leads to a further reduction of the signal to noise level due to the low frequency noise. These problems were solved using an oscillating scan delay for recording the THz pulses. This device has a set of mirrors that oscillate with a sine function at frequencies around 15 Hz and a maximum oscillating amplitude of 50 ps. In this way, the THz electric field is recorded at an acquisition frequency of 100 kHz (with a corresponding integration time of 10 μs) avoiding time lags and the low frequency noise. A comparison of the standard deviation of the THz signal obtained using both methods to generate time delay between pump and probe together with the THz reference pulse is included in Fig.

4.9. Both measurements, with an oscillating scan delay and with the step motor scan delay, were fixed to the same total time. It can be seen that on average, the introduction of an oscillating delay stage, yields five times less noise level and therefore a five times enhancement in the signal to noise ratio. As a final remark, the signal to noise obtained at the peak of the THz pulse is of the order of 100000 $\mathrm{Hz}^{1/2}$.

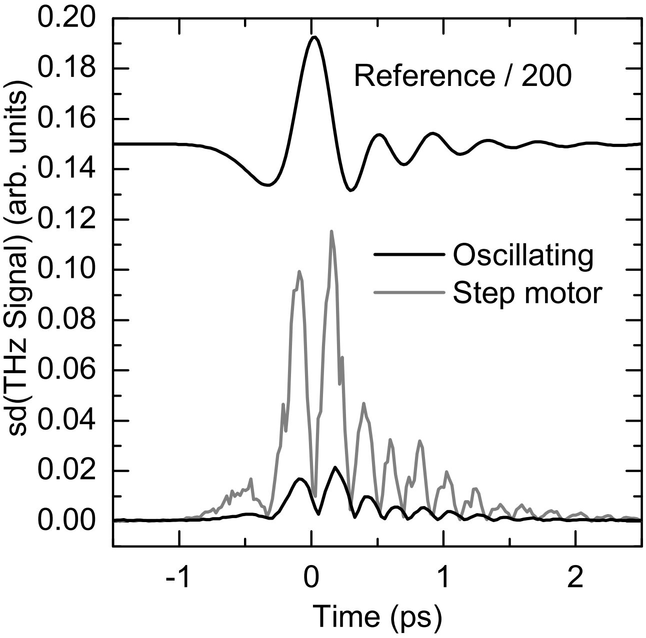

Figure 4.9: Comparison between the standard deviation of the THz electric field obtained using an oscillating delay stage and a step motor delay stage. In the upper part of the figure, the measured THz pulse is included as a reference.

4.4 Development of a Shear Force Control System for THz-ANSOM Techniques

4.4.1 Introduction

As discussed in Sec. 3.4.2 aperture-less near field techniques that overcome the diffraction limit take advantage of the evanescent waves between probe and sample. It is therefore necessary for THz-ANSOM techniques to place the probe tip at a distance from the sample smaller than the wavelength of the THz radiation employed. In addition, it is empirically found that for submicrometer resolutions, the tip-sample distance has to be smaller than 100 nm [89]. Besides that, it was observed that the image contrast decreases significantly with the tip-sample separation [81]. Reducing the tip-sample distance without degrading neither the sample nor the tip makes THz-ANSOM experimentally challenging. If samples are scanned with the tip held at larger heights than the topographic roughness of the sample, the aforementioned problems can be avoided. However, this leads to an ambiguity in the interpretation of the THz signal contrast. This signal contrast can originate from variations in the dielectric properties of the sample or from the topographic profile $\Delta z(x,y)$ which affects the air gap between tip and sample (see Fig. 3.9). Thus, in order to reduce artifacts arising from the sample topography, it is important to keep the distance between sample and tip constant, ideally in the nanometer range.

Scanning tunnelling microscopy (STM) could be a candidate for controlling the tip-sample distance. However, since this method relies on measuring a tunnelling current between tip and sample only conductive samples can be studied. Alternatively, a well established technique, atomic force microscopy (AFM) could be employed. Unfortunately THz microscopy requires probes in the millimeter range for effective antenna coupling, much larger than standard AFM cantilevers. These limitations were circumvented in this work [105] by adapting shear force microscopy (SFM) [106–108] to THz-ANSOM. SFM techniques are based on the detection of the shear force between tip and sample F_{ts}. These forces are mostly short-range, like the van-der-Waals force, that builds up when the tip-sample distance is reduced below 100 nm. By measuring and monitoring F_{ts} the tip-sample distance can be controlled. Moreover, SFM allows for simultaneous topography measurement which enables the recognition of sample features.

4.4.2 Overview and Realization of a Shear Force Control Technique

For the present work, tungsten probes were used due to their stiffness and high electric conductivity at THz frequencies. The probes were chemically etched with a solution of NaOH until tips with a diameter between 100 nm and 1 μm were obtained. In Fig. 4.10 scanning electron microscope images of a tungsten probe with an etched tip are included, the zoom on the right shows a diameter of around 100 nm.

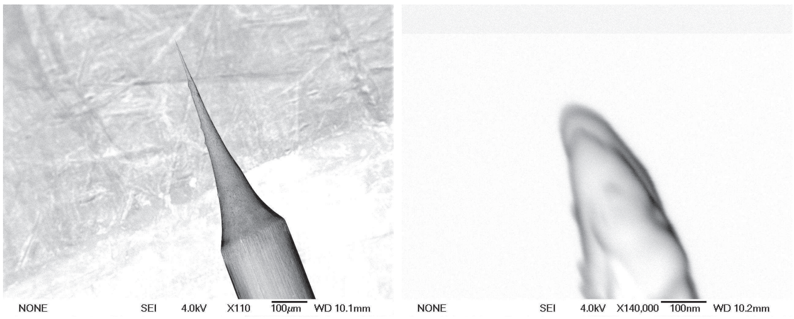

Figure 4.10: Scanning electron microscope images of a tungsten probe with an etched tip. On the right a zoom of the tip is included.

Following chemical etching, the probes were glued onto one arm of commercial quartz tuning forks protruding some millimeters, see Fig. 4.11a). This tuning forks have originally a resonance at 2^{15} Hz=32768 Hz, however when the probe is glued to it, the resonance is shifted to lower frequencies. In Fig. 4.11b) the frequency dependence of the tuning fork's oscillating amplitude with an attached needle is depicted. It can be noted that the resonance occurs at around 26 kHz with a quality factor of Q=900.

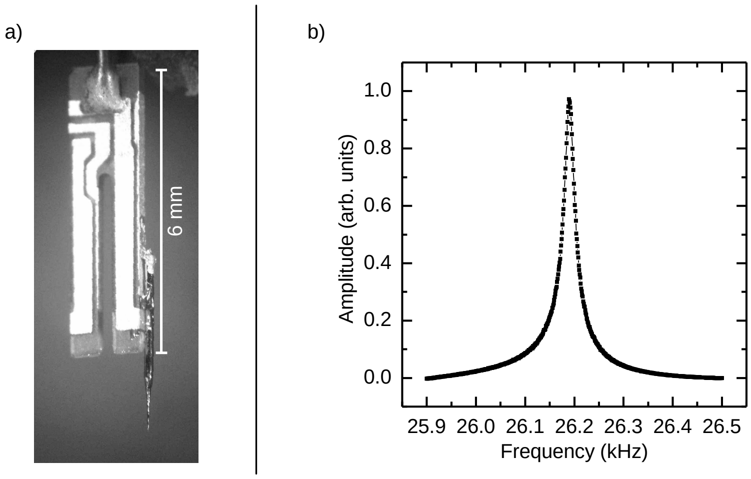

Figure 4.11: a) Image of a tungsten probe glued to a commercial quartz tuning fork used for shear force detection. b) Frequency dependence of the tuning fork oscillating amplitude with glued needle. A resonance frequency of around 26 kHz and a quality factor of Q=900 is obtained.

The amplitude of the tuning fork's oscillation is measured to extract the shear force between tip and sample. A sketch of the SFM setup including electronic connections and devices is included in Fig.4.12. The slip-stick piezo actuators Px, Py and Pz are used to align the probe tip to the THz beam focus and to bring the probe close to the sample.

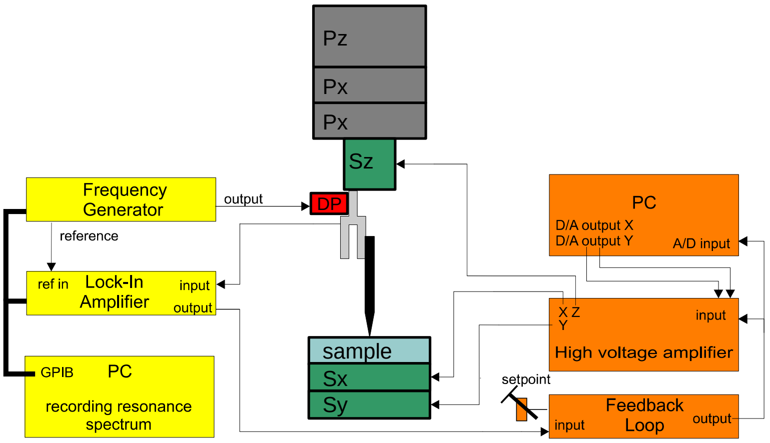

Figure 4.12: Sketch of the shear force microscopy (SFM) setup.

The tuning fork is excited at its resonance frequency, with a frequency generator (DS360, Stanford Research Systems), which drives a dither piezo (DP) attached to the tuning fork. The physical displacement induced to the tuning fork arms was previously measured using a Michelson interferometer [88] and found to be <1 nm for typical driving voltages. The oscillation of the tuning fork induces a voltage due to the piezo electric properties of quartz, which is measured with a lock-in amplifier (SR830, Stanford Research Systems) at the driving resonance frequency. When the probe is approached to the sample's surface, the oscillation amplitude of the tuning fork is reduced once the tip-surface separation is less than approximately 50 nm due to shear forces, see Fig. 4.13.

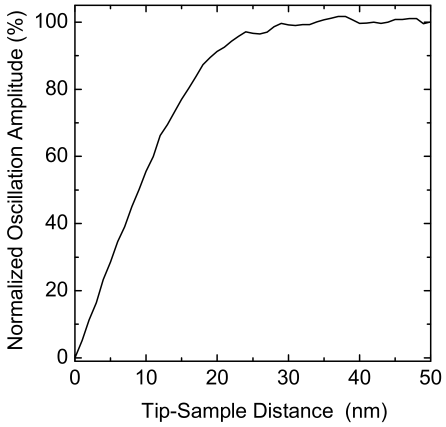

Figure 4.13: Dependence of the tuning fork's oscillation amplitude with the tip-sample distance.

In this example, if the tip-sample distance is to be held constant at for example 20 nm, the amplitude of the tuning fork has to be kept at around 80 % of the free oscillation amplitude. This percentage of the free oscillation amplitude constitutes the working setpoint. The measured amplitude signal of the tuning fork and the desired setpoint are fed into a feedback controller which operates following a proportional-integral (PI) algorithm, developed and implemented during the present work (further details are included in Appendix A). The feedback controller outputs a voltage that is related to the difference between the input amplitude signal and the user defined working setpoint. This voltage is amplified (ANC300, attocube systems) leading to an expansion or contraction of the Sz piezo actuator. In this way, the tip-sample distance is kept constant. By simultaneously recording the voltage put out to Sz while scanning the sample with the Sx and Sy piezo actuators, a topographic image of the sample is obtained.

Shear force between tip and sample

Following the approach introduced by Karrai [109], the shear force F_{ts} can be deduced within an harmonic oscillator model

$$F_{ts} = \left(1 - \frac{A_c}{A_o}\right) \frac{\kappa}{\sqrt{3}Q} x_o, \tag{4.4.1}$$

with A_c/A_o the ratio (working setpoint) between the tuning fork amplitude with the needle in contact A_c and the free oscillation amplitude A_o. The shear force is also a function of Q the quality factor of the tuning fork resonance, the spring constant of the quartz fork $\kappa \approx 26.6$ kN/m and the free oscillating amplitude at the resonance frequency $x_o < 1$ nm. The shear force can cause degradation of the tip as well as of the sample and thus it should be kept at the minimum value possible. The shear force can be reduced by improving the quality factor and working with lower oscillation amplitudes x_o.

4.4.3 Characterization and Spatial Resolution of the Microcospe

Approach of the tip to the sample

The approach routine was optimized and studied in detail since it provides insight into whether the probe was crashed. In Fig. 4.14 the tuning fork amplitude variation during a tip-sample approach is plotted, the data included were taken with an acquisition frequency of 1 kHz. Initially, the PI feedback-loop controller is not in operation and therefore the quartz fork oscillates with its free amplitude. At $t \approx 5$ s the working setpoint is adjusted to 79 % and thus the PI feedback-loop controller starts adjusting the tip-sample distance. After 100 ms the tuning fork amplitude oscillates around the selected setpoint with a standard deviation of 2 %, this can be translated into a tip-sample distance of (19±0.6) nm. It is worth noting that within the time resolution given by the acquisition frequency, the tuning fork amplitude is never reduced further than 70 % which means that the probe is not crashed into the sample. This observation has been confirmed by scanning electron microscopy (SEM) images of the probes taken after the experiment.

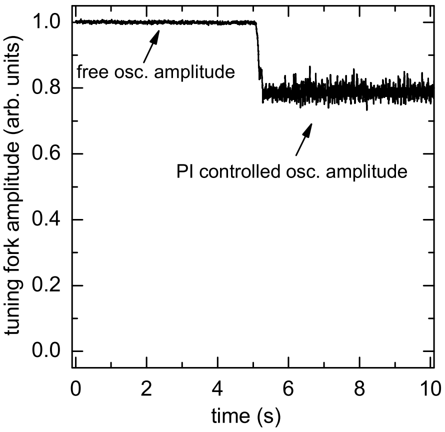

Figure 4.14: Tuning fork amplitude variations during a tip-sample approach. Before time $t \approx 5$ s, the PI feedback-loop controller is not in operation and the fork oscillates with the free amplitude. After $t \approx 5$ s the working setpoint is adjusted to 79 % and the PI feedback-loop controller keeps the tip-sample distance constant.

Scanning capabilities

The scanning capabilities of the developed shear force microscope (SFM) were tested studying GaAs nanowires [110]. In Fig. 4.15a) a scanning electron microscope image of a nanowire is included. These nanowires show a diameter of approximately 150 nm and a length of several micrometers. A sample consisting of several nanowires on a gold surface, was scanned using SFM techniques. While raster scanning the sample, the voltage required for keeping the tip-sample distance equal to 20 nm was recorded. In this way, a 20 μm x 40 μm topographic image of the surface was reconstructed. The results are shown in Fig. 4.15 b). Besides some particles (presumably GaAs fragments of broken wires), several nanowires can be detected. The nanowires appeared to be slightly bent in some cases, this is due to the non linearity of the piezo coefficient of the scanning actuators (Sx and Sy). The spatial resolution is limited to the diameter of the tip, approximately 500 nm and therefore the nanowires appear with a larger diameter as compared to the SEM image. Two nanowires, outlined in Fig. 4.15 b), were studied in further detail, see Fig. 4.15 c). This last image shows that the developed SFM can even resolve two overlapping nanowires.

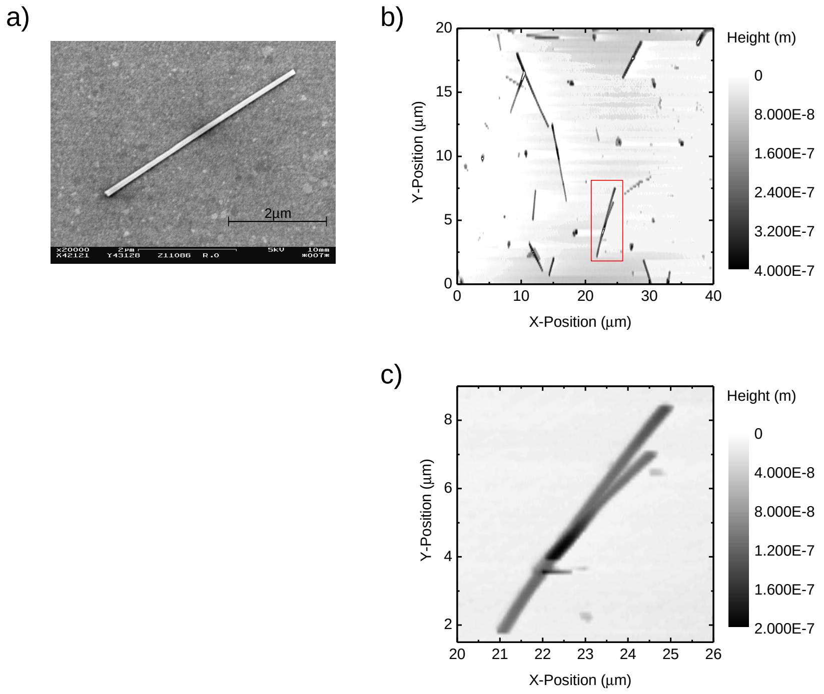

Figure 4.15: a) Scanning electron microscopy (SEM) image of a GaAs nanowire. b) Shear force microscopy (SFM) image of several GaAs nanowires lying on a gold surface. Two nanowires are outlined. c) Detail of the outlined overlapping nanowires.

Relevance of SFM for THz-ANSOM

As previously introduced, the main advantage of adapting SFM to THz-ANSOM techniques is that the tip is held in close proximity to the sample at a constant distance of around 20 nm. This results in a higher image contrast and in the elimination of artifacts arising from the topography of the sample. In addition, topographic images of the sample can be taken simultaneously and correlated to the THz-ANSOM images. Thus, the identification of features of the sample is highly facilitated and new experiments are enabled. In Fig. 4.16 a) a topographic SFM image of a GaAs nanowire is included. As in the previous image, the thickness of the nanowire is enhanced due to the tip diameter (≈500 nm) but the length and depth are within the expected values. Simultaneously, a THz-ANSOM image was also taken, see Fig. 4.16 b). The THz signal contrast of almost 2% is in good agreement with the antenna model (Section 3.4.3) and can be correlated to the topographic image.

Improvement of the spatial resolution

Near-field techniques were introduced mainly to overcome the diffraction limit and to improve the spatial resolution. This is particularly relevant for THz radiation with a wavelength of some

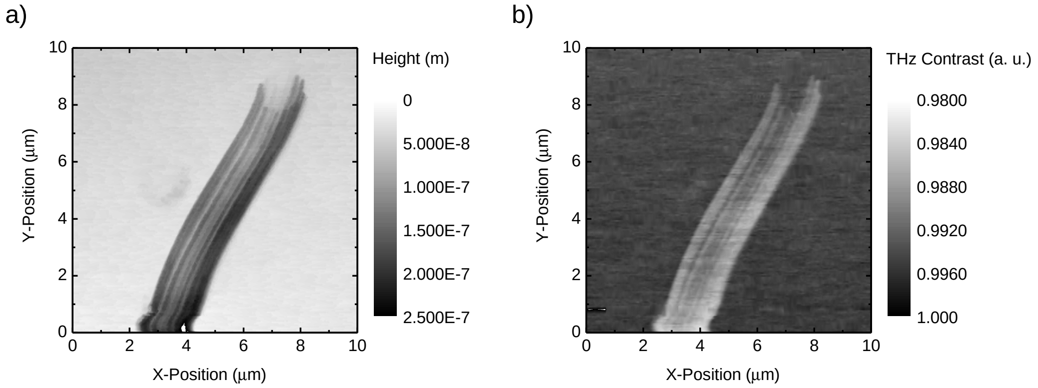

Figure 4.16: a) SFM image of GaAs nanowire. b) Simultaneously taken THz-ANSOM image.

hundreds of micrometers. Previously, Chen and coworkers [77] have reached a spatial resolution of 150 nm for broadband THz radiation at a centre frequency of 2 THz (which corresponds to a wavelength of 150 μm). However, this measurement was performed with a tip-sample distance of 200 nm without any active distance control. In addition, the signal contrast obtained was below 0.5%.

For the setup developed in the present work, the spatial resolution was tested on a sample consisting of an interdigitated finger structure of 40 nm Cr evaporated on a Si wafer. The sample was linearly scanned so that the tip went through the Cr-Si edge. During the measurement the tip-sample distance was kept at 20 nm and topographic as well as THz contrast images were simultaneously taken. The results of the line scan are shown in the following Fig. 4.17. A spatial resolution of 65 nm with a signal contrast of more than 1.5 % can be deduced. This represents an extreme sub-wavelength spatial resolution ($<\lambda/1000$) mostly limited by the tip diameter and constitutes to date the highest resolution for THz broadband radiation.

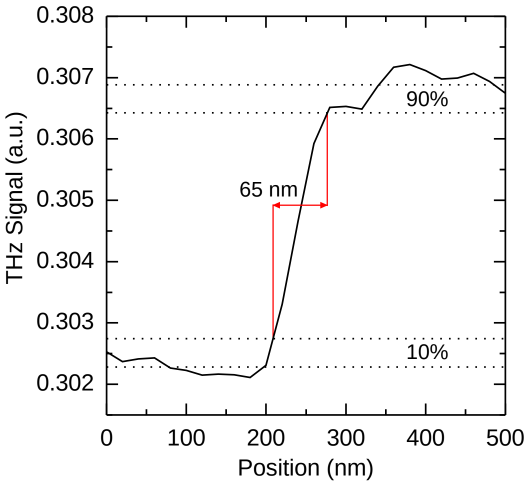

Figure 4.17: THz-ANSOM line scan of a sample consisting of an interdigitated 40 nm Cr finger structure evaporated on Si. The spatial resolution of 65 nm is outlined.

5 Preparation and Characterization of the Parabolic Quantum Well Structure

In this chapter the parabolic quantum well structure is introduced. In the first section, all the layers that constitute the structure are described. An electric characterization of the contacts made to the structure is included, together with a measurement of the electron density in the well. The chapter ends with a further characterization using numerical simulation techniques. The conduction band is simulated and the electron density in the well is deduced with a complementary method. Finally, a parameter of high relevance for the present work, the intersubband transition frequency is estimated.

5.1 The Parabolic Quantum Well

The parabolic quantum well structure studied in this work was developed in the group of Prof. Strasser at the Technical University of Vienna (TU Wien). It consists of several semiconductor layers grown on an intrinsic gallium arsenide (i-GaAs) wafer using molecular-beam epitaxy (MBE) techniques. The layer sequence, composition, thickness, doping concentration and aluminum content x is included in Table 5.1.

The structure begins with an i-GaAs 100 nm buffer (l) deposited on the i-GaAs wafer (m). The following layer (k) consists of 50 repetitions of a sequence of 1.4 nm GaAs and 0.6 nm AlAs and serves as a barrier to stop diffusion of impurities from the wafer [34]. The 200 nm $Al_{0.3}Ga_{0.7}As$ layer (j) has the conduction band at a higher energy level than the next layers and therefore it confines electrons to the well. The doping of the well is performed using modulation doping techniques as discussed in Sec. 2.2.2, through layers (i), (h), (f) and (e) surrounding the well (g). Layers (i) and (e) are made of 18 repetitions of a sequence of 2 nm $Al_{0.3}Ga_{0.7}As$ and 1 nm $Si{:}Al_{0.3}Ga_{0.7}As$. The doping is done with silicon, which acts as a donor (n-doping), at a 1.8 x $10^{12}cm^{-2}$ surface density. Electrons diffuse into the well and are separated from the donors through layers (h) and (f), 15 nm of $Al_{0.3}Ga_{0.7}As$. This leads to an increment of the mobility of the electrons in the well, see Fig. 2.5 c), also these layers ensure that the electrons transferred into the well are insufficient to begin occupying the second subband at low temparatures [28]. The parabolic quantum well is located in layer (g) and has a thickness of 140 nm. The aluminum content is varied from $x = 0.2$ at the edges to $x = 0$ at the centre in a parabolic manner using digital alloy techniques, Sec. 2.2.3 and Fig. 2.6. Subsequent layers (d), (c) and (b) of $Al_{0.3}Ga_{0.7}As$, with an overall thickness of 111 nm and a volume silicon doping in (c) of 1 x $10^{18}cm^{-3}$ straighten

Layer	Material	Doping Level	Thickness (nm)	x(%)
a	GaAs		5	
b	$Al_xGa_{1-x}As$		80	30
c	Si:$Al_xGa_{1-x}As$	1 x $10^{18}cm^{-3}$	11	30
d	$Al_xGa_{1-x}As$		20	30
e	18 x (2 nm $Al_xGa_{1-x}As$/1 nm Si:$Al_xGa_{1-x}As$)	1.8 x $10^{12}cm^{-2}$	54	30
f	$Al_xGa_{1-x}As$		15	30
g	$Al_xGa_{1-x}As$ (QW, x parabolic)		140	0/30
h	$Al_xGa_{1-x}As$		15	30
i	18 x (2 nm $Al_xGa_{1-x}As$/1 nm Si:$Al_xGa_{1-x}As$)	1.8 x $10^{12}cm^{-2}$	54	30
j	$Al_xGa_{1-x}As$		200	30
k	50 x (1.4 nm GaAs/0.6 nm AlAs)		100	100/30
l	GaAs (Buffer)		100	
m	i-GaAs (Substrate)		(508±20) μm	

Table 5.1: Layer sequence of the parabolic quantum well used in this work, from top (surface) to bottom (wafer). For every layer, the composition, thickness, doping concentration and aluminum content x is listed.

the conduction band [111]. The structure is completed with a 5 nm GaAs cap layer to prevent oxidation of the $Al_{0.3}Ga_{0.7}As$ and to enable contacting. The mobility of the electrons in the well at cryogenic temperatures was found to be approximately 55000 cm^2/Vs [112] by performing Hall measurements.

Contacting of the structure

As it will be discussed in more detail in the following chapter, for the present work and in order to perform differential THz measurements the parabolic quantum well has to be depleted (emptied) from electrons. This is achieved through two contacts: An Ohmic contact (Sec. 2.4.2) to the 2 DEG in the quantum well and a Schottky (Sec. 2.4.1) contact to the surface 5.1.
The Ohmic contacts are performed using a previously developed recipe [104] consisting of 45 nm AuGe, 10 nm Ni and 220 nm Au. Following evaporation, the contacts are annealed during 5 min at 570 K in a formation-gas atmosphere. Four Ohmic contacts are deposited onto the edges of the structure, this allows for further characterization of the resistance between the contacts and the electron gas. For near-field measurements a contacted probe in close proximity (20 nm) to the GaAs cap layer acts as a Schottky contact (MIS diode) [93]. In the case of far-field measurements a 5 nm Cr layer is evaporated in the centre of the structure. In Fig. 5.1 a sketch of the contacted structure showing the parabolic quantum well layer, the Ohmic and the Schottky contacts is included.

Experimental coupling of the THz radiation to the intersubband transitions

In Sec. 2.3.2 the coupling of the electromagnetic radiation to intersubband transitions in structures with quantum wells was discussed. The main result is that in order to excite intersubband transitions the electric field of the incoming radiation needs to have electric field components

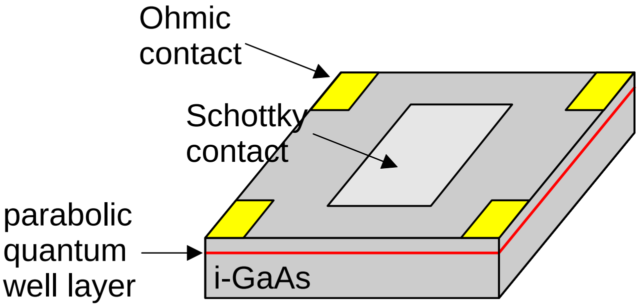

Figure 5.1: Sketch of the parabolic quantum structure. The Ohmic as well as the Schottky contacts are indicated.

in the growth direction of the structure z (perpendicular to the surface). For near-field measurements, the induced electric field between probe tip and sample satisfies this condition, (see for example Fig. 3.8 a)). However, in the case of far-field experiments the incoming radiation impinges at an angle of 30° with the normal which yields a reduced electric field in z direction. The coupling efficiency can be enhanced by introducing a metallic grating coupler with a periodicity much smaller than the wavelength of the radiation [12, 113, 114]. A sketch of a grating coupler is illustrated in Fig. 5.2. As the incoming radiation impinges at the surface with an electric field perpendicular to the surface normal, a charge distribution is induced in the metallic fingers of the grating. This distribution leads to dipole-like electric field distribution within the sample with components in z direction across the quantum well. In the present work, a grating consisting of 5 nm Cr and 50 nm Au was evaporated onto the Schottky contact. The finger width of the grating and the spacing between them is 4 μm.

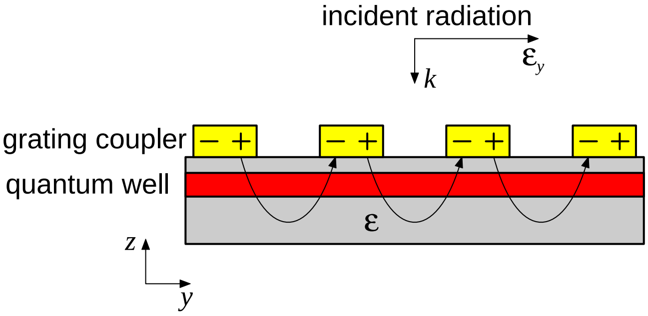

Figure 5.2: Illustration of a metallic grating coupler. The wave vector k and the electric field $\mathcal{E}_y$ of the incoming radiation are indicated. $\mathcal{E}$ represents the induced electric field within the structure .

5.2 Electronic Characterization

The Ohmic and Schottky contacts deposited on the parabolic quantum well structure enable the electric characterization through current-voltage (I-V) and capacitance-voltage (C-V) measurements. For simplicity these experiments were carried out at 80 K (nitrogen temperature) since comparable results are expected at even lower temperatures. Also, the following measurements were performed in the dark, in order to prevent photoexcitation of carriers.

I-V Measurements

Access to the electron gas in the quantum well is of high relevance to perform differential THz experiments. The Ohmic contacts to the electron gas were characterized through I-V measurements between two of this contacts. The results are shown in Fig. 5.3. As expected for Ohmic contacts, a linear dependence of the current with the voltage was obtained. The resistance between Ohmic contacts through the parabolic quantum well structure is approximately 0.8 kΩ, in good agreement with calculations considering the doping concentration and the dimensions of the sample.

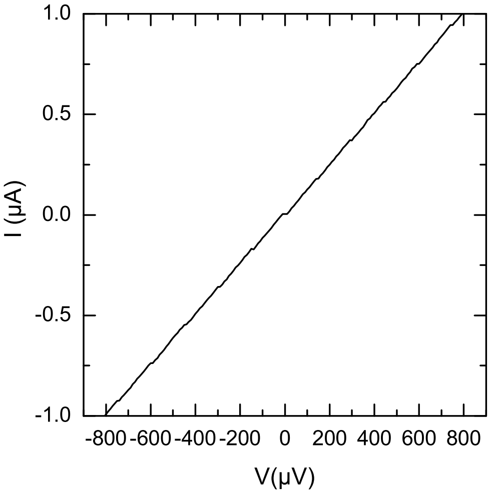

Figure 5.3: I-V measurement between two Ohmic contacts. A resistance of 0.8 kΩ can be extracted between the contacts and through the parabolic quantum well structure.

The resistance between an Ohmic and Schottky contact was characterized in the range of -0.75 to 10 V, where the sign corresponds to the voltage applied to the Ohmic contact. This range is the one to be employed in forthcoming THz experiments. These contacts show a typical diode behavior, see Fig. 5.4 with a standard forward voltage drop V_d=-0.6 V. The reverse current remains constant around 2 μA for voltages higher than 2 V. At 10 V the breakdown voltage is still not reached, setting an appropriate range for operation.

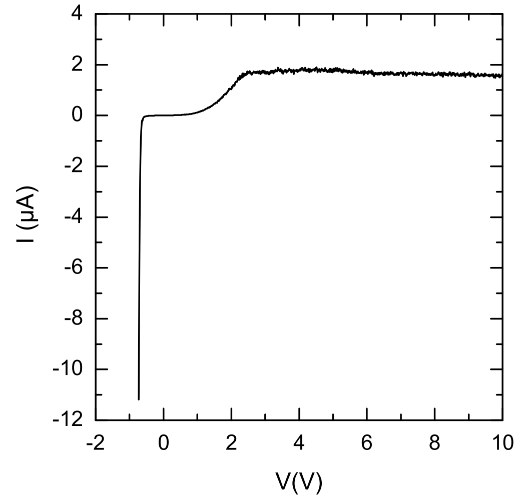

Figure 5.4: I-V measurement between an Ohmic and a Schottky contact showing a typical diode behavior. The forward voltage drop occurs at V_d=-0.6 V and the breakdown voltage in reverse direction is not reached at 10 V.

C-V Measurements

Capacitance-Voltage profiling has become a standard technique for studying the carrier distribution in semiconductors [15, 115, 116].

Theoretical Derivation

As discussed in Sec. 2.4.1, when a positive voltage V is applied between the Ohmic contact (contacted to the electron gas) and the Schottky contact on a n-doped semiconductor, electrons are pushed away from the surface into the bulk semiconductor a distance called depletion width W,

$$W = \sqrt{\frac{2\epsilon_o\epsilon(V_{bi} - V)}{qN_d}}, \tag{5.2.1}$$

with ϵ_o being the vacuum permittivity, ϵ the dielectric function of the semiconductor, V_{bi} the built-in potential, q the electron charge and N_d the donor concentration concentration. Across this depletion zone, a capacitance C is formed,

$$C = \frac{\epsilon_o \epsilon A}{W}, \tag{5.2.2}$$

where A refers to the Schottky contact surface. A differential variation of the charge in the semiconductor dQ is related to the depletion width and electron volume density n_e through

$$dQ = q n_e A \, dW. \tag{5.2.3}$$

Combining the last equations, a new expression for the capacitance related to the voltage applied can be derived

$$C \equiv \frac{dQ}{dV} = q n_e \epsilon_o \epsilon \frac{A^2}{C^2} \frac{dC}{dV}. \tag{5.2.4}$$

So that finally, the electron volume density n_e as a function of the depletion width W is obtained

$$n_e(W) = \frac{C^3}{q \epsilon_o \epsilon A^2 \frac{dC}{dV}}. \tag{5.2.5}$$

This equation shows that from capacitance-voltage measurements in Schottky contacts, the electron volume concentration can be deduced.

Method and realization

In order to perform capacitance-voltage measurements, the following voltage is applied between the Ohmic and Schottky contacts

$$V = V_{DC} + V_{AC} \sin(\omega t) \qquad \text{with} \qquad V_{AC} << V_{DC}. \tag{5.2.6}$$

The first term on the right side corresponds to the DC voltage, which is responsible for the change in the depletion width and therefore in the capacitance. The second term consists of an oscillating voltage of amplitude V_{AC} and frequency ω. This last voltage is employed to deduce the capacitance. Thus, V_{AC} is kept at the minimum value not to affect the dc voltage V_{DC}. An oscillating current I given by

$$I = I_{AC} \sin(\omega t + \phi_o) \tag{5.2.7}$$

will be induced by the AC applied voltage. Using lock-in techniques I_{ac} can be extracted. Considering the imaginary part of an impedance, the capacitance is expressed as

$$C(V_{dc}) = \frac{I_{AC}(V_{DC})}{\omega V_{AC}}. \tag{5.2.8}$$

Results

The C-V measurement was performed at a frequency of ω=2π·300 Hz and AC amplitude of V_{AC}=0.025 V, the results are shown in Fig. 5.5. It can be noted that for voltages higher than 0.7 V the quantum well is totally depleted of electrons.

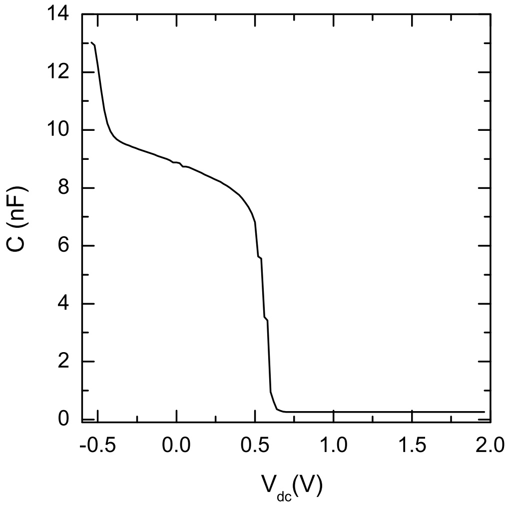

Figure 5.5: C-V measurement between an Ohmic and a Schottky contact on the parabolic quantum well structure. The experiment was done at a frequency of ω=2π·300 Hz and ac voltage amplitude of V_{ac}=0.025 V.

From the data of the C-V measurement, the electron volume density as a function of the applied voltage (Fig. 5.6) together with the electron volume density dependence with the depletion width (Fig. 5.7) can be deduced using Eq. 5.2.5. In the last figure, the electron density n_e shows a peak at $W \approx 180$ nm. This is in reasonable agreement with the centre position of the parabolic quantum well layer (g) at 255 nm (see Table 5.1). For W<125 nm, the electron volume density rapidly increases. An artifact is responsible for this behavior [117] since in that depletion range the voltage applied is close to the forward voltage drop (see Fig. 5.6) and a significant dc current is flowing („diode almost open“). In order to calculate the surface density of the two dimensional electron gas in the parabolic quantum n_{2d}^{C-V}, the curve in Fig. 5.7 can be integrated between 150 and 350 nm,

$$n_{2d}^{C-V} = \int_{150nm}^{350nm} n_e(W)dW = 3.5 \times 10^{11}\text{cm}^{-2}. \tag{5.2.9}$$

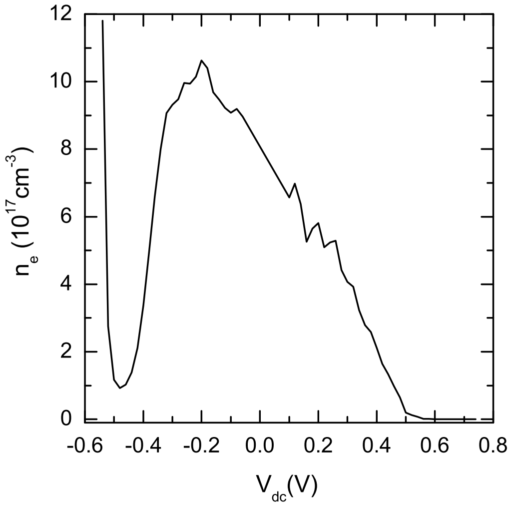

Figure 5.6: Electron volume density n_e depending on the applied voltage V for the parabolic quantum well structure. The results were deduced from a C-V measurement.

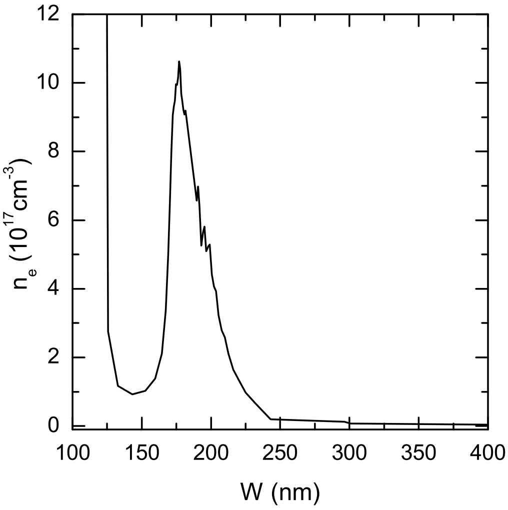

Figure 5.7: Electron volume density n_e dependence with the depletion width W for the parabolic quantum well structure. The results were deduced from the C-V measurement .

5.3 Numerical Analysis

Numerical simulation techniques are a powerful tool to study semiconductor structures with quantum wells [118]. Several properties, like the conduction and valence band, the spatial carrier distribution, the carrier wavefunctions and the quantized energy levels can be deduced.

Method

The parabolic quantum well structure studied in this work is quantized in one dimension z (see Sec. 2.3.1) and therefore the simulations can be simplified by reducing the calculations to one dimension. The software developed by G. Snider (University of Notre Dame, USA), "1D Poisson / Schrödinger solver" was employed throughout this work [119]. It solves the following equations in a self-consistent way using iterative techniques [120]. The one dimensional Schrödinger equation reads:

$$-\frac{\hbar}{2}\frac{d}{dz}\left(\frac{1}{m_{eff}(z)}\frac{d}{dz}\right)\varphi(z) + V(z)\varphi(z) = E\varphi(z), \tag{5.3.1}$$

with $\varphi(z)$ being the wave function, E the energy, $V(z)$ the potential energy and m_{eff} the effective electron mass. In one dimension the Poisson equation can be written as

$$\frac{d}{dz}\left(\epsilon_o \epsilon(z) \frac{d}{dz}\right)\phi(z) = \frac{-q(N_d(z) - n_e(z))}{\epsilon_o}, \tag{5.3.2}$$

where ϵ_o and $\epsilon(z)$ are the vacuum permittivity and dielectric function respectively, $\phi(z)$ the electrostatic potential, $N_d(z)$ the ionized donor concentration and $n_e(z)$ the electron density distribution. For a quantum well, the potential energy $V(z)$ is related to the electrostatic potential $\phi(z)$ as follows:

$$V(z) = -q\phi(z) + \Delta E_c(z), \tag{5.3.3}$$

with ΔE_c the energy due to the conduction band offset at an heterointerface. The electron density $n_e(z)$ in Eq. 5.3.2 depends on the wave function $\varphi(z)$ in Eq. 5.3.1 through:

$$n_e(z) = \sum_{i=1}^{m} \varphi_i^*(z)\varphi_i(z)n_i, \tag{5.3.4}$$

where m is the number of bound states and n_i is the electron occupation for each state i. Finally, the electron concentration for each state is expressed by [120]

$$n_i = \frac{m_{eff}}{\pi\hbar^2}\int_{E_i}^{\infty} \frac{1}{1 + e^{(E-E_i)/k_BT}} dE, \tag{5.3.5}$$

with E_i being the energy of the i state.

The software uses an iteration procedure to obtain self-consistent solutions for Eqs. 5.3.1 and 5.3.3. A starting trial potential $V(z)$ is used to calculate the electron density distribution $n_e(z)$. Subsequent iterations will yield the final self-consistent solution for $V(z)$ and $n_e(z)$ that satisfies certain error criteria.

Results

For the simulations, the layer sequence introduced in Table 5.1 was employed. The calculations were performed at a selected temperature of 80 K so that the results could be compared with the electric characterization. The discretization of the space was done in 0.5 nm steps around the heterointerfaces and in 1 μm steps inside the substrate. All the doped layers were considered to be fully ionized, so that effects like freezing of electrons were neglected. In order to quantify the influence of the electrons and donors to the conduction band (see Fig. 2.7), simulations were carried out with and without doping.

Conduction Band

In Fig. 5.8, the results for the simulation of the conduction band E_c setting all the doping concentrations to zero are included. The different layers, as labelled in Table 5.1 (from (a) surface to (m) substrate), are outlined together with the chemical potential μ. The conduction band shows the expected dependence with the aluminum content x as discussed in Section 2.2.1. In layer (g), the conduction band has clearly a parabolic shape. When the simulation is performed with doping, as in Fig. 5.9, the presence of ionized donors and electrons deform the conduction band, see Sec. 2.3.3 and [12].

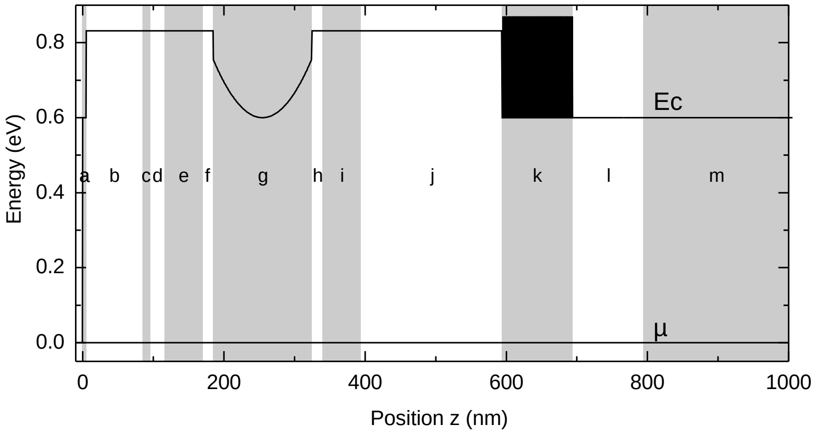

Figure 5.8: Simulation of the conduction band E_c relative to the chemical potential μ for the parabolic quantum well structure setting all the doping concentrations to zero. Together with the conduction band and chemical potential, the different layers included in table 5.1 (from (a) surface to (m) substrate) are outlined.

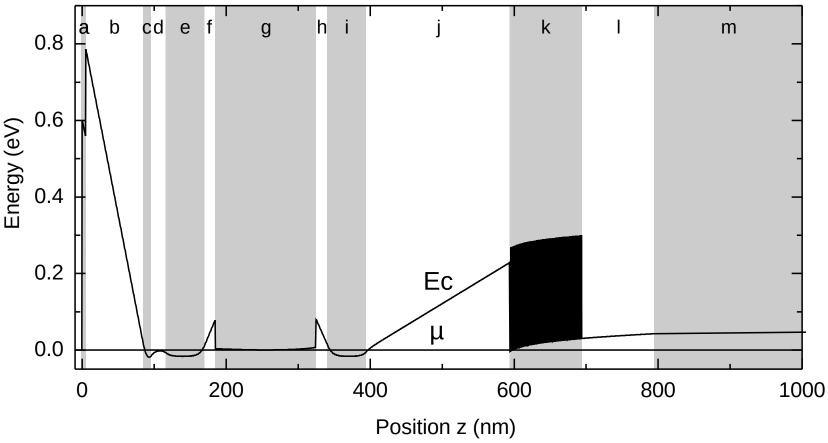

Figure 5.9: Simulation of the conduction band E_c also relative to the chemical potential μ for the parabolic quantum well structure with doping concentration. The presence of ionized donors and electrons deforms the conduction band, in particular in layer (g) were the parabolic quantum well is located.

Electron Spatial Density

The results for the simulation of the electron density dependence with the position z are shown in Fig. 5.10. A high electron concentration is observed in the doped layers (c), (e) and (i) as expected. In the parabolic quantum well layer (g), an electron concentration is also observed. This electrons are separated from the donors by layers (f) and (h), which is also expected since the modulation doping technique was employed (Sec. 2.2.2). The electron surface density of the two dimensional electron gas in the quantum well can be deduced in a similar manner as in Eq. 5.2.9, integrating the electron volume density in layer (g). Using the data from the simulation an electron surface density of $n_{2D}^{sim} = 5.9 \times 10^{11}\mathrm{cm}^{-2}$ is obtained. This result is in good agreement with the previous results extracted from the C-V measurements ($n_{2D}^{C-V} = 3.5 \times 10^{11}\mathrm{cm}^{-2}$).

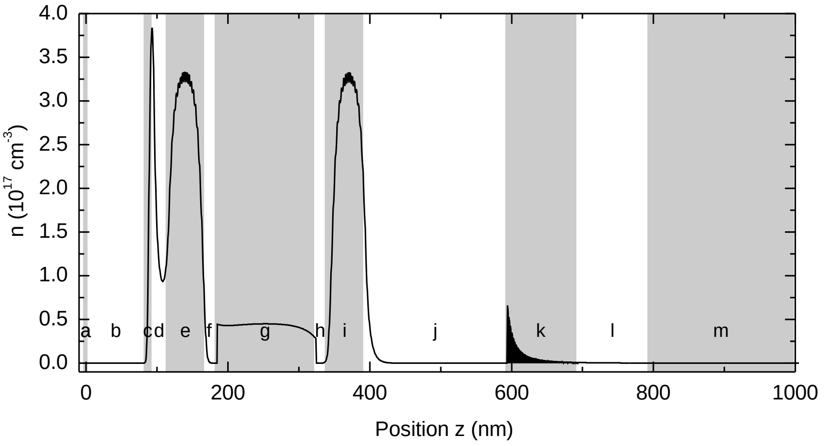

Figure 5.10: Simulation of the electron volume density dependence with the position z.

Resonance Frequency

The solution of the Poisson as well as the Schrödinger equations yield not only the band structure and the electron volume density, but also the electron wave function and quantized energy levels. As expected for an harmonic oscillator, subsequent energy levels show a constant spacing ΔE. The results for the simulated energy of the first 25 quantized states are included in Fig. 5.11 in which the solid red line consists of a linear fit. From these data, the resonance frequency was deduced to be f_0 = (2.00 ± 0.01) THz. This is an utmost relevant result for the present work, since it is the only way to estimate the expected intersubband transition frequency. In addition, the Fermi energy level was also estimated from the simulation to lay between the first and the second level. This confirms that in the present work only transitions between the first two levels are going to be excited [6].

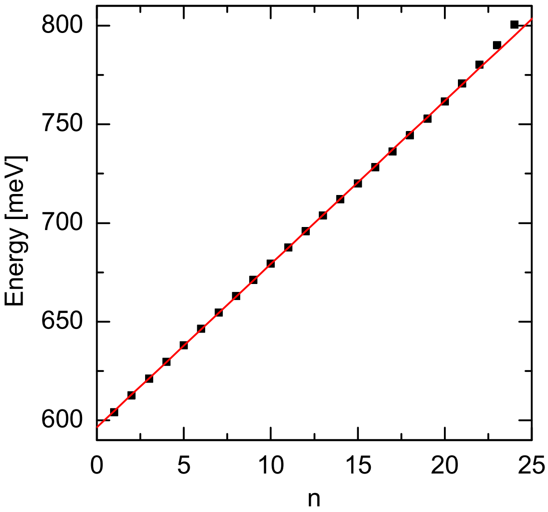

Figure 5.11: Simulated energy for the first 25 quantized states of the parabolic quantum well. A linear fit is included in red solid line.

6 Far Field and Near Field Terahertz Spectroscopy Measurements

In this chapter the results of far field and near field terahertz measurements on the parabolic quantum well structure are presented. The main scope of the experiments is discussed and the electro-modulation technique is addressed. An extension to the optical thin film equations is developed in order to analyze the measured data. Through the application of the developed model, parameters like the momentum relaxation time and dephasing time are deduced for both, the far and the near field experiments. This allows concluding on the mechanisms responsible for dephasing of intersubband excitations and to obtain for the first time quantitative information about the local dephasing time.

6.1 Introduction

Following the numerical simulations and the electrical characterization introduced in the previous chapter, THz spectroscopy measurements were performed on the parabolic quantum well sample. The main aim of these experiments is to determine the mechanisms that affect the dephasing of the intersubband transition. In Sec. 2.3.4 these mechanisms were discussed and they can be classified in two main groups: Homogeneous and inhomogeneous broadening. In the first case, scattering is mainly responsible for the dephasing while in the second case imperfections of the sample, fluctuations in the layer's thicknesses lead to a distribution of resonance frequencies that result in the broadening of the resonance. Both mechanisms are supposed to take part at the same time, however the presence of inhomogeneous broadening has not been fully understood [12] since sub-wavelength measurements are required to resolve the fluctuations in the layer. The strategy is the following: A comparison between far field measurements in which an area with a diameter of around 1 mm of the parabolic quantum well is sampled and near field measurements with a sampling area with a diameter smaller than 1 μm can provide insight into whether inhomogeneous broadening occurs. Scattering should be present in both cases and therefore homogeneous broadening but in near field measurements fluctuations of local properties are less probable. In case inhomogeneous broadening dominates, lower dephasing rates in near field experiments are expected as compared to the dephasing obtained in far field measurements. Additionally, it can be expected in this case, that the measured resonance frequency depends on the position of the near field probe.

In order to perform these experiments, the setup presented in chapter 3 was designed and built.

To date, the results presented in this chapter belong to the first THz near field measurements performed at low temperatures.

Besides studying the dephasing mechanisms in intersubband transitions, this technique is also extended to determine the mobility of carriers in semiconductors with subwavelength resolution. Free electrons in a doped semiconductor are well described by the Drude model, see Sec. 2.1.5. Within this framework, the momentum relaxation time τ_m (also known as mean free time) can be measured and thus the mobility can be deduced using Eq. 2.1.6. This is one of the most relevant parameters that describes the behavior of electrons in semiconductors and to the best of our knowledge it has not been determined with subwavelength resolution using THz near field techniques.

6.2 Electro-Modulation Spectroscopy

In the setup developed for this work, the THz pulse which is reflected on the surface is measured in the far field, see Fig. 4.2. The interaction of radiation with matter in general has many contributions (like for example phonons), however, the object of study in the current experiments are the intersubband transitions together with the motion of electrons in the $x-y$ parallel plane. These contributions cause a small change in the measured THz pulse. In the case of far field measurements it is around 1 % of the overall signal, but for near field experiments it can be lower than 0.2 %. It is therefore desirable to isolate the contribution to the overall measured signal of the electrons in the quantum well. This is achieved through electro modulation techniques, introduced for the far field by Allen *et al* [121] and recently extended to THz near field measurements [93]. In Sec. 5.2 it was shown how the parabolic quantum well could be depleted of electrons by applying a voltage between a Schottky contact and an Ohmic contact to the electron gas. Thus, the reflected THz pulse can be measured with the quantum well filled with or depleted of electrons. A comparison between the two pulses yields the contribution of the electrons in the well. In Fig. 6.1 a sketch of how this technique is realized in the far field is included.

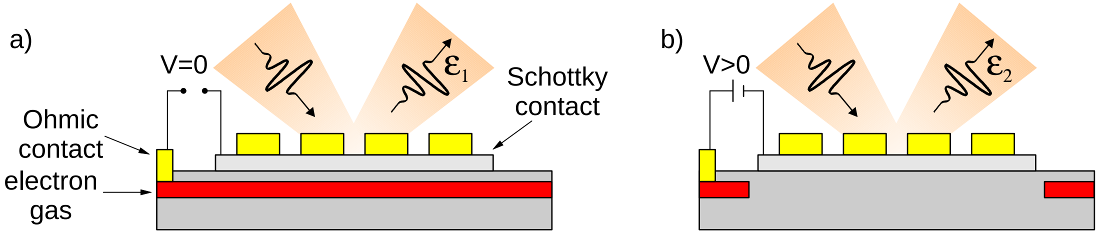

Figure 6.1: Sketch of the far field electro-modulation technique. a) no voltage is applied between the Ohmic and Schottky contacts and therefore electrons are present in the quantum well. The electric field of the THz pulse reflected in this case $\mathcal{E}_1$ contains information about the intersubband transition. b) when a voltage is applied the well is depleted of electrons and $\mathcal{E}_2$ contains no information regarding the intersubband transitions in the well.

When no voltage is applied between the Schottky and the Ohmic contact (Fig. 6.1a)), there are electrons in the well and therefore the electric field of the reflected THz pulse $\mathcal{E}_1$ contains information about the intersubband transition. This contribution can be ”switched off” by applying a voltage between the contacts (Fig. 6.1b)) which results in a depletion of the quantum well, so that $\mathcal{E}_2$ contains no information about the intersubband transition. Finally through the calculation of the differential electric field $\Delta\mathcal{E} = \mathcal{E}_1 - \mathcal{E}_2$ the contribution of the electrons in the quantum well is isolated.

This method is extended to near field measurements: The Schottky contact is replaced by a contacted probe, see Fig. 6.2. When a voltage between the probe and Ohmic contact is applied, depletion of electrons occurs in the vicinity of the probe tip. Therefore, in the case of near field measurements with the probe, the differential electric field $\Delta\mathcal{E}$ originates from the contribution of electrons in the quantum well confined to a spot with dimensions comparable with the probe tip diameter.

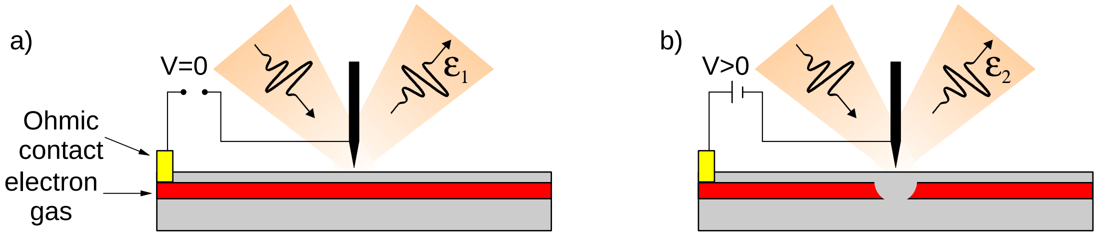

Figure 6.2: Sketch of the near field electro-modulation technique. The Schottky contact is replaced by a contacted probe. In a) no voltage is applied and the well contains electrons. b) when a voltage is applied between the probe and the Ohmic contact the well is depleted of electrons in the vicinity of the probe tip.

6.3 Extension of the Thin Film Equations for a Theoretical Analysis

The depletion of electrons takes place in the quantum well, which has a thickness much smaller than the wavelength employed. Therefore the analysis of the differential electric field $\Delta\mathcal{E}$ can be conveniently achieved within the framework of thin film equations [122–124].

The situation is illustrated in Fig. 6.3:An electromagnetic pulse characterized by its electric field $\mathcal{E}_i$ impinges from a medium with index of refraction n_1 onto a thin film of thickness d. This thin film represents the parabolic quantum well in which the electron density can be controlled. In the following, normal incidence is assumed which simplifies the calculations[1]. This approximation is justified since in the developed setup the angle of incidence forms an angle of 30° with the

---

[1] Other effects like the spectral efficiency of the grating coupler can be neglected since the period of the grating is much smaller than the wavelength of the radiation employed [12].

sample's surface normal (this assumption was further verified by comparing transmission and reflection measurements). A fraction of the incoming pulse will be transmitted through the thin film to a medium with index of refraction n_2, giving rise to $\mathcal{E}_t$ while another part will be reflected, $\mathcal{E}_r$ (Fig. refFig:thinfilm).

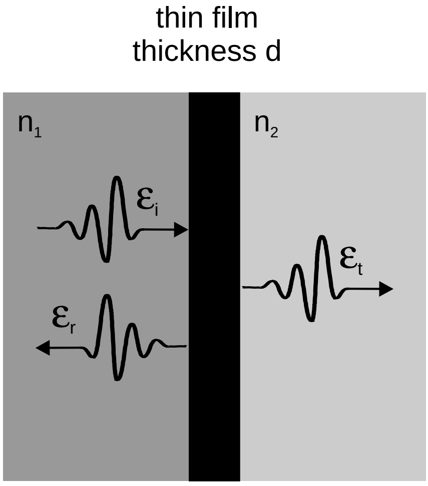

Figure 6.3: Incident, reflected and transmitted electric field at the interface of two dielectrics with indices of refraction n_1 and n_2. The interface consists of a thin film of thickness d.

Since the quantum well has a thickness and a skin depth much smaller than the wavelength of the THz radiation employed [94], the boundary condition for the electric field reads [123]:

$$\mathcal{E}_i + \mathcal{E}_r = \mathcal{E}_t. \tag{6.3.1}$$

The energy balance has also to be considered,

$$J_i = J_r + J_t + J_a, \tag{6.3.2}$$

where J_i, J_r and J_t are the incident, reflected and transmitted energy flux, respectively. J_a represents the absorbed energy flux due to Joule heating in the thin layer. This last equation can be re written in terms of the electric field,

$$\frac{\epsilon_o\, c\, n_1\, \mathcal{E}_i^2}{2} = \frac{\epsilon_o\, c\, n_1\, \mathcal{E}_r^2}{2} + \frac{\epsilon_o\, c\, n_2\, \mathcal{E}_t^2}{2} + \frac{\sigma\, d\mathcal{E}_t^2}{2}, \tag{6.3.3}$$

with σ being the complex conductivity of the thin layer. Combining Eqs. 6.3.1 and 6.3.3 an expression for the reflection and transmission coefficient is derived:

$$r_{12} = \frac{\mathcal{E}_r}{\mathcal{E}_i} = \frac{n_1 - n_2 - y}{n_1 + n_2 + y}, \tag{6.3.4}$$

and

$$t_{12} = \frac{\mathcal{E}_t}{\mathcal{E}_i} = \frac{2n_1}{n_1 + n_2 + y}, \tag{6.3.5}$$

with

$$y = \frac{\sigma\, d}{\epsilon_o\, c}. \tag{6.3.6}$$

The parabolic quantum well lies between GaAs layers so therefore a further simplification can be done by considering $n = n_1 = n_2$. This approximation has been successfully employed during the present work for the determination of the momentum relaxation time of carriers in a thin doped layer of GaAs [94]. Thus, the change of the reflected THz electric field $\Delta\mathcal{E} = \mathcal{E}_1 - \mathcal{E}_2$ as shown in Figs: 6.1 and 6.2 reads

$$\Delta\mathcal{E} = r_{12}\mathcal{E}_i = -\frac{y}{2n + y}\mathcal{E}_i. \tag{6.3.7}$$

For a thin layer $y << 2n$. Finally dividing the last equation by $\mathcal{E}_i$ yields:

$$\frac{\Delta\mathcal{E}}{\mathcal{E}_i} \approx -\frac{y}{2n} = -\frac{\sigma\, d}{2n\epsilon_o\, c}. \tag{6.3.8}$$

In this way the change of the measured THz electric field can be related to the conductivity σ of the electrons which are modulated under the Schottky contact in far field experiments or close to the probe tip in the case of near field measurements.

Depending on the frequency interval considered, there are two main contributions to the conductivity σ. Around the resonance frequency of the parabolic quantum well, the conductivity will arise from the intersubband transitions. For low frequencies, the conductivity will originate from the free motion of electrons in the plane perpendicular to the growth direction, which behave like a Drude gas. In the following both contributions will be addressed.

Intersubband transitions

In Sec. 2.3 an expression for the susceptibility $\chi(\omega)$ (Eq. 2.3.23), for electrons in a two level system was derived. The conductivity is related to the susceptibility [38, 56, 125]

$$\sigma = -i\epsilon_o \omega \chi(\omega). \tag{6.3.9}$$

Now the relative change $\Delta\mathcal{E}/\mathcal{E}$ can be linked to the susceptibility by combining Eqs. 6.3.9 and 2.3.23 with Eq. 6.3.8. This yields the following expression

$$\frac{\Delta\mathcal{E}}{\mathcal{E}} = i\frac{dn_e e^2}{2n\epsilon_o c m_{eff}} \frac{\omega}{\omega^2 - \omega_o^2 - i\omega/\tau_d} = iC_1 \frac{\omega}{\omega^2 - \omega_o^2 - i\omega/\tau_d}, \tag{6.3.10}$$

where the subscript i (incident) for the electric field has been dropped for simplicity since in the reported experiments $\Delta\mathcal{E} << \mathcal{E}$. The last equation deals with complex quantities, however one of the advantages of measuring the electric field of the THz radiation is that the modulus and the phase can be deduced. The modulus is:

$$\left|\frac{\Delta\mathcal{E}}{\mathcal{E}}\right| = \frac{dn_e e^2}{2n\epsilon_o c m_{eff}} \left|\frac{\omega}{\omega^2 - \omega_o^2 - i\omega/\tau_d}\right| = C_1 \frac{\omega\sqrt{(\omega^2 - \omega_o^2)^2 + (\omega/\tau_d)^2}}{(\omega^2 - \omega_o^2)^2 + (\omega/\tau_d)^2}. \tag{6.3.11}$$

It is convenient to square the last expression, which leads to

$$\left|\frac{\Delta\mathcal{E}}{\mathcal{E}}\right|^2 = C_1^2 \frac{\omega^2}{(\omega^2 - \omega_o^2)^2 + (\omega/\tau_d)^2}. \tag{6.3.12}$$

This equation relates the measured normalized change in the reflected THz electric field $\Delta\mathcal{E}/\mathcal{E}$ with the main object of study in the present work, the dephasing time τ_d. The dependence of $|\Delta\mathcal{E}/\mathcal{E}|^2$ with ω has a peak at the resonance frequency ω_o and a shape similar to a Lorentzian distribution with a full width at half maximum related to τ_d [1].

The analysis of the dephasing times in terms of Eq. 6.3.12 has several advantages. Many parameters, like the electron density n_e and the thickness of the layer d can be grouped in a general constant C_1. By fitting the results to the derived equation, the resonance frequency $\omega_o = 2\pi \cdot f_o$ and the dephasing time t_d can be extracted regardless of all the parameters in C_1.

Drude electron gas

In the plane perpendicular to the growth direction of the parabolic quantum well, electrons are not confined, see Eq. 2.3.2. The motion in this plane can be described using the Drude model. In

---

[1] However, since the expression derived in Eq. 6.3.12 differs from a Lorentzian, a simple relationship between the full width at half maximum and τ_d can not be obtained.

section 2.1.5 an expression was obtained which describes the conductivity arising from electrons behaving like a Drude gas, $\sigma(\omega) = \sigma_o/(1+i\omega\tau_m)$ with $\sigma_o = n_e q^2 \tau_m / m_{eff}$. Similar as done before for intersubband transitions, this expression can be combined with equation 6.3.8 which provides

$$\frac{\Delta\mathcal{E}}{\mathcal{E}} = \frac{d n_e e^2}{2n\epsilon_o c m_{eff}} \frac{\tau_m}{1 + i\omega\tau_m}. \tag{6.3.13}$$

Again like in the previous case, the same analysis can be performed and the square of the modulus derived reads

$$\left|\frac{\Delta\mathcal{E}}{\mathcal{E}}\right|^2 = C_1^2 \frac{\tau_m^2}{1 + \omega^2\tau_m^2}. \tag{6.3.14}$$

The measured normalized change in the reflected THz electric field $\Delta\mathcal{E}/\mathcal{E}$ is related to the momentum relaxation time τ_m. It is important to note that the last equation can be obtained from Eq. 6.3.12 assuming $\omega_o = 0$, as expected from the Drude model. This means that the electron response due to the intersubband transition and the motion in the perpendicular plane can be treated analogously with different centre frequencies. Depending on ω_o, τ_m and τ_d there will be an overlap between both contributions, which for the parameters in the present case is negligible. The situation is illustrated in Fig. 6.4 which shows a calculation for the Drude gas and the intersubband response at $\omega_o = 2\pi \cdot 2$THz.

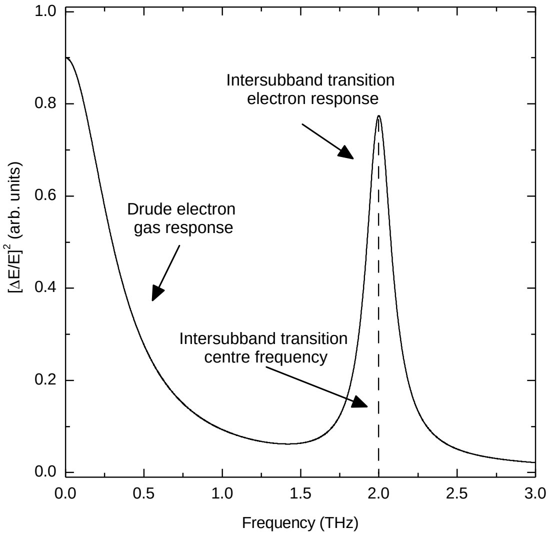

Figure 6.4: Calculation for the Drude gas and intersubband transition response at $\omega_o = 2\pi \cdot 2$THz

For cases like the one depicted in the previous figure in which both responses can be identified, ω_o, τ_m and τ_d can be deduced from a single measurement by studying different parts of the spectrum. This derivation, developed for the present work, will be employed to analyze the results obtained for the far field as well as the near field experiments.

6.4 Results

Far field measurements together with near field measurements were performed using electro modulation techniques as depicted in Figs. 6.1 and 6.2 on the parabolic quantum well structure introduced in Sec. 5.1. All the experiments were done in a cryostat (see Fig. 4.2) at a temperature of 4 K. Care was taken that during the data acquisition and cooling down process the sample remained in the dark to avoid photoexcitation of electrons into long-lived trap states. In order to modulate the number of electrons in the quantum well a voltage between -0.2 and 10 V was applied between the Ohmic and the Schottky contact for far field measurements. In the case of the near field measurements the probe tip was employed as a Schottky contact for electro-modulation. The applied voltage was modulated at a frequency of 10 Hz with a square waveform.

The near field experiments were performed using a tungsten probe with a tip diameter of approximately 500 nm. The distance between the probe tip and the parabolic quantum well structure was set to 20 nm and monitored during the measurement at a frequency of 1000 Hz using shear force techniques (see Sec. 4.4).

For the two voltages applied and therefore for the quantum well with and without electrons, the THz electric field was recorded in the far field. Further analysis of the data yields the differential electric field $\Delta\mathcal{E} = \mathcal{E}_1 - \mathcal{E}_2$ for both the far field and near field experiments. The results are depicted in Fig. 6.5. In the upper part of Fig. 6.5a), the reflected THz pulse is included as a reference. The differential electric field for the far field experiment is $\Delta\mathcal{E}_{ff}/\mathcal{E} \approx 1/250$ whereas in the near field case it reads $\Delta\mathcal{E}_{nf}/\mathcal{E} \approx 1/1500$. In Fig. 6.5b) the corresponding amplitude spectrum is included.

The presence of both responses, the Drude and intersubband transition complicates the analysis of the differential electric field in time domain. However, at the initial part of the THz pulse, both differential signals resemble approximately the reflected THz pulse, slightly shifted. This means that $\mathcal{E}_1$ and $\mathcal{E}_2$ are also slightly dephased with negligible absorption, a characteristic of the Drude response in the initial ballistic regime [126]. In the final part of the THz pulse, after the initial high amplitude oscillation the far field differential signal shows oscillations with a period corresponding to a frequency of around 2 THz. This is the behavior expected for the intersubband transition response. In the near field trace, the same behavior can not be clearly noted and therefore it is more convenient to work in frequency space.

Through an analysis in frequency space of the differential electric field signal $|\Delta\mathcal{E}/\mathcal{E}|^2$, both responses can be more clearly isolated. In this way, the momentum relaxation time τ_m, the intersubband transition frequency $\omega_o = 2\pi \cdot f_o$ and the dephasing time τ_d can be deduced.

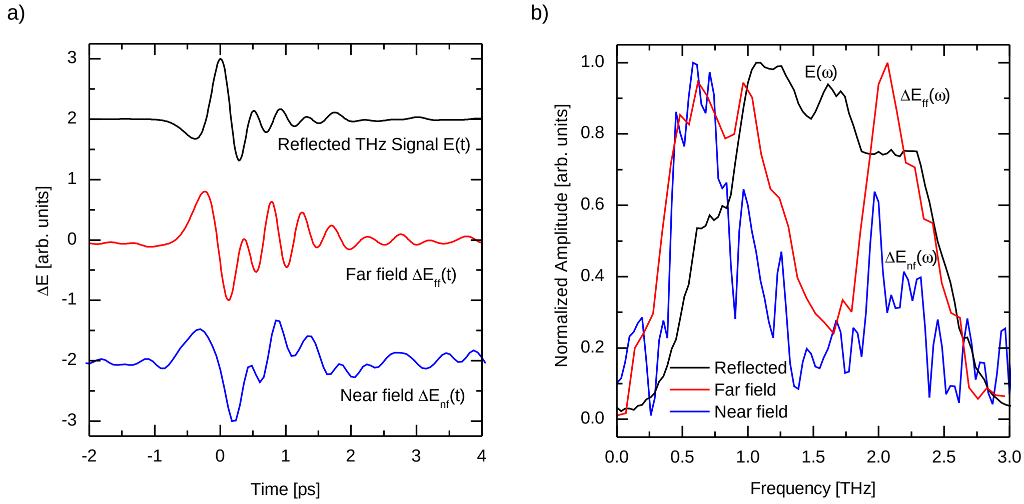

Figure 6.5: a) Reflected THz pulse together with the differential electric field for the far and near field measurements. The differential traces were scaled by a factor of $\Delta\mathcal{E}_{ff}/\mathcal{E} \approx 1/250$ and $\Delta\mathcal{E}_{nf}/\mathcal{E} \approx 1/1500$. b) Corresponding normalized amplitude spectrum.

6.4.1 Drude Response

In order to study the Drude response of the electron gas in the parabolic quantum well, a Fourier transform of $|\Delta\mathcal{E}/\mathcal{E}|^2$ extracted from the differential signals included in Fig. 6.5a) was performed. The first fraction (between 0.5 and 1.5 THz) of the spectrum was analyzed. In Fig. 6.6, $|\Delta\mathcal{E}/\mathcal{E}|^2$ is plotted for the far and near field measurements. The traces obtained resemble the first part of the spectrum (Drude response) of the calculation included in Fig. 6.4. The solid lines represent a least mean square fit using Eq. 6.3.14. From the fit, the momentum relaxation time is estimated to be $\tau_m^{ff} = (350 \pm 150)$ fs for the far field measurement and $\tau_m^{nf} = (500 \pm 200)$ fs in the case of the near field experiment [1]. Considering the donor concentration and electron surface density in the well, scattering will occur on the nanometer scale and therefore no significant difference between the near field and far field values is expected, as obtained in the measurement. The momentum relaxation times deduced are also in good agreement with low temperature measurements of thin doped GaAs layers [94]. The uncertainty in the determination of the relaxation times is rather considerable which is due to the fact that the THz radiation employed has negligible frequency components for frequencies under 0.4 THz (see Fig. 3.2 b)). Nevertheless, these results show the potential of this technique for the determination of the momentum relaxation time of carriers and therefore the mobility with subwavelength resolution.

---

[1] In the case of the near field experiments, excitation of the Drude gas is possible since the electric field in the vicinity of the probe tip has multiple directions, see for example Figs: 3.7 and 3.8a).

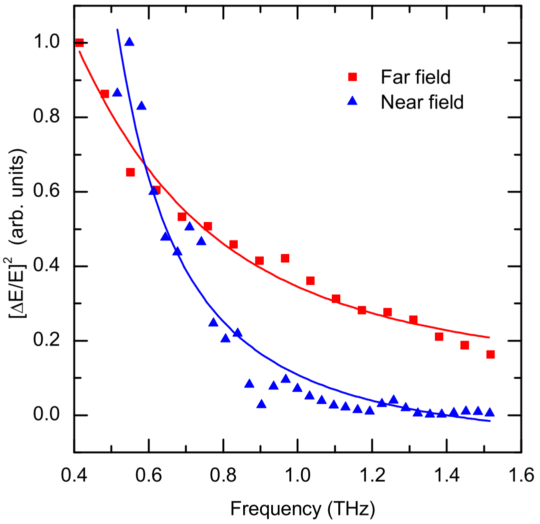

Figure 6.6: Square of the normalized differential electric field signal, $|\Delta\mathcal{E}/\mathcal{E}|^2$ for the far and near field measurements. The solid lines represent a least mean square fit using Eq. 6.3.14, for the Drude response of an electron gas.

6.4.2 Intersubband Transitions

The study of the intersubband transitions was performed in a similar manner as in the case of the Drude response, in Fourier space. The analysis was done in a range around the expected intersubband transition frequency, ω_o=$2\pi\cdot$ 2 THz. Fig. 6.7a) shows the results obtained for $|\Delta\mathcal{E}/\mathcal{E}|^2$ for the near field and far field measurements.

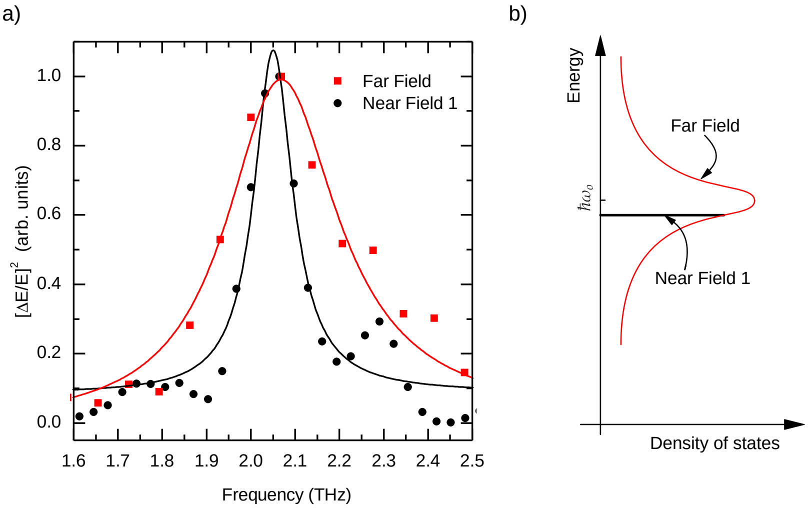

Figure 6.7: a) Square of the normalized differential electric field signal, $|\Delta\mathcal{E}/\mathcal{E}|^2$ for the far and near field measurements. The solid lines represent a least mean square fit using a Eq. 6.3.12, for the intersubband transition response of an electron gas. b) Sketch of the distribution of the density of states as a function of the transition energy. The distribution has a peak at the estimated centre frequency ω_o. In far field measurements the sampled transition energies are broad while in near field experiments a sharper transition is expected.

As in the previous case, the results are in good agreement with the calculation included in Fig. 6.4 for the intersubband transition. The solid lines represent a least mean square fit using Eq. 6.3.12. From this fit the centre frequency $\omega_o = 2\pi \cdot f_o$ and the dephasing time τ_d can be deduced, the values are listed in Table 6.1.

Measurement	Centre Frequency f_o [THz]	Dephasing Time τ_d [ps]
Far field	(2.07±0.02)	(0.49±0.08)
Near field 1	(2.05±0.02)	(1.5±0.2)
Near field 2	(1.98±0.01)	(2.3±0.3)

Table 6.1: Centre frequency f_o and dephasing time τ_d for the far and near field measurements included in Figs: 6.7 and 6.8. The values listed were obtained through a numerical fit using Eq. 6.3.12.

The values for the centre frequency agree with the numerical calculation performed in Sec. 5.3 (ω_o=$2\pi\cdot$ 2 THz). For the far field measurement the resonance frequency appears to be slightly shifted towards higher frequencies, this effect has been previously attributed to the presence of the Schottky contact [127]. Also the applied voltage can deform the shape of the quantum well leading to a shift of the resonance [128].

In the case of the near field measurement, the dephasing time deduced is three times bigger as compared to the dephasing time in the far field measurement. This effect is attributed to inhomogeneous broadening. If inhomogeneous broadening occurs, a distribution of transition energies centered around the estimated ω_o is to be expected (see Fig. 6.7b)). In the far field measurements in which an area of ≈1 mm^2 is studied, several transition energies can be simultaneously sampled and therefore a lower dephasing time is observed. For near field measurements, the sampling area is six orders of magnitude smaller, i.e. ≈1 μm^2 and thus, fluctuations in the transition energy are less probable. This leads to higher dephasing rates.

In order to further verify this finding, near field measurements were performed at different positions on the quantum well sample, separated by approximately 2 μm. The results are included in Fig. 6.8a). As expected, the dephasing times are higher than in the far field measurement. In addition to that, the centre frequencies of both near field measurements slightly differ around the estimated value ω_o. This effect can also be explained in terms of inhomogeneous broadening: At different positions on the parabolic quantum well sample, different transition energies can be sampled (see Fig. 6.8b)).

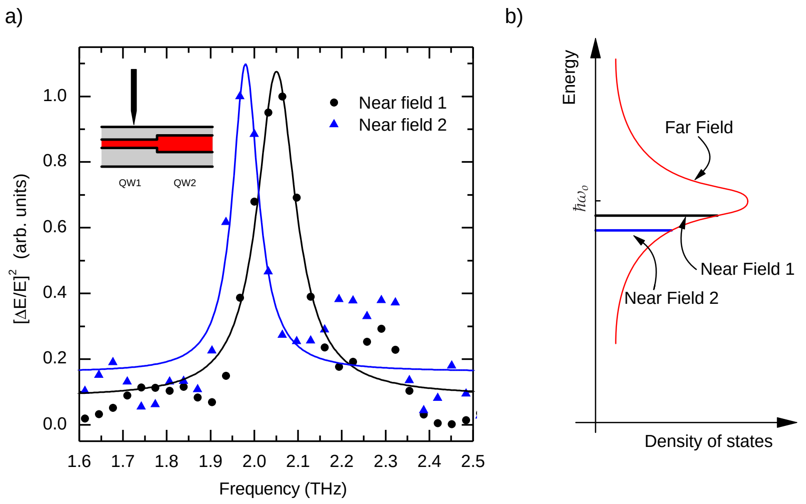

Figure 6.8: a) Square of the normalized differential electric field signal, $|\Delta\mathcal{E}/\mathcal{E}|^2$ for two different near field measurements. The solid lines represent a least mean square fit using Eq. 6.3.12, for the intersubband transition response of an electron gas. The inset shows a sketch of a near field measurement in which fluctuations of the quantum well (QW) thickness, QW1 and QW2 lead to inhomogeneous broadening. b)Sketch of the distribution of the density of states as a function of the transition energy. The transition energies of both near field measurements are outlined.

6.5 Summary

In this chapter the results for the far and near field THz spectroscopy measurements on parabolic quantum well structures were presented. These experiments were enabled by electromodulation techniques in which the contribution of electrons under a metallic contact could be isolated. In order to interpret the results and to obtain a qualitative understanding of the dephasing mechanisms, a theoretical model was developed to study both the intersuband transition response as well as the Drude response of the free electron gas. To date, this measurements are the first THz near field experiments of the local response of electrons at cryogenic temperatures. The momentum relaxation time τ_m could be estimated in good agreement with previous measurements which indicates the potential of this technique for determining the mobility with subwavelength resolution. Finally, the dephasing of the intersubband transition was studied through a comparison between far field and near field results. In this case, several near field measurements were taken at different positions. The near field measurements show higher dephasing times τ_d and a distribution of centre frequencies, a clear evidence of inhomogeneous broadening.

7 Conclusions and Outlook

In this dissertation, it was shown how far field and near field THz spectroscopy techniques can be combined to study electronic excitations in semiconductor heterostructures. Electrons in such structures show intersubband transitions along the quantized direction and a Drude response in the perpendicular plane. For the first time, the main parameters that characterize both responses, the dephasing time τ_d of the intersubband transition and the momentum relaxation time τ_m of free electrons within the Drude model were obtained with extreme subwavelength spatial resolution using aperture-less THz near field microscopy in a contactless manner. In addition, through a comparison between far field and near field experiments insight into the mechanisms that lead to broadening of the intersubband transition lines was attained. Inhomogeneous broadening was found to predominantly affect the coherence of the intersubband transitions in parabolic quantum wells.

The momentum relaxation time τ_m, is one of the most important parameters to characterize charge transport in solids within the Drude model. This parameter is essential for predicting device performance in semiconductor technology and high electron mobility transistors. It was deduced quantitatively for the first time during this work with subwavelength spatial resolution at cryogenic temperatures. No significant difference was obtained between the far field $\tau_m^{ff} = (350 \pm 150)$ fs and near field $\tau_m^{nf} = (500 \pm 200)$ fs values as expected considering the carrier densities involved in which the mean free path is in the nanometer range. These results show that this technique can be extended to the determination of the momentum relaxation time in current semiconductor devices with dimensions much smaller than the wavelength of the THz radiation.

The dephasing time τ_d, defines the decay of the coherence of electrons performing intersubband transitions in quantum wells. The main dephasing processes in quantum wells can be divided into homogenous and inhomogeneous broadening although to date a detailed understanding of the individual contributions could not be achieved.

A comparison between far field and near field experiments, with a sampling area six orders of magnitude smaller was performed ($\approx 1\text{mm}^2$ in the far field and $\approx 1\mu\text{m}^2$ for the near field). The near field measurements were taken at different positions on the sample separated in the micrometer range. The results for the near field experiments show a dephasing time as high as (2.3 ± 0.3) ps which is approximately four times higher as compared to far field measurements. In addition, variations around the expected intersubband transition frequency were also observed in near field experiments. This constitutes strong evidence that the intersubband transition line is inhomogeneously broadened.

In order to perform these measurements substantial improvements to the experimental methodology were made. Previously, most near field measurements with subwavelength resolution were hindered by experimental limitations. During this work a novel setup was designed and built to operate at cryogenic temperatures, focusing primarily on the enhancement of the signal to noise ratio and a method to eliminate artifacts arising from the topology of the samples.

To improve the THz signal, different processes that yield THz emission were identified [101] and novel microstructured THz emitters were fabricated [96]. These structures show several advantages as compared to previously employed devices: They are less complex to fabricate, they have a higher signal output and they can be modulation biased allowing for narrow bandwidth detection which optimizes the signal detection. In summary, all these factors lead to an improvement of the signal to noise ratio by at least an order of magnitude. Thus, the data acquisition time is significantly reduced and new experiments enabled.

A shear force technique was implemented to control the distance between probe and sample's surface [105]. In this way, artifacts related to variations in the sample's surface profile were avoided. Moreover, with this technique the topography of the sample's surface was determined simultaneously with THz near field measurements, which facilitates the data analysis. Therefore, objects with extreme subwavelength dimensions, like GaAs nanowires, could be detected. Finally, the improvement in the distance control contributed to an increase of the spatial resolution. A maximum value of 65 nm was obtained, which constitutes to date the highest spatial resolution for THz broadband radiation.

It was also shown during this work, that electro-modulation techniques can be applied to isolate the response of electrons located under a metallic contact. In this way, the contribution of electrons in the quantum well were addressed. This method was extended to near field experiments in which measurements were performed in a contact-less manner using a metallic probe. This is particularly relevant for devices where physical contacts may affect the quantum properties under study.

Besides the contributions to the experimental methodology, a model to interpret the electro-modulation spectroscopy experiments was developed. This model is based on an extension of the optical thin film equations and was successfully applied for both the intersubband transition response and also the free electron gas response. As a result, the dephasing time τ_d and the momentum relaxation time τ_m were determined.

For on going research and future directions, the presented technique could be applied to the determination of the momentum relaxation time of GaAs nanowires. To date, this parameter has only been estimated in the far field for an ensemble of nanowires [129]. THz near field microscopy could also be employed for deducing the carrier mobility in transistors with nanometer dimensions since previous works have already shown a contrast between source, drain and gate contacts in the THz range [79]. Finally the dephasing mechanisms of semiconductor quantum dots could be studied combining far and near field techniques.

Appendix

A Proportional-Integral (PI) Controller

A proportional-integral (PI) controller consists of a control loop feedback. In the context of this work, it was implemented to control the distance between the probe's tip and the sample's surface. It determines the difference (error) between a measured value, in this case the tuning fork amplitude and a desired setpoint. The controller then attempts to minimize this error by outputting a signal that affects the measured value.

The operating algorithm involves typically two parameters: The proportional and the integral values. The proportional value determines the reaction to the current error whereas the integral value determines the reaction based on the sum of recent errors. Both values need to be adjusted to reduce overshooting and oscillations around the desired setpoint.

The signal outputted by the controller is a voltage that leads to a contraction or expansion of a piezo actuator and therefore it determines the distance between probe and sample. This voltage V_c, reads

$$V_c(t) = P_o + I_o, \tag{A.1}$$

where P_o and I_o are the proportional and integral contributions respectively. The first term on the right side can be expressed as

$$P_o = C_p e_r(t), \tag{A.2}$$

with C_p being the proportional gain, one of the parameters to be tuned and $e_r(t)$ is the error or difference between the measured and desired value. The integral contribution is given by

$$I_o = C_i \int_0^t e_r(\tau) d\tau, \tag{A.3}$$

where C_i is the integral gain, the second parameter to be tuned. For a discrete implementation this last integral is replaced by a sum

$$\int_0^t e(\tau)d\tau \approx \sum_{i=1}^{k} e_r(t_i)\Delta t. \tag{A.4}$$

This algorithm was employed in the present work. The tuning parameters C_p and C_i where adjusted considering the piezo actuator expansion coefficient for different temperatures and the distance in which the tuning fork amplitude is reduced to zero when approaching the sample's surface.

B Allowed Intersubband Transitions on Parabolic Quantum Wells

In this appendix, the allowed intersubband transitions on parabolic quantum wells induced by optical excitations will be derived. In section 2.3.2, the interaction Hamiltonian with a classical radiation field was introduced. Within the electric dipole approximation [25], the interaction hamiltonian can be reduced to the calculation of the dipole moment.

For a parabolic potential in z direction, the dipole moment for an electron with charge q between eigenstates $\mid \varphi_n(z)\rangle$ and $\mid \varphi_{n'}(z)\rangle$ is given by $\langle \varphi_n(z) \mid qz \mid \varphi_{n'}(z)\rangle$. The Hermitian operator position z, can be written in terms of the creation operator

$$a^{\dagger} = \sqrt{\frac{m_{eff}\omega_o}{2\hbar}}\left(z - \frac{ip_z}{m_{eff}\omega_o}\right), \tag{B.1}$$

and the annihilation operator

$$a = \sqrt{\frac{m_{eff}\omega_o}{2\hbar}}\left(z + \frac{ip_z}{m_{eff}\omega_o}\right), \tag{B.2}$$

with m_{eff} the electron effective mass and ω_o the resonance frequency. Combining the last two equations,

$$z = \sqrt{\frac{\hbar}{2m_{eff}\omega_o}}(a + a^{\dagger}). \tag{B.3}$$

The effect of applying the creation and annihilation operators onto eigenstates is the following,

$$a^{\dagger} \mid \varphi_n(z)\rangle = \sqrt{n+1} \mid \varphi_{n+1}(z)\rangle \tag{B.4}$$

and

$$a \mid \varphi_n(z)\rangle = \sqrt{n} \mid \varphi_{n-1}(z)\rangle. \tag{B.5}$$

The dipole moment can now be calculated as

$$\begin{aligned} \langle \varphi_n(z) \mid qz \mid \varphi_{n'}(z)\rangle &= q\sqrt{\frac{\hbar}{2m_{eff}\omega_o}}\langle \varphi_n(z) \mid (a + a^{\dagger}) \mid \varphi_{n'}(z)\rangle \\ &= q\sqrt{\frac{\hbar}{2m_{eff}\omega_o}}\left(\sqrt{n+1}\delta_{n',n+1} + \sqrt{n}\delta_{n',n-1}\right). \end{aligned} \tag{B.6}$$

Therefore, only transitions between adjacent states are allowed, since n' needs to be either $n+1$ or $n-1$.

List of Symbols

Symbol	Denomination	Symbol	Denomination
A	Surface	m_{eff}	Effective mass
$\mathbf{A}$	Vector potential	m_o	Free electron mass
c	Speed of light	n_e	Electron density
C	Capacitance	N_d	Donor density
e	Fundamental charge	p	Momentum
$\mathbf{e}$	polarization vector	P	Power
E	Energy	P_m	Macroscopic polarization
E_a	Acceptor energy	q	Electron charge
E_c	Conduction band energy	Q	Quality factor
E_d	Donor energy	Q	Charge
E_f	Fermi energy	r	Reflection coefficient
E_g	Energy band gap	r_t	Tip radius
E_v	Valence band energy	R	Resistance
E_{vac}	Vacuum level	sd	Standard deviation
$\mathcal{E}$	Electric field	SNR	Signal to noise ratio
f	Frequency	t	Time
$\hbar$	Reduced Planck constant	t	Transmission coefficient
H	Hamiltonian	T	Temperature
i	Imaginary unit	v_d	Drift velocity
I	Current	V	Voltage
I_i	Intensity	V_{bi}	Built-in potential
j	Current density	V_r	Reverse bias
k_B	Boltzmann constant	x	Aluminum content
l	Length	Z_o	Vacuum impedance
L	Inductance		

Table B.1: List of latin symbols.

Symbol	Denomination
α	Polarizability
ϵ	Dielectric function
ϵ_o	Vacuum permittivity
χ	Susceptibility
δ	Dirac delta function
Δ	Difference
η	Power dissipation
ϕ	Potential
γ	Damping rate
κ	Spring constant
λ	Wavelength
μ	Chemical potential
μ	Mobility
μ_d	Dipole moment
ω	Angula frequency
ω_o	Oscillator frequency
π	3.1415...
τ_e	Electron lifetime
τ_d	Dephasing time
τ_m	Mean free time
τ_e	Electron lifetime
σ	Conductivity
σ_o	DC conductivity

Table B.2: List of greek symbols.

List of Figures

List of Tables

Bibliography

[1] G. E. Moore. Cramming more components onto integrated circuits. *Electronics* **38**, 8 (1965).

[2] M. H. Devoret and R. J. Schoelkopf. Amplifying quantum signals with the single-electron transistor. *Nature* **406**, 1039 (2000).

[3] M. van Exter and D. Grischkowsky. Optical and electronic properties of doped silicon from 0. 1 to 2 THz. *Appl. Phys. Lett.* **56**, 1694 (1990).

[4] M. van Exter and D. Grischkowsky. Carrier dynamics of electrons and holes in moderately doped silicon. *Phys. Rev. B* **41**, 12140 (1990).

[5] R. Ascazubi, O. C. Akin, T. Zaman, R. Kersting and G. Strasser. Dephasing in modulation-doped quantum structures probed by THz time-domain spectroscopy. *Appl. Phys. Lett.* **81**, 4344 (2002).

[6] J. N. Heyman, R. Kersting and K. Unterrainer. Time–domain measurement of intersubband oscillations in a quantum well. *Appl. Phys. Lett.* **72**, 644 (1998).

[7] R. Kersting, R. Bratschitsch, G. Strasser, K. Unterrainer and J. N. Heyman. Sampling a terahertz dipole transition with subcycle time resolution. *Opt. Lett.* **25**, 272 (2000).

[8] B. Williams, S. Kumar, Q. Hu and J. Reno. Operation of terahertz quantum-cascade lasers at 164 K in pulsed mode and at 117 K in continuous-wave mode. *Opt. Express* **13**(9), 3331 (2005).

[9] M. A. Belkin, F. Capasso, F. Xie, A. Belyanin, M. Fischer, A. Wittmann and J. Faist. Room temperature terahertz quantum cascade laser source based on intracavity difference-frequency generation. *Applied Physics Letters* **92**(20), 201101 (2008).

[10] N. W. Ashcroft and N. D. Mermin. *Solid State Physics*. Holt, Rinehart and Winston (1987).

[11] S. M. Sze. *Semiconductor Devices*. John Wiley & Sons (1985).

[12] M. Helm. The basic physics of intersubband transitions. In R. K. Willardson and E. R. Weber, Hg., *Semiconductors and Semimetals, Intersubband Transitions in Quantum Wells: Physics and Device Applications I*, Bd. 62, S. 1. Academic Press (2000).

[13] T. Elsaesser and M. Woerner. Femtosecond infrared spectroscopy of semiconductors and semiconductors nanostructures. *Physics Reports* **321**, 253 (1999).

[14] T. Heinzel. *Mesoscopic Electronics in Solid State Nanostructures*. WILEY-VCH (2003).

[15] S. M. Sze. *Physics of semiconductor devices*. John Wiley & Sons, Wiley-Science (2007).

[16] J. Davies. *The Physics of Low-Dimensiona Semiconductors*. Cambridge University Press (1998).

[17] M. Balkanski and R. F. Wallis. *Semiconductor Physics and Applications*. Oxford University Press (2000).

[18] R. Dingle, H. L. Störmer, A. C. Gossard and W. Wiegmann. Electron mobilities in modulation-doped semiconductor heterojunction superlattices. *Appl. Phys. Lett.* **33**, 665 (1978).

[19] P. F. Hopkins, A. J. Rimberg, E. G. Gwinn, R. M. Westervelt, M. Sundaram and A. C. Gossard. Low-density high-mobility electron gas in wide parabolic GaAs/$Al_xGa_{1-x}As$ wells. *Appl. Phys. Lett.* **57**(26), 2823 (1990).

[20] P. F. Hopkins, K. L. Campman and A. C. Gossard. Growth and characterization of Be modulation doped wide parabolic GaAs/$Al_xGa_{1-x}As$ wells. *Journal of Crystal Growth* **127**, 798 (1993).

[21] L. Brey, N. F. Johnson and J. Dempsey. Electronic and optical properties of a superlattice in a parabolic potential. *Phys. Rev. B* **42**(5), 2886 (1990).

[22] M. Sundaram, J. S. J. Allen, M. R. Geller, P. F. Hopkins, K. L. Campman and A. C. Gossard. Infrared absorption of holes in a parabolic quantum well. *Appl. Phys. Lett.* **65**(17), 2226 (1994).

[23] R. C. Miller, A. C. Gossard, D. A. Kleinman and O. Munteanu. Parabolic quantum wells with the GaAs – $Al_xGa_{1-x}As$ system. *Phys. Rev. B* **29**(6), 3740 (1984).

[24] M. Sundaram, A. Wixforth, R. S. Geels, A. C. Gossard and J. H. English. A direct method to produce and measure compositional grading in $Al_xGa_{1-x}As$ alloys. *Journal of Vacuum Science & Technology B: Microelectronics and Nanometer Structures* **9**(3), 1524 (1991).

[25] J. Sakurai. *Modern Quantum Mechanics*. Addison Wesley (1993).

[26] W. Kohn. Cyclotron resonance and de Haas–van Alphen oscillations of an interacting electron gas. *Phys. Rev.* **123**, 1242 (1961).

[27] K. Karrai, X. Ying, H. D. Drew and M. Shayegan. Collective cyclotron resonance in a quasi-three-dimensional electron gas. *Phys. Rev. B* **40**, 12020 (1989).

[28] K. Craig, B. Galdrikian, J. N. Heyman, A. G. Markelz, J. B. Williams, M. S. Sherwin, K. Campman, P. F. Hopkins and A. C. Gossard. Undressing a collective intersubband excitation in a quantum well. *Phys. Rev. Lett.* **76**, 2382 (1996).

[29] O. Svelto. *Priciples of lasers*. Plenum Press (1998).

[30] D. R. Luhman, D. C. Tsui, L. N. Pfeiffer and K. W. West. Electronic transport studies of a systematic series of GaAs/AlGaAs quantum wells. *Appl. Phys. Lett.* **91**(7), 072104 (2007).

[31] R. Bratschitsch, T. Müller, R. Kersting, G. Strasser and K. Unterrainer. Coherent THz emission from optically pumped parabolic quantum wells. In *CLEO 2000* (2000).

[32] P. Yu and M. Cardona. *Fundamentals of Semiconductors*. Springer (1995).

[33] Y. Fu and M. Willander. Alloy scattering in GaAs/AlGaAs quantum well infrared pohotodetector. *J. Appl. Phys.* **88**, 288 (2000).

[34] H. Sakaki, T. Noda, K. Hirakawa, M. Tanaka and T. Matsusue. Interface roughness scattering in GaAs/AlAs quantum wells. *Appl. Phys. Lett.* **51**, 1934 (1987).

[35] B. Yang, Y. Cheng, Z. Wang, J. Liang, Q. Liao, L. Lin, Z. Zhu, B. Xu and W. Li. Interface roughness scattering in GaAs-AlGaAs modulation-doped heterostructures. *Appl. Phys. Lett.* **65**, 3329 (1994).

[36] J. F. I. Waldmüller, S.-C. Lee, A. Knorr, M. Woerner, K. Reimann, R. A. Kaindl, T. Elsaesser, R. Hey and K. H. Ploog. Optical dephasing of coherent intersubband transitions in a quasi-two-dimensional electron gas. *Phys. Rev. B* **69**, 205307 (2004).

[37] K. Shimoda. *Introduction to Laser Physics*. Springer Verlag (1984).

[38] G. A. Reider. *Photonik*. Springer (1997).

[39] W. Schottky. Halbleitertheorie der Sperrschicht. *Naturwissenschaften* **26**, 843 (1938).

[40] B. P. Gorshunov, A. Volkov, I. E. Spektor, A. S. Prokhorov, A. A. Mukhin, M. Dressel, S. Uchida and A. Loidl. Terahertz BWO-spectroscopy. *Int. J. Infr. Mill. Waves* **26**, 1217 (2005).

[41] E. R. Brown, K. A. McIntosh, K. B. Nichols and C. L. Dennis. Photomixing up to 3.8 THz in low-temperature-grown GaAs. *Appl. Phys. Lett* **66**, 285 (1995).

[42] D. E. Spence, P. N. Kean and W. Sibbett. 60–fsec pulse generation from a self–mode–locked Ti:sapphire laser. *Opt. Lett.* **16**, 42 (1991).

[43] P. M. W. French. The generation of ultrashort laser pulses. *Rep. Prog. Phys.* **58**, 169 (1995).

[44] F. Krausz. Tracking light oscillations: attosecond spectroscopy comes of age. *Micron* **13**, 62 (2002).

[45] N. Katzenellenbogen and D. Grischkowsky. Efficient generation of 380 fs pulses of THz radiation by ultrafast laser pulse excitation of a biased metal-semiconductor interface. *Appl. Phys. Lett.* **58**, 222 (1991).

[46] M. C. Beard, M. Turner and C. A. Schmuttenmaer. Transient photoconductivity in GaAs as measured by time-resolved terahertz spectroscopy. *Phys. Rev. B* **62**, 15764 (2000).

[47] Y. Deng, R. Kersting, V. Roytburd, J. Xu, R. Ascazubi, K. Liu, X.-C. Zhang and M. S. Shur. Spectrum determination of terahertz sources using a Fabry-Perot interferometer and bolometer. *Int. J. Infr. Mill. Waves* **25**, 215 (2004).

[48] C. A. Schmuttenmaer. Exploring dynamics in the far-infrared with terahertz spectroscopy. *Chem. Rev.* **104**, 1759 (2004).

[49] J. Ahn, A. V. Efimov, R. D. Averitt and A. J. Taylor. Terahertz waveforms synthesis via optical rectification of shaped ultrafast laser pulses. *Opt. Expr.* **11**, 2486 (2003).

[50] T. Löffler, T. Hahn, M. Thomson, F. Jacob and H. G. Roskos. Large-area electro-optic ZnTe terahert emitters. *Opt. Expr.* **13**, 5353 (2005).

[51] B. Bartal, I. Z. Kozma, A. G. Stepanov, G. Almási, J. Kuhl, E. Riedle and J. Hebling. Toward generation of μJ range sub-ps THz pulse by optical rectification. *Appl. Phys. B* **86**, 419 (2007).

[52] M. B. Johnston, D. M. Whittaker, A. Corchia, A. G. Davies and E. H. Linfield. Simulation of terahertz generation at semiconductor surfaces. *Phys. Rev. B* **65**, 165301 (2002).

[53] J. N. Heyman, P. Neocleous, D. Herbert, P. A. Crowell, T. Müller and K. Unterrainer. Terahertz emission from GaAs and InAs in a magnetic field. *Phys. Rev. B* **64**, 085202 (2001).

[54] D. H. Auston. Picosecond optoelectronic switching and gating in silicon. *Appl. Phys. Lett.* **26**, 101 (1975).

[55] D. H. Auston, K. P. Cheung and P. R. Smith. Picosecond photoconducting Hertzian dipoles. *Appl. Phys. Lett.* **45**, 284 (1984).

[56] J. D. Jackson. *Classical Electrodynamics*. John Wiley & Sons (1998).

[57] K. Reimann. Table-top sources of ultrashort THz pulses. *Rep. Prog. Phys.* **70**, 1597 (2007).

[58] D. H. Auston, P. Lavallard, N. Sol and D. Kaplan. An amorphous silicon photodetector for picosecond pulses. *Appl. Phys. Lett.* **36**, 66 (1980).

[59] F. Peter, S. Winnerl, S. Nitsche, A. Dreyhaupt, H. Schneider and M. Helm. Coherent terahertz detection with a large-area photoconductive antenna. *Appl. Phys. Lett.* **91**, 081109 (2007).

[60] Q. Wu and X.-C. Zhang. Free–space electro–optic sampling of THz beams. *Appl. Phys. Lett.* **67**, 3523 (1995).

[61] N. C. J. van der Valk, T. Wenckebach and P. C. M. Planken. Full mathematical description of electro-optic detection in optically isotropic crystals. *JOSA B* **21**, 622 (2004).

[62] Q. Wu, M. Litz and X.-C. Zhang. Broadband detection capability of ZnTe electro-optic field sensors. *Appl. Phys. Lett.* **68**, 2924 (1996).

[63] P. C. M. Planken, H.-K. Nienhuys, H. J. Bakker and T. Wenckebach. Measurement and calculation of the orientation dependence of terahertz pulse detection in ZnTe. *J. Opt. Soc. Am. B* **18**, 313 (2001).

[64] G. Gallot, J. Zhang, R. W. McGowan, T.-I. Jeon and D. Grischkowsky. Measurements of the THz absorption and dispersion of ZnTe and their relevance to the electro-optic detection of THz radiation. *Appl. Phys. Lett.* **74**, 3450 (1999).

[65] Q. Wu and X.-C. Zhang. 7 Terahertz braodband GaP electro–optic sensor. *Appl. Phys. Lett.* **70**, 1784 (1997).

[66] E. Hecht. *Optics*. Addison-Wesley (1998).

[67] L. Novotny and S. J. Stranick. Near-Field Optical Microscopy and Spectroscopy with Pointed Probes. *Annu. Rev. Phys. Chem.* **57**, 303 (2006).

[68] W. L. Chan, J. Deibel and D. M. Mittleman. Imaging with terahertz radiation. *Rep. Prog. Phys.* **70**, 1325 (2007).

[69] J. F. Federici, B. Schulkin, F. Huang, D. Gray, R. Barat, F. Oliveira and D. Zimar. THz imaging and sensing for security applications-explosives, weapons and drugs. *Semicond. Sci. Technol.* **20**, S266 (2005).

[70] F. Buersgens, G. Acuna and R. Kersting. Millimeter wave probing of the acoustic phase for concealed object detection. *Optics Express* **15**, 8838 (2007).

[71] F. Buersgens, G. Acuna and R. Kersting. Acoustic phase imaging with terahertz radiation. *Optics Express* **15**, 4427 (2007).

[72] E. H. Synge. Asuggested methode for extending microscopic resolution into the ultra-microscopic region. *Philos. Mag.* **6**, 356 (1928).

[73] S. Hunsche, M. Koch, I. Brener and M. C. Nuss. THz near-field imaging. *Opt. Comm.* **150**, 22 (1998).

[74] H. A. Bethe. Theory of diffraction by small holes. *Phys. Rev.* **66**, 163 (1944).

[75] F. Zenhausern, T. Martin and H. K. Wickramasinghe. Scanning interferometric apertureless microscopy: Optical Imaging at 10 Angstrom resolution. *Science* **269**, 1083 (1995).

[76] N. C. J. van der Valk and P. C. M. Planken. Electro-optic detection of subwavelength terahertz spot sizes in the near field of a metal tip. *Appl. Phys. Lett.* **81**, 1558 (2002).

[77] H.-T. Chen, R. Kersting and G. C. Cho. Terahertz imaging with nanometer resolution. *Appl. Phys. Lett* **83**, 3009 (2003).

[78] K. Wang, D. M. Mittleman, N. C. J. van der Valk and P. C. M. Planken. Antenna effects in terahertz apertureless near-field optical microscopy. *Appl. Phys. Lett.* **85**, 2715 (2004).

[79] A. J. Huber, F. Keilmann, J. Wittborn, J. Aizpurua and R. Hillenbrand. Terahertz Near-Field Nanoscopy of Mobile Carriers in Single Semiconductor Nanodevices. *Nano Lett.* **8**, 3766 (2008).

[80] A. Thoma and T. Dekorsy. Influence of tip-sample interaction in a time-domain terahertz scattering near field scanning microscope. *Appl. Phys. Lett* **92**, 251103 (2008).

[81] R. Kersting, H.-T. Chen, N. Karpowicz and G. C. Cho. Terahertz microscopy with submicrometre resolution. *J. Opt. A* **7**, 184 (2005).

[82] L. Novotny, R. X. Brian and X. S. Xie. Theory of nanometric optical tweezers. *Phys. Rev. Lett.* **79**, 645 (1997).

[83] T. Taubner, R. Hillenbrand and F. Keilmann. Performance of visible and mid-infrared scattering-type near-field optical microscopes. *J. Microsc.* **210**, 311 (2003).

[84] R. Hillenbrandt and F. Keilmann. Complex optical constants on a subwavelength scale. *Phys. Rev. Lett.* **85**, 3029 (2000).

[85] B. Knoll and F. Keilmann. Enhanced dielectric contrast in scattering-type scanning near-field optical microscopy. *Opt. Comm.* **182**, 321 (2000).

[86] B. Knoll and F. Keilmann. Infrared conductivity mapping for nanoelectronics. *Appl. Phys. Lett.* **77**, 3980 (2000).

[87] G. Acuna, S. F. Heucke, F. Kuchler, H.-T. Chen, A. J. Taylor and R. Kersting. Surface plasmons in terahertz metamaterials. *Optics Express* **16**, 18745 (2008).

[88] F. Kuchler. Terahertz Nahfeld-Mikroskopie an Metamaterialen. *Diploma Thesis, Sektion Physik, Ludwig-Maximilians Universität München* (2008).

[89] G. C. Cho, H.-T. Chen, S. Kraatz, N. Karpowicz and R. Kersting. Apertureless terahertz near-field microscopy. *Sem. Sci. Techn.* **20**, 286 (2005).

[90] H.-T. Chen, S. Kraatz, G. C. Cho and R. Kersting. Identification of a resonat imaging process in apertureless near-field microscopy. *Phys. Rev. Lett.* **93**, 267401 (2004).

[91] T. A. Milligan. *Modern Antenna Design, Second Edition*. John Wiley & Sons New Jersey (2005).

[92] M. Walther, G. S. Chambers, Z. Liu, M. R. Freeman and F. A. Hegmann. Emission and detection of terahertz pulses from metal tip antenna. *J. Opt. Soc. Am. B* **22**, 2357 (2005).

[93] F. Buersgens, R. Kersting and H.-T. Chen. Terahertz microscopy of charge carriers in semiconductors. *Appl. Phys. Lett.* **88**, 112115 (2006).

[94] S. Funk, G. Acuna, M. Handloser and R. Kersting. Probing the momentum relaxation time of charge carriers in ultrathin layers with terahertz radiation. *Opt. Express* **17**, 17450 (2009).

[95] A. Dreyhaupt, S. Winnerl, T. Dekorsy and M. Helm. High-intensity terahertz radiation from a microstructured large-area photoconductor. *Appl. Phys. Lett* **86**, 12114 (2005).

[96] G. Acuna, F. Buersgens, C. H. Lang, M. Handloser, A. Guggenmos and R. Kersting. Interdigitated terahertz emitters. *Electr. Lett.* **44**, 3 (2008).

[97] T. Bauer, J. Kolb, T. Löffler, E. Mohler, H. G. Roskos and U. Pernisz. Indium-Tin-Oxide-Coated Glass as Dichroic Mirror for Far-Infrared Electromagnetic Radiation. *J. Appl. Phys.* .

[98] M. van Exter, C. Fattinger and D. Grischkowsky. Terahertz time–domain spectroscopy of water vapor. *Opt. Lett.* **14**, 1128 (1989).

[99] P. C. M. Planken, C. E. W. M. van Rijmenam and R. N. Schouten. Opto-electronic pulsed THz systems. *Sem. Sci. Techn.* **20**, 121 (2005).

[100] G. Zhao, R. N. Schouten, N. van der Valk, W. T. Wenckebach and P. C. M. Planken. Design and performance of a THz emission and detection setup based on a semi-insulating GaAs emitter. *Rev. Sci. Instr.* **73**, 1715 (2002).

[101] G. Acuna, F. Buersgens, C. H. Lang and R. Kersting. Impact of High-Field Charge Transport on Terahertz Emission From Semiconductor Devices. *IEEE J. Sel. Top. Quant. Electr.* **14**, 1 (2008).

[102] A. Dreyhaupt, S. Winnerl, M. Helm and T. Dekorsy. Optimum excitation conditions for the generation of high-electric-field terahertz radiation from an oscillator-driven photoconductive device. *Opt. Lett* **31**, 1546 (2006).

[103] A. Dreyhaupt. Private communication in November 2006. (2006).

[104] F. Buersgens. Terahertz-Nahfeldmikroskopie an Ladungsträgern in GaAs. *PhD Thesis, Sektion Physik, Ludwig-Maximilians Universität München* (2008).

[105] F. Buersgens, G. Acuna, C. H. Lang, S. Manus and R. Kersting. Shear force control for a terahertz near field microscope. *Rev. Sci. Instr.* **78**, 113701 (2007).

[106] K. Karrai and R. D. Grober. Piezoelectric tip-sample distance control for near field optical microscopes. *Appl. Phys. Lett.* **66**, 1842 (1995).

[107] F. J. Giessibl. High-speed force sensor for force microscopy and profilometry utilizing a quartz tuning fork. *Appl. Phys. Lett* **73**, 3956 (1998).

[108] F. J. Giessibl. Advances in Atomic Force Microscopy. *Rev. Mod. Phys.* **75**, 949 (2003).

[109] K. Karrai. Lecture notes on shear force detection with quartz tuning forks. *La Londe les Maures, France* (2000).

[110] C. Colombo, D. Spirkoska, M. Frimmer, G. Abstreiter and A. F. i Morral. Ga-assisted catalyst-free growth mechanism of GaAs nanowires by molecular beam epitaxy. *Phys. Rev. B* **77**, 155326 (2008).

[111] W. Nitsche. Terahertz-Mikroskopie an Halbleitern. *Diploma Thesis, Sektion Physik, Ludwig-Maximilians Universität München* (2008).

[112] G. Strasser. Private communication in July 2009. (2009).

[113] D. Heitmann, J. Kotthaus and E. Mohr. Plasmon dispersion and intersubband resonance at high wavevectors in Si(100) inversion layers. *Solid State Commun.* **44**, 715 (1982).

[114] D. Heitmann and U. Mackens. Grating-coupler-induced intersubband resonances in electron inversion layers of silicon. *Phys. Rev. B* **33**, 8269 (1986).

[115] D. P. Kennedy, P. C. Murley and W. J. Kleinfelder. On the Measurement of Impurity Atom Distributions in Silicon by the Differential Capacitance Technique. *IBM J. Res. Develop.* **12**, 399 (1968).

[116] P. N. Brounkov, T. Benyattou and G. Guillot. Simulation of the capacitance-voltage characteristics of a single-quantum-well structure based on the self-consistent solution of the Schrödinger and Poisson equations. *J. Appl. Phys.* **80**, 864 (1996).

[117] J.N. Heyman. Private communication in July 2008. (2008).

[118] W. W. Bewley, C. L. Felix, J. J. Plombon, M. S. Sherwin, M. Sundaram, P. F. Hopkins and A. C. Gossard. Far-infrared second-harmonic generation in GaAs/AlGaAs heterostructures: Perturbative and nonperturbative response. *Phys. Rev. B* **48**, 2376 (1993).

[119] G. L. Snider, I.-H. Tan and E. L. Hu. Electron states in mesa-etched one-dimensional quantum well wires. *J. Appl. Phys.* **68**, 2849 (1990).

[120] I.-H. Tan, G. L. Snider and E. L. Hu. A self-consiten solution of the Schrödinger-Poisson equation using a nonuniform mesh. *J. Appl. Phys.* **68**, 4071 (1990).

[121] S. J. Allen Jr. , D. C. Tsui and R. A. Logan. Observation of the two–dimensional plasmon silicon inversion layers. *Phys. Rev. Lett.* **38**, 980 (1977).

[122] M. Born and E. Wolf. *Principles of Optics*. Cambridge University Press (1980).

[123] S. Bauer. Optical properties of a metal film and its application as an infrared absorber and as a beam splitter. *Am. J. Phys.* .

[124] S. W. McKnight, K. P. Stewart, H. D. Drew and K. Moorjani. Wavelength-independent anti-interference coating for the far-infrared. *Infrared Phys.* **27**, 327 (1987).

[125] M. Dressel and G. Grüner. *Electrodynamics of Solids: Optical Properties of Electrons in Matter*. Cambridge University Press (2002).

[126] M. Dressel and M. Scheffler. Verifying the Drude response. *Ann. Phys.* **15**, 535 (2006).

[127] J. Hetzler, B. Brunner, M. Wegener, S. Leu, S. Nau and W. Stolz. 100 fs Carrier Dynamics in GaAs under 100 nm Diameter Apertures. *phys. stat. sol. b)* **221**, 425 (2000).

[128] J. B. Williams, M. S. Sherwin, K. D. Maranowski, C. Kadow and A. C. Gossard. Linewidth and dephasing of Thz-frequency collective intersubband transitions in a GaAs/AlGaAs quantum well. *Physica E* **7**, 204 (2000).

[129] P. Parkinson, J. Lloyd-Hughes, Q. Gao, H. H. Tan, C. Jagadish, M. B. Johnston and L. M. Herz. Transient Terahertz Conductivity of GaAs Nanowires. *Nano Lett.* **7**, 2162 (2007).

Acknowledgements

During this dissertation I have received the support of several people to whom I would like to personally thank.

First of all I would like to specially thank Prof. Dr. Roland Kersting for the opportunity he gave me of working in his group. Without his enthusiasm and support this work would not have been possible. I also want to mention that his door was always open for me and that he was always willing to go down to the lab to discuss physics and new results.

I want to express my gratefulness to Prof. Dr. Achim Hartschuh for reading my thesis and for being the second corrector.

I would also like to thank Prof. Dr. Jochen Feldmann for allowing me to use his laboratories, infrastructure and in particular the cleanroom facilities.

Special thanks to Prof. Dr. Gottfried Strasser for growing the quantum well samples and to Prof. Dr. James Heyman for fruitful discussion.

In particular I would like to mention all my colleagues in the THz group, Federico Buersgens, Stefan Funk, Florian Kuchler, Matthias Handloser, Alexander Guggenmoos, Stephan Heucke, Hartmut Nitsche, Christian Lang, Stefan Schlögl and Konstantin Eisler who were always willing to support me. Special thanks also to all the members of the Photonics and Optoelectronics group for the working atmosphere.

In addition I would also like to acknowledge the support of Stephan Manus, Werner Stadler, Stefan Niedermaier and Christian Holopirek.

Finally I would like to deeply thank my family, my girlfriend and all my friends who supported me during all these years.

Curriculum Vitae

Guillermo Pedro Acuña,

Date of birth: 08.05.1980

Place of birth: Buenos Aires, Argentina

Education

1993 - 1998	Studies at the Philips High School (sponsored by the Dutch Philips Inc.). Electromechanical Technician degree, Buenos Aires, Argentina.
1999	Introductory Course for Engineering and Natural Sciences. Universidad de Buenos Aires, Argentina.
2000 - 2005	Physics degree at the "Universidad de Buenos Aires", Argentina. Grade Point Average: 88/100. Final Thesis at Prof. Miraglia's Atomic Collision group. Title: "Calculation of factors that affect the production and trajectory of convoy electrons".
since 2006	Ph.D. Candidate at Prof. Kersting's THz group at the Ludwig Maximilians Universität München, Munich, Germany.

Scholarships and Awards

1998	Bronze Medal and Special Prize for the best experimental solution at the Iberoamerican Physics Olympiads in Merida, Venezuela.
1999	"XXX International Physics Olympiads" in Padova, Italy.
2004	Fellowship "Beca de Verano", awarded by the "Instituto Balseiro, Centro Atómico", Bariloche Argentina.
2004	Fellowship "Beca Estímulo" (2004), awarded by the "Universidad de Buenos Aires", Argentina, for the most outstanding students of the class of 2004.